Tandem effects of lipid head and tail chemistry on the wettability of montmorillonite clay

Brenda Lin Kessenich

A dissertation

submitted in partial fulfillment of the

requirements for the degree of

Doctor of Philosophy

University of Washington

2020

Reading Committee:

James J. De Yoreo, Chair

Sarah L. Keller

Anne B. McCoy

Program Authorized to Offer Degree:

Chemistry

University of Washington

Abstract

Tandem effects of lipid head and tail chemistry on the wettability of clay

Brenda Lin Kessenich

Chair of the Supervisory Committee:
Affiliate Professor James J. De Yoreo
Materials Science and Engineering

Organic matter can drastically alter soil behavior, including by changing how soil interacts with water. In particular, organic matter can reduce a soil's ability to absorb and retain water, a phenomenon called soil water repellency. Soil water repellency leads to a variety of detrimental environmental effects ranging from increased erosion to decreased crop yield. However, the molecular mechanisms that drive soil water repellency have not been determined, which hampers the development of remediation protocols. Researchers hypothesize that amphiphilic molecules (such as phospholipids) could drive seasonal changes in water repellency. To determine the chemical factors that influence amphiphile-induced water repellency, I developed a model system consisting of one mineral, the clay montmorillonite, mixed with several phospholipids selected to test specific chemical characteristics and their relationship to water repellency.

Phospholipids have a polar headgroup and two tails of carbon chains. I tested two distinct head groups, phosphoethanolamine (zwitterionic) and phosphoglycerol (negative). The head groups were selected to test the relationship of lipid-mineral binding and wettability, as they will interact differently with the negatively-charged montmorillonite clay surface. Within each category of headgroup, I investigated two types of tails: a saturated tail that is solid (gel) at room temperature, and an unsaturated tail that is liquid at room temperature, in order to determine if the lipids' physical state – solid or liquid – influences wettability. I employed a suite of techniques designed for measurements at a range of length scales. For the smallest scale I utilized molecular dynamics, and at the mesoscale I used atomic force microscopy and fluorescence microscopy. To probe the macroscopic wettability, I utilized contact angle measurements and adapted a kinetic model to extract information on how the model system absorbed water. I measured three metrics of wettability: the initial contact angle of a water droplet on the sample surface, the kinetics of the droplet spreading across and imbibing into the sample, and the viscosity of the imbibing flow. All three metrics were altered by lipids that exhibited binding to the mineral surface, were solid at room temperature, and were distributed throughout the mineral film. In addition to determining which lipid characteristics changed wettability, this study provides unprecedented detail on the assembly of phospholipids on mineral surfaces and on the distribution of phospholipids in a model substrate. These results can help illuminate why clay alleviates water repellency and inform the design of remediation strategies.

TABLE OF CONTENTS

List of Figures.......v

List of Tables.......viii

List of Equations.......ix

List of Acronyms.......x

Chapter 1. Background.......13

1.1 Soil and soil water repellency.......13

1.2 Wettability.......17

1.2.1 Standard measurements of wettability.......17

1.2.2 Water-surface interactions and non-ideal surfaces.......20

1.2.3 Quantifying flow and including non-Newtonian parameters.......22

1.3 Experimental Techniques.......27

1.3.1 Atomic force microscopy (AFM).......27

1.3.2 Fluorescence microscopy.......29

1.3.3 Sessile drop.......29

Chapter 2. Wettability Project Summary.......30

2.1 Model system.......30

2.2 Experimental details.......32

2.2.1 Sample preparation.......32

2.2.2 Molecular dynamics simulations.......33

2.2.3 Atomic force microscopy 33

2.2.4 Fluorescence microscopy 33

2.2.5 Contact angle and droplet dynamics 34

2.3 Characteristics measured 34

2.3.1 Physical variables 34

2.3.2 Wettability variables 40

2.4 Determining the cause of wettability changes 42

2.5 Summary and conclusions 45

Chapter 3. Detailed methods 47

3.1 Lipid preparation 47

3.2 Montmorillonite preparation 49

3.3 Small-scale AFM sample preparation 49

3.4 Large-scale AFM sample preparation, fluorescence, and wettability samples 50

3.5 Note on heated/melted DSPE 51

3.6 Wettability measurements and analysis 51

3.7 Notes on Asylum Cypher AFM imaging 52

3.8 Notes on large-scale AFM imaging (Bruker ICON) 54

3.9 Image analysis: Skeletonizing fluorescence and AFM lipid/clay data 54

Chapter 4. Connecting wettability, topography, and chemistry in a simple lipid-montmorillonite system 61

4.1 Manuscript 62

4.2 Supplementary information 73

Chapter 5. Negatively-charged lipids exhibit negligible effects on the water repellency of montmorillonite films 86

5.1 Manuscript 87

5.2 Supplementary information 108

Chapter 6. Structures of dried fatty acids 118

6.1 Introduction 118

6.2 Methodology 119

6.2.1 Experimental details 119

6.2.2 Molecular packing theory calculations 119

6.3 Results 122

6.3.1 Structures of fatty acids and a phospholipid 122

6.3.2 Decanoic acid mixed with other molecules 124

6.3.3 Non-lipid structures 126

6.3.4 Molecular packing theory results 126

6.4 Discussion and conclusions 128

6.5 Additional images 129

Chapter 7. PC Lipids, solvent effects, and high lipid coverage 132

7.1 PC lipids 132

7.1.1 PC aggregates on the montmorillonite film surface 132

7.1.2 DOPC on a flat mica surface 134

7.1.3 PC fluorescence 135

7.2 Comparing lipids dried from H_2O and dried from $CHCl_3$ 136

7.3 High-coverage lipid/clay films 138

Appendix A: Code for data collection and analysis 140

Bibliography 150

LIST OF FIGURES

Figure 1-1: Hypothesized vs. observed organic matter configurations.. 15
Figure 1-2: The contact angle of a water droplet on a surface. 18
Figure 1-3: Relationships between different methods of measuring wettability............. 20
Figure 1-4: Different wetting scenarios.. 22
Figure 1-5: Newtonian vs. non-Newtonian fluids. 25
Figure 1-6: Interfacial interactions alter fluid flow. 26
Figure 1-7: AFM schematic. 27
Figure 1-8: Phase images. 29
Figure 1-9: Instrument set-up for sessile drop data.. 30
Figure 2-1: Lipid aggregate behavior in solution. 35
Figure 2-2: The main morphologies of lipids on the film surface. 36
Figure 2-3: Example of image processing.. 38
Figure 2-4: Fluorescence indicating lipid distribution. 40
Figure 2-5: Measured wettability characteristics for lipid-clay systems. 42
Figure 2-6: How linear fits were generated for wettability and physical variables......... 43
Figure 3-1: Teflon tape and Parafilm to prevent evaporation of chloroform. 47
Figure 3-2: Cleaving mica.. 49
Figure 3-3: Example of a sessile drop on a surface. 52
Figure 3-4: Adjusting the binary threshold in ImageJ. 55
Figure 3-5: The result of applying a binary threshold in ImageJ. 56
Figure 3-6: How to skeletonize an image in ImageJ. 57
Figure 3-7: The result of skeletonizing an image. 58
Figure 3-8: Setup of the Analyze Skeleton macro. 59
Figure 3-9: Where to find the Analyze Skeleton macro. 59
Figure 3-10: The results of processing one image. 60
Figure 4-1: (S1) An example of image processing with annotation. 75
Figure 4-2: (S2) A complete example of image processing with histograms. 77
Figure 4-3: (S3) The geometry of a spherical cap. 78

Figure 4-4: (S4) Correlations of physical and wettability variables for DSPE. 84
Figure 4-5: (S5) Correlations of wettability and physical characteristics for DOPE. 85
Figure 5-1: An example of image processing. 94
Figure 5-2: Lipid aggregates on montmorillonite.. 96
Figure 5-3: Results from MD simulations. 98
Figure 5-4: Film topography and lipid distribution.. 99
Figure 5-5: Comparison of PE and PG lipid wetting characteristics. 102
Figure 5-6: Correlations between a physical variable.. 103
Figure 5-7: (S1) All contact angle data points.. 109
Figure 5-8: (S2) Aggregate characteristics... 110
Figure 5-9: (S3) Additional height profiles. 110
Figure 5-10: (S4) Wettability variables vs. concentration for PG lipids. 111
Figure 5-11: (S5) PG wettability variables against each other. 112
Figure 5-12: (S6) Cartoon of lipid aggregates.. 113
Figure 5-13: (S7) Representative fluorescence micrographs. 114
Figure 5-14: (S8) DSPG correlation plots for which $r^2 > 0.8$.................................... 116
Figure 5-15: (S9) : All DOPG correlation plots for which $r^2 > 0.7$. 117
Figure 6-1: Dried structures of fatty acids. 122
Figure 6-2: Vertical profile of a "ribbon”. 123
Figure 6-3: Dried structures. 125
Figure 6-4: Vertical profile of a "flat" surface. 125
Figure 6-5: Dried structures of serine and alanine ethyl ester..................................... 126
Figure 6-6: Molecular packing theory results. 127
Figure 6-7: Additional dried decanoic acid vesicle images. 129
Figure 6-8: Decanoic acid vesicles and alanine... 129
Figure 6-9: Decanoic acid and alanine ethyl ester... 130
Figure 6-10: Decanoic acid and HEPES. 131
Figure 6-11: Benzoic acid. 131
Figure 7-1: PC lipids on montmorillonite. 133
Figure 7-2: Unbiased molecular dynamics simulation of DOPC. 134

Figure 7-3: DOPC on mica. 135
Figure 7-4: Fluorescence micrographs. 136
Figure 7-5: Lipids dried from chloroform vs. water. 137
Figure 7-6: Lipids at 300% coverage on montmorillonite. 138
Figure 7-7: Topography (left column) vs. phase images (right column). 139

LIST OF TABLES

Table 1-1: Summary of common methods to measure surface wettability...................... 18

Table 1-2: Summary of prior SWR studies.. 22

Table 2-1: Lipid properties.. 31

Table 2-2: Lipid-montmorillonite binding and physical state at room temperature......... 32

Table 2-3: Categorization of experimental variables.. 34

Table 2-4: Lipid aggregate characteristics. 37

Table 2-5: Summary of lipid characteristics in a lipid-montmorillonite system............. 43

Table 2-6: Correlations of wettability variables with physical variables......................... 45

Table 4-1: (S1) Values of the exponent a, time constant, and rate constant K. 80

Table 4-2: (S2) Average diameters.. 81

Table 4-3: (S3) Comparison of fluorescence and AFM data for DOPE.......................... 81

Table 4-4: (S4) Comparison of fluorescence and AFM data for DSPE 82

Table 4-5: (S5) r^2 values from linear regressions 82

Table 5-1: Fraction of aggregates on clay flake edges. 97

Table 5-2: Wettability percent difference. 101

Table 5-3: An overview of correlation strength. 105

Table 5-4: (S1) All wettability data for PG samples. 108

Table 5-5: (S2) r^2 values for each linear comparison. 115

Table 6-1: Summary of molecular packing theory results. 128

LIST OF EQUATIONS

1.1: Young's Equation…... 17

1.2: Wenzel Equation………... 21

1.3: Cassie-Baxter………………………... 21

1.4: Droplet spreading……………………………... 23

1.5: Droplet spreading.. 23

1.6: *a,* spreading-limited 24

1.7: *a,* imbibition-limited 24

1.8: Power law viscosity 24

1.9: AFM spring force…………... 28

2.1: Lipid coverage. 33

4.1 Droplet height……... 77

4.2: Droplet volume………………………….. 78

4.3 Droplet radius (1.5) 79

6.1: Packing parameter.. 120

6.2: Fatty acid tail length... 120

LIST OF ACRONYMS

AFM: Atomic force microscopy
CA: Contact angle
CAM: Coverage as monolayer
DA: Decanoic acid
DOPC: 1,2-dioleoyl-sn-glycero-3-phosphocholine
DOPE: 1,2-dioleoyl-sn-glycero-3-phosphoethanolamine
DOPG: 1,2-dioleoyl-sn-glycero-3-phospho-(1’-rac-glycerol)
DSPC: 1,2-distearoyl-sn-glycero-3-phosphocholine
DSPE: 1,2-distearoyl-sn-glycero-3-phosphoethanolamine
DSPG: 1,2-distearoyl-sn-glycero-3-phospho-(1’-rac-glycerol)
Fl: Fluorescence microscopy
MD: Molecular dynamics
MED: Molarity of ethanol droplet (test)
MMT: Montmorillonite
PC: Phosphocholine lipid headgroup
PE: Phosphoethanolamine lipid headgroup
PG: Phosphoglycerol lipid headgroup
SA: Stearic acid
SWR: Soil water repellency
TC: Time constant, inverse of rate constant *K*
WDPT: Water droplet penetration time (test)

ACKNOWLEDGEMENTS

I could not have completed this degree alone. I am immensely grateful for the guidance I have received from my advisors Jim De Yoreo and Sarah Keller and their respective groups. In particular, I thank Caitlin Cornell, Zack Cohen, Chantelle Leveille, Heidi Spears, Dr. Glennis Rayermann, Dr. Scott Rayermann, Catherine Chang, and Ana Duarte for being wonderful co-workers (go Squishy Squad!). Thank you to Dr. Elias Nakouzi, Dr. Ben Legg, and Dr. Christina Newcomb for their mentorship and many fruitful scientific discussions. Thank you to all my co-authors for their expert feedback and advice on my long manuscripts and support through the publishing process. Thank you to Dr. Micah Glaz and Dr. Raj Giridharagopal for fielding my many AFM questions. I am also grateful for the Department's administrative and custodial staff, who provided a great place to work.

Thank you to my friends and family, in particular Michael DeGregori, Scott Rayermann, Alex Sturbaum, Rae Eaton, Jared Canright, Ashley Dostie, Nick Montoni, and Kaitlyn Casimo for getting me outside the lab, making sure I ate something that wasn't cookies for lunch, and for all your support through the rough patches. Thank you to Nick Montoni and Addie Kingsland for paving the way for another queer chemist. Thank you to a very special group of my pets and friends' pets (Lapis, Pearl, Leona, Zarya, Coconut, Hoa, Chell, Roswell, Bilbo, and Dahli) for being wonderful fuzzy companions, even if you did get fur all over my car and sometimes tried to eat my shoes. Thank you to the National Forest Service, the Washington State Parks, and the Washington Trails Association for stewardship of the wild places I escaped to on the weekends. Thank you to the McElroy family of podcasts, without which all the long hours I spent imaging would have been much less anticipated and enjoyed.

DEDICATION

For everyone who has struggled with imposter syndrome: you are not alone.

Chapter 1. BACKGROUND

In this chapter, I introduce the background information for my work on soil wettability. In the next chapter, I summarize the wettability project's model system, approach, and results. Chapter 3 contains detailed protocols for carrying out experiments. Chapters 4 and 5 represent my publications in this field. Chapter 6 represents my work on a different branch of research on the role of decanoic acid in the origin of life. Chapter 7 contains additional, incomplete data for the wettability project. Appendix A contains code I wrote and/or used to process and analyze my data.

1.1 SOIL AND SOIL WATER REPELLENCY

The organic components of soil dramatically alter its behavior. Erosion rates, for example, largely depend on the quantity of roots and other organic "cements" that hold slopes in place. Organic matter also governs how a soil interacts with water. Most mineral surfaces are hydrophilic[1], but a coating of organic matter can induce hydrophobicity. Soil water repellency (SWR) occurs when a soil does not readily absorb and retain water. When occurring on a large enough scale, SWR reduces crop output, increases erosion rates, and changes runoff patterns. Organic matter is generally known as the source of SWR, but the exact mechanisms by which organic matter alters the soil's hydrophilicity have not been identified, which restricts development of remediation protocols. This remains relevant because extreme events, such as wildfires, associated with climate change will worsen SWR[2,3,4].

Broadly speaking, soil is composed of two types of materials: inorganic material (rocks, minerals) and organic material (plants, microbes). Because the source of both the inorganic and organic components varies by location, soil has a tremendous geographical diversity[5]. At a much smaller scale, the distribution of organic matter is still heterogenous[6]. Soil harbors a large quantity of organic matter that exists on a continuum ranging from intact plant matter, to decaying organisms, to highly oxidized organic molecules[7]. The study of natural soil organic matter is complicated by the self-aggregation of molecules and the complexity of organic-mineral interactions. For example, an amphiphilic molecule will tend to aggregate with other amphiphiles in an aqueous environment, but may also bind to available mineral surfaces. Even for model systems with single-crystal interfaces and therefore few defect or edge sites to change how organic matter binds to surfaces, the nature of organic-mineral interactions are complex[8].

Organic matter ranging in complexity from a colony of bacteria[9] to a simple coating of a fatty acid[10] has been observed to increase the hydrophobicity of mineral surfaces. The assembly of organic matter on mineral grains could influence SWR, and it has been proposed that amphiphilic molecules – molecules with one hydrophilic end and one hydrophobic end – could contribute to seasonal SWR cycling by changing their conformation **(Figure 1-1)**. Should the molecules' hydrophilic end be exposed, the soil ought to be more hydrophilic, and vice versa[11]. However, this hypothesized behavior has not been directly observed. In fact, imaging thus far has shown that amphiphilic organic matter tends to assemble into globules[12] rather than films (**Figure 1-1D**).

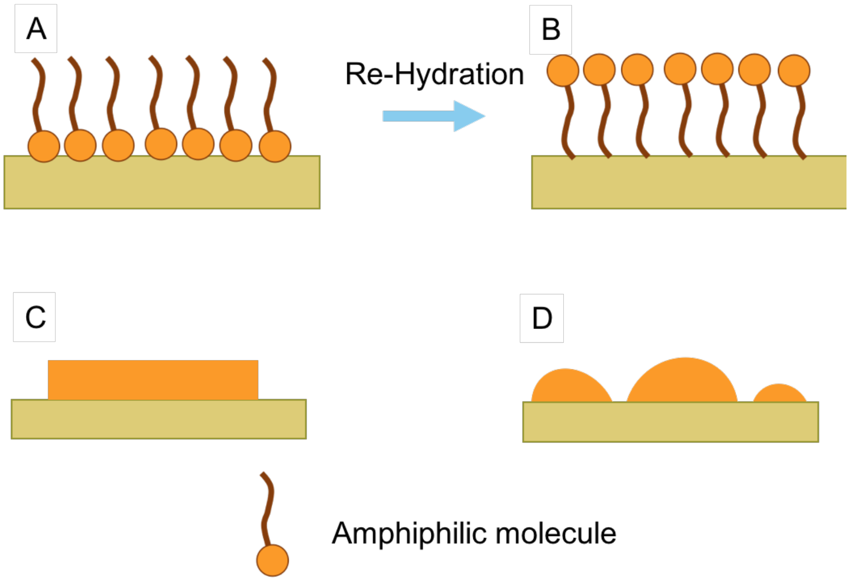

Figure 1-1: Hypothesized vs. observed organic matter configurations. It has been hypothesized that a monolayer of amphiphiles with exposed hydrophobic tails (A) could cause SWR, and on re-wetting could change conformation to expose hydrophilic heads (B) causing the soil to become wettable again. However, if this monolayer scenario occurred, we expect to observe sample topography (C) that is flat and uniform, whereas what is actually observed (D) is lumpy aggregates[12].

Some studies have taken soils into the lab, and shown that certain types of organic matter can induce water repellency in sampled soils or model substrates. Ma'shum *et al.*[13] used gas chromatography-mass spectrometry to demonstrate the presence of fatty acids with 16-32 carbon tails in water-repellent soils, with the maximum SWR occurring at the concentration of molecules required to coat the mineral in many monolayers. De Blas *et al.*[14] found that removing the lipid fraction of soil organic matter from natural soil drastically reduced SWR. Mainwaring *et al.*[15] demonstrated that a variety of organic molecules induce SWR on clean sand, and that the SWR was highest for combinations of molecules; for example, alkanes and fatty acids together caused more SWR than either component alone. Likewise, Leelamanie *et al.*[10] showed that the amphiphilic molecule stearic acid induced water repellency on a model sand substrate.

A few studies have begun to link the arrangement of organic matter on soil surfaces to the macroscale soil wettability. These studies sometimes include imaging, but the imaging is often on a single-crystal, flat surface, while the wettability is measured on a multi-crystal, particulate surface that has different roughness, porosity, and permeability than the single-crystal surface. For example, Truong *et al.*[12] measured wettability on a substrate of crushed quartz and imaged organic aggregates on a flat, single-crystalline quartz surface. On the other hand, measuring wettability of organic matter on a glass slide may be more comparable to the images collected on the same surface (as done by Kaltenbach *et al.*[16]), but may not behave the same as a multi-crystalline soil sample with more defect sites and roughness to which organic matter could adhere. Cheng *et al.*[17] and others have imaged natural organic matter on mineral substrates; however, because the organic matter or the substrate used has not been molecularly characterized, the type of organic aggregation occurring remains unknown.

An additional consideration is that Cheng *et al.*[18] and Leelamanie *et al.*[10] use double-sided tape to hold their particulate matter in place for measuring the wettability, opening up the possibility of contamination from the tape adhesive. Furthermore, the organic molecules are typically introduced into the substrate via an organic solvent[10,15]. While this choice is no doubt made because of the solubility of the molecule of interest, the solvent could leave behind the organics in a very different configuration than would occur if they were introduced in an aqueous, more soil-analogous solution. If the configuration of the molecules is indeed responsible for SWR, organic solvents should be used cautiously.

In short, what is needed is a study that images a known organic material, with known concentration, on a known, particulate surface, and measures the wettability on the same particulate substrate – without introducing additional confounding variables like tape adhesive and variable solvents. These characteristics are summarized in **Table 2** at the end of section **1.2**.

1.2 WETTABILITY

Wettability, like soil, is complex. Both chemistry and texture can change a material's wettability. Certain waxes may be hydrophobic, but texturing the surface can increase hydrophobicity still further[19]. Therefore, when thinking about wettability of soils, both the chemistry of the organic matter and the particulate, textured nature of the soil must be considered.

1.2.1 *Standard measurements of wettability*

Several methods have been widely used to measure the wettability of a given soil sample: contact angle (CA), the molarity of ethanol droplet test (MED), and the water droplet penetration time test (WDPT). All of these methods probe the surface energy of a sample surface relative to the surface tension of a liquid droplet and are summarized in **Table 1-1**.

CA is one method for determining wettability, and has a relatively simple concept: water will form beads on a more hydrophobic surface, and therefore have a large contact angle, while it will spread out on a hydrophilic surface and have a lower contact angle **(Figure 1-2)**. Contact angle and surface tension are related by Young's Equation[20]:

$$\gamma_{sv} - \gamma_{sl} = \gamma_{lv} cos\theta \qquad \text{1.1: Young's Equation.}$$

where γ_{sl} is the surface tension of the solid-vapor interface, γ_{sl} is the surface tension of the solid-liquid interface, γ_{lv} is the surface tension of the liquid-vapor interface (72 mN/m for water in air), and θ is the contact angle of the liquid with respect to the solid-vapor contact line. The solid-vapor surface tension must be larger than the solid-liquid surface tension in order to have a favorable liquid-solid interaction. Therefore, solids with a relatively low surface tension will have large contact angles and be considered hydrophobic, as it is more favorable to maximize the surface area of the solid in that case. CA = 90° represents the case where the solid-vapor and solid-liquid surface tensions are equal. **Equation 1.1** assumes a flat, chemically homogenous surface.

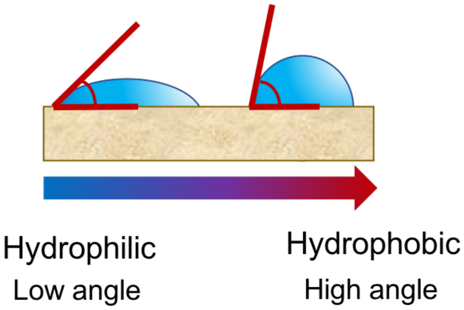

Figure 1-2: The contact angle of a water droplet on a surface will be higher if the surface is more hydrophobic.

Table 1-1: Summary of common methods to measure surface wettability.

Method	**Measurement**	**Classification**	**Comments**
Contact Angle (CA)	Angle > 90°	Hydrophobic	-Typically assumes "equilibrium" CA at time = 0
	Angle < 90°	Hydrophilic	
Water Droplet Penetration Time (WDPT)	Time < 5s	Wettable	-Values from Dekker and Ritsema 1994[23] -King 1981 uses this only up to 4 min (240s)[22]
	5s - 60s	Slightly water repellent	
	60s - 600s	Strongly water repellent	
	600s - 3600s	Severely water repellent	
	Time > 3600s	Extremely water repellent	
Molarity of Ethanol (MED)	Ethanol concentration < 1 M	Slight water repellency	-Scale from King 1981[22] -Time of <10s (Roy and McGill)[24] or <5s (Dekker and Ritsema[23] and Letey *et al.*[21]) to complete penetration, defined as CA = 0°, for spontaneous wetting
	1.0 – 2.2 M	Moderate water repellency	
	> 2.2 M	Severe water repellency	

The MED test instead changes the surface tension of the water droplet by adding different fractions of ethanol[22]. Ethanol reduces the surface tension of the water droplet. If enough ethanol is added, it becomes favorable for the droplet to spread out/imbibe into a hydrophobic substrate. A series of droplets, ranging from no ethanol to > 2.2 M ethanol, is set on a surface of interest. The concentration of ethanol at which the droplet readily soaks into the sample is deemed a proxy for the sample's surface energy. Complete absorption of the droplet into the sample is defined as a contact angle of 0°. Because they both relate to surface energy, MED results can be compared to CA results. However, the penetration time cutoff is defined differently by different authors; for example, Dekker and Ritsema[23] use 5s as the cutoff while Roy and McGill[24] use 10s.

The WDPT test is similar to the MED test, but uses only water. A water droplet is set on the surface and the time it takes for the droplet to soak in is measured. The longer the time, the more persistent the hydrophobicity of the sample. Rather than a measurement of the surface energy, the WDPT test determines the time required for the surface to interact with the water droplet until its own surface tension is altered to increase past the solid-liquid surface tension, allowing water penetration. Again, the time the droplet is monitored depends on the author; Dekker and Ritsema[23] monitor for up to an hour while King[22] only monitored for four minutes.

The WDPT, MED, and CA tests can be used in tandem, and the relationships between them have been empirically determined before[22,23,24] **(Figure 1-3)**. The range of wettability explored by each technique varies.

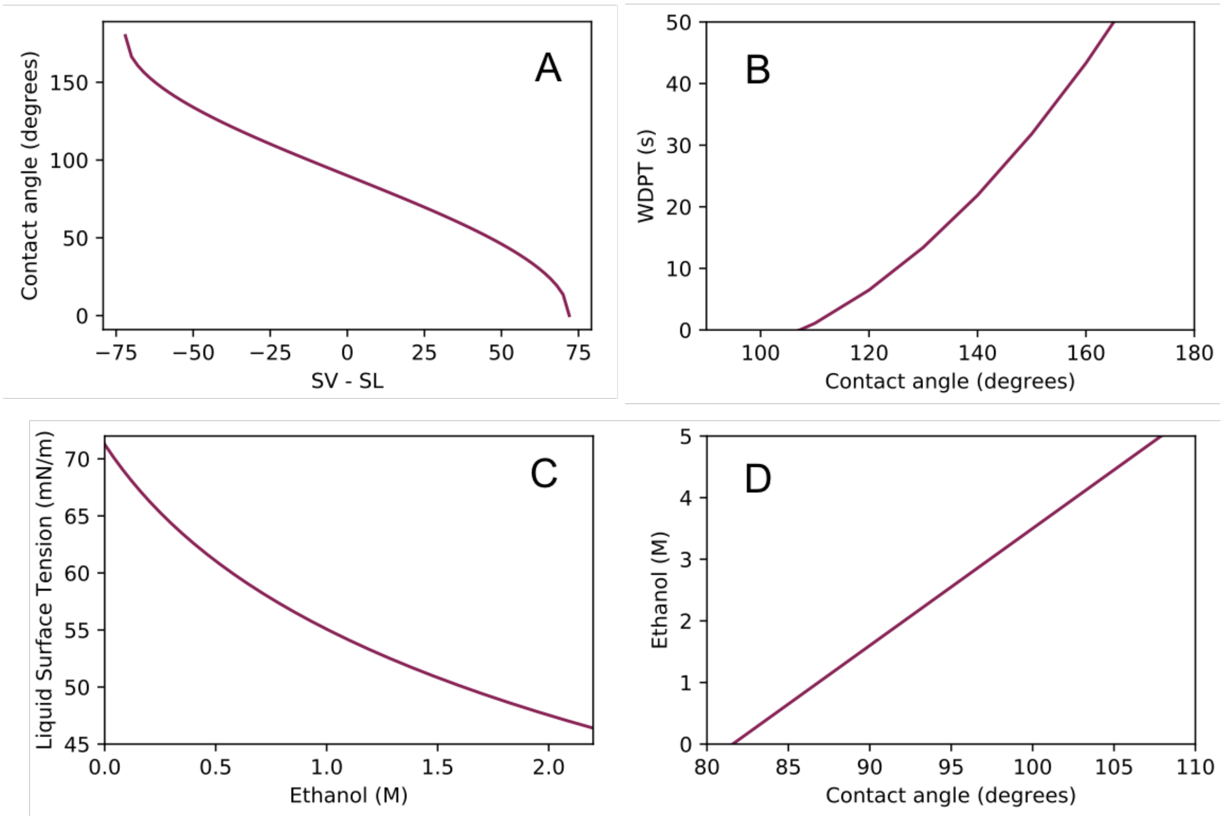

Figure 1-3: Relationships between different methods of measuring wettability. A) Young's equation for water on an ideal surface. The X-axis is the difference in surface tensions between solid-vapor (SV) and solid-liquid (SL) interfaces, measured in mN/m. B) The empirical WDPT relationship with CA. C) The surface tension of a mixed water-ethanol drop for different concentrations of ethanol. D) The empirical MED correlation with CA measurements.

1.2.2 *Water-surface interactions and non-ideal surfaces*

Water interacts with surfaces in a multitude of ways. For an ideal, flat surface, no air pockets can form, and the hydrophobicity ought to depend only on the chemistry **(Figure 1-4A)**. In this case, the contact angle and surface energy relationship can be described by Young's equation **(Equation 1.1)**. For a rough surface, air pockets may exist under the water droplet, or perhaps the valleys in the surface will already be filled, which will change how water interacts with a substrate[25] **(Figure 1-4B,C,D)**.

The Wenzel equation applies to a situation where a water droplet placed on a rough surface interacts with the entire surface, valleys and ridges **(Figure 1-4B)**. This type of wetting serves to exaggerate the effect the surface chemistry would have; e.g. it makes hydrophobic surfaces more hydrophobic, and hydrophilic surfaces more hydrophilic. The observed contact angle θ_{obs} deviates from the contact angle of water on a flat surface of the same material θ_{chem} by the ratio of the actual surface area to the planar area *r:*

$$cos\theta_{obs} = r * cos\theta_{chem} \qquad \text{1.2: Wenzel Equation.}$$

Cassie-Baxter wetting **(Equation 3)** occurs when the valleys in the rough surface are already filled with water or air that the water droplet cannot displace **(Figure 1-4C,D)**. Surface heterogeneity can cause contact angles to be much higher than would be predicted by surface chemistry alone. In this case, the observed contact angle θ_{obs} is derived from the contact angle of water on each of the two materials making up the surface (θ_1 and θ_2), and the fraction of the surface occupied by each material (φ_1, 1-φ_1). For most discussions of the Cassie-Baxter wetting state, the two materials are air and the solid substrate.

$$cos\theta_{obs} = \varphi_1 cos\theta_1 + (1 - \varphi_1) cos\theta_2 \qquad \text{1.3: Cassie-Baxter.}$$

As a result, any study of soil wettability must not only account for chemical effects on wettability, but also determine if the surface topography contributes to the observed wettability. When considered along with the various configurations of soil wettability listed in **Table 1-2**: Summary of prior SWR studies., comparison of different studies becomes difficult, especially given the lack of direct imaging of the soil surfaces investigated.

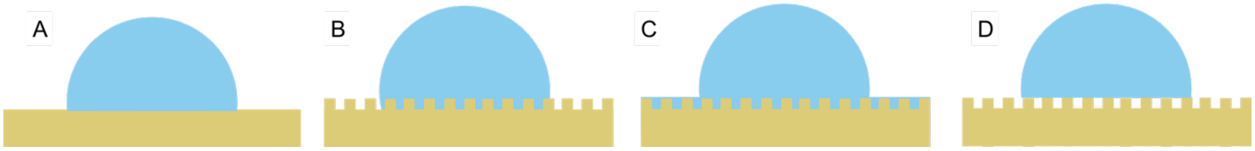

Figure 1-4: Different wetting scenarios. A) Ideal surface, B) Wenzel, C) Cassie-Baxter with a hydrated surface, D) Cassie-Baxter with air trapped by the surface roughness. Derived from McHale *et al.* 2004 with permission from John Wiley and Sons[25].

Table 1-2: Summary of prior SWR studies.

Study	Known organic?	Known substrate?	Imaging?	Imaging substrate particulate?	Wettability measured on particulate?	Contact angle?	WDPT?	MED?
Kaltenbach[16]	No	Yes	Yes	No	No	Yes	No	No
Truong[12]	Yes	Yes	Yes	No	Yes	Yes	No	No
Mainwaring[15]	Yes	Yes	No	n/a	Yes	No	Yes	No
Cheng[18]	Yes	No	Yes	Yes	Yes	Yes	Yes	No
Leelamanie[10]	Yes	Yes	No	n/a	Yes	Yes	Yes	Yes
Ma'shum[13]	Yes	Yes	No	n/a	Yes	No	No	Yes
Petridis[26]	Yes	Yes	No	n/a	No	Yes	No	No

1.2.3 *Quantifying flow and including non-Newtonian parameters*

The CA approach to wettability assumes that the initial contact angle measured is an equilibrium value, and will be distorted by the surface roughness. The MED and WDPT tests are not well standardized, as they require the experimenter to determine when a droplet has been absorbed and have been arbitrarily assigned wettable/not-wettable cutoffs. In general, these techniques work better for more hydrophobic samples.

To account for non-equilibrium droplet-sample interactions, and still obtain the information on the persistence of hydrophobicity provided by the WDPT test, I turned to fitting the radius of a droplet imbibing into a porous substrate with an equation developed by Chao *et al.*[27]:

$$R = \left(\left(\frac{\lambda}{\alpha}\right) \left(\frac{\sigma}{k}\right)^{\frac{1}{n}} \left(\frac{n}{2n+1}\right) \left(\frac{V_0^{\frac{n-2}{n}}}{2\pi^{\frac{n-2}{n}}}\right) (t - t_0) \right)^{\alpha} \qquad \text{1.4: Droplet spreading.}$$

where R is the droplet radius, *t* is the time since the droplet touched the surface, *n* is the fluid index, α is a fluid index proxy, V_0 is the droplet volume, σ is the surface tension, *k* is the fluid's flow consistency index, and λ is the effective lubrication parameter of the substrate. In a system comprised of water, a mineral, and soluble organic matter, the exact composition of the fluid present is not known; some organic will solubilize and the fluid should not be assumed to be pure water. Further, the clay properties will change as the clay swells during imbibition. Because *k* and λ will not be known for this system, we combined all factors before $(t-t_0)$ into a variable *K*. We also assumed $t_0 = 0$. This simplified the equation to:

$$\frac{R}{R_0} = [1 + Kt]^{a} \qquad \text{1.5: Droplet spreading.}$$

where R is the droplet radius, R_0 is the drop radius at $t = 0$, *K* is a constant, and *a* is the same fluid index proxy as α in the original equation **(Equation 1.4)**. *K* is inversely proportional to the time constant *TC* of the radius spread, and therefore give an indication of the speed at which the droplet spreads across the surface.

Depending on whether spreading across the surface[27] or imbibition into the substrate[28] is the limiting factor, a is respectively

$$a = \frac{n}{3n+7} \qquad \text{1.6: } a\text{, spreading-limited}$$

or

$$a = \frac{1}{n+1} \qquad \text{1.7: } a\text{, imbibition-limited}$$

The fluid index *n* indicates how the fluid viscosity changes when subjected to strain. Newtonian fluids do not change their viscosity when subjected to stress, and will always have $n = 1$. Shear-thinning (pseudo-plastic) fluids are defined as having $n < 1$, and are less viscous under strain, whereas shear-thickening (dilatant) fluids ($n > 1$) become more viscous under strain[29]. Modern paint typically behaves as a shear-thinning fluid; while being rolled onto a surface, the paint experiences shear strain from the roller, and is thin enough to spread out. After the roller and therefore the strain is removed, the paint thickens and does not drip. A shear-thickening fluid such as Oobleck (corn starch and water) will thicken when stressed by being hit by a dropped object. However, if an object is instead slowly lowered into an Oobleck mixture, the fluid is thin and the object can be immersed in the Oobleck.

Fluid index n and viscosity η are related through the shear rate $\dot{\gamma}$, and material constant K, by the Ostwald-de Waele or power law model[29]:

$$\eta = K\dot{\gamma}^{n-1} \qquad \text{1.8: Power law viscosity}$$

This relationship is plotted in **Fig. 1-5** for $n = 1$, $n < 1$, and $n > 1$.

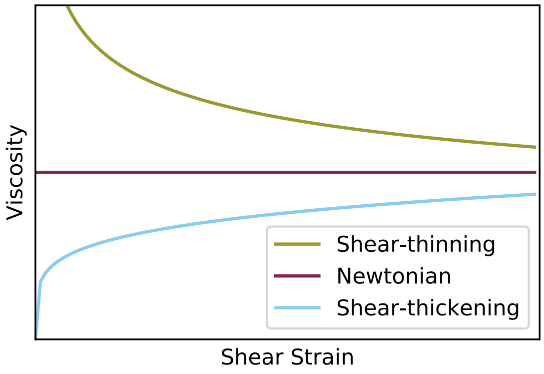

Figure 1-5: The relationship between fluid viscosity behavior and shear strain for Newtonian and non-Newtonian fluids.

Water typically behaves as a Newtonian fluid with $n = 1$. However, because non-Newtonian behavior has been proposed to occur in clay soils, using methodology that can account for non-Newtonian flow is essential.

Specifically, non-Newtonian behavior could contribute to non-Darcian flow in clay[30]. In Darcian flow, the potential energy (measured as hydraulic head) of a fluid and its flow rate have a linear relationship. Nonlinear and therefore non-Darcian relationships have been found for water flow through clay, especially in unsaturated conditions where water does not completely fill the available pore space and the rest of the pore volume is occupied by air[31]. Shear-thinning (the liquid becomes less viscous) behavior is proposed to account for this; H.H. Liu *et al.* find flow with $n = 0.28$ in an unsaturated clay column.

This change is most likely a result of strong interfacial interaction between the clay surface and water molecules[30,32,33]: water bonds to the charged clay surface, which alters its flow by reducing the water-water interactions relative to clay-water interactions **(Figure 1-6)**. Additionally, as the water infiltrates soil pores containing organic matter, the local concentration of surfactant molecules may be quite high; such solutions also exhibit non-Newtonian behavior[34].

Overall, **Equation 1.5** represents a more effective way to gauge wettability of a porous surface than the CA, MED, or WDPT methods alone, as it accounts for the temporal persistence of hydrophobicity as well as the speed of imbibition or spreading across the surface.

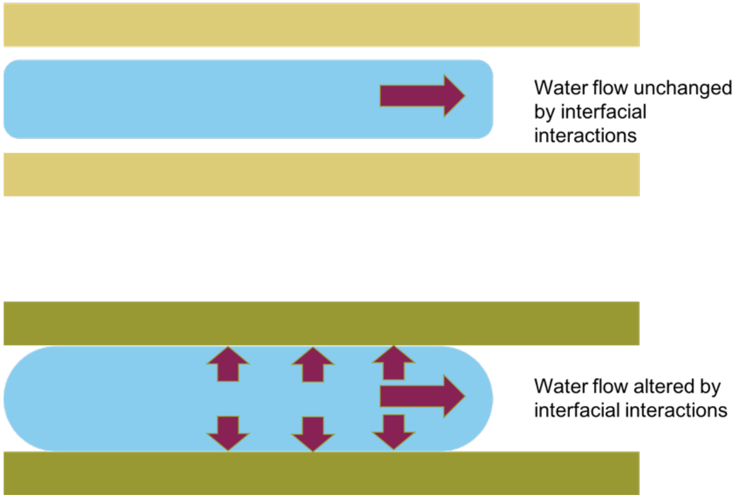

Figure 1-6: Interfacial interactions alter fluid flow. Top: if a material and water do not appreciably interact, the material is "ideal" and does not alter water flow. Bottom: if a material and water interact strongly via intermolecular forces, the water flow can change considerably.

1.3 EXPERIMENTAL TECHNIQUES

1.3.1 *Atomic force microscopy (AFM)*

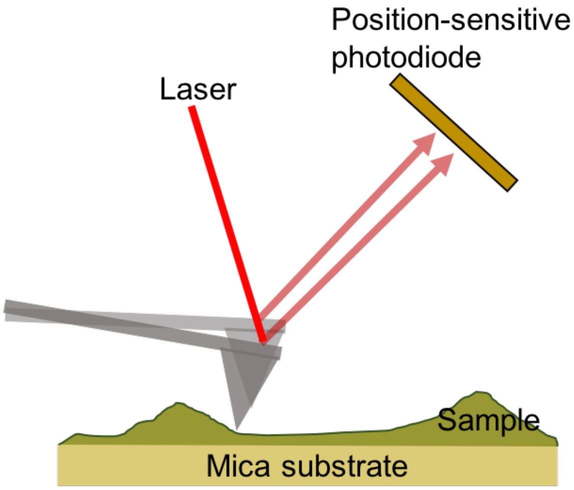

Figure 1-7: AFM schematic. A laser reflected off the back of the AFM cantilever changes position on a photodiode; the position changes with the sample topography.

Atomic force microscopy is a versatile surface technique. Here, I leverage it primarily to determine surface topography, identify organic matter aggregates and mineral grains, and determine surface roughness.

AFM was invented in 1986 by Binnig and Quate as an extension of the principles of scanning tunneling microscopy and stylus profilometry[35]. Modern AFMs are capable of detecting picometer-scale changes in topography.

AFM produces images by a raster scan where deflection indicates sample surface topography. The raster moves a probe (the ‘tip’) across along a fast axis (typically, the x-axis) and a slow axis (the y-axis). The tip is attached to a cantilever with a known spring force constant, $k_{\text{cantilever}}$. The cantilever bends as the tip interacts with the sample; this deflection dz is measured by a laser which reflects off the back of the cantilever and is detected by a photodiode

(Figure 1-7). The restoring force $F_{restore}$ can be calculated from the interaction of the sample surface with the tip[36]:

$$F_{restore} = -k_{cantilever} dz \qquad \text{1.9: AFM spring force}$$

Imaging can be performed in a *contact mode* or *tapping mode.* In contact mode, the tip-to-sample force is held at a set-point. While scanning, adjustments in sample-to-probe distance keep the force at the set-point, with the adjustments providing sample topography information. Contact mode works best with a $k_{cantilever} \approx 0.15$ N/m, as a small spring constant minimizes damage to the sample while increasing responsiveness to surface forces and providing a better signal. Friction data can also be collected if the sample causes side-to-side twisting of the cantilever[36].

Tapping mode is less likely to damage the sample than contact mode[37]. Rather than dragging the tip along the surface as in contact mode, a drive amplitude is applied so that the cantilever oscillates as it rasters along the sample. This amplitude will change as the tip interacts with the sample; the corrections necessary to keep the cantilever at the set-point amplitude provide height information. Tapping mode requires a larger spring constant, typically $k_{cantilever} \approx$ 40 N/m. In general, in tapping mode the tip is less likely to get stuck on the sample, and thus it provides higher resolution topography; in particular, the high spring constant reduces error caused by excessive bending of the cantilever[37].

Tapping mode can also be used to produce a “phase image”. Typically, there is a 90 degree difference between the oscillation of the cantilever base and the oscillation of the tip[38]. When interacting with the sample, the difference in phase between the free end of the cantilever versus the base of the cantilever (where the driving amplitude is applied) can also be measured

(Figure 1-8). The difference indicates tip-sample interactions due to changes in material characteristics on the surface[38]. For example, a particularly soft material may have good phase contrast with a harder material. However, phase images must be interpreted cautiously because changes in height often cause a difference in phase[39].

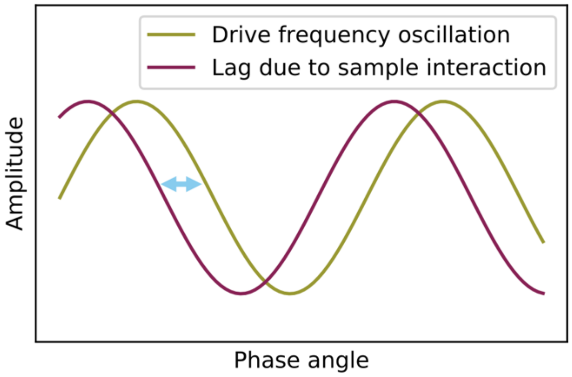

Figure 1-8: Phase images are produced by mapping the lag in frequency between the cantilever base and the tip. The amount of lag is indicated by the blue double-headed arrow.

1.3.2 *Fluorescence microscopy*

Fluorescence microscopy has been used extensively to image self-assembled structures of amphiphilic molecules, such as lipid vesicles[40]. Use of a fluorophore attached to a lipid provides a lipid-specific fluorescence that maps the location of lipids in physical space. Due to the optical resolution limit, this type of fluorescence cannot map the localization of a single lipid, but can accurately identify collections of lipids.

1.3.3 *Sessile drop*

Contact angle can be measured by depositing a sessile droplet on a surface (as opposed to a pendant drop that hangs from a needle in air). Automated droplet placement can deposit droplets of a known volume with the same force each time, which removes error caused by placing droplets with varying quantities of force, which would perturb the initial contact angle. A camera is used to capture images of the sessile drop on placement or record videos of the droplet as it interacts with the surface **(Figure 1-9)**.

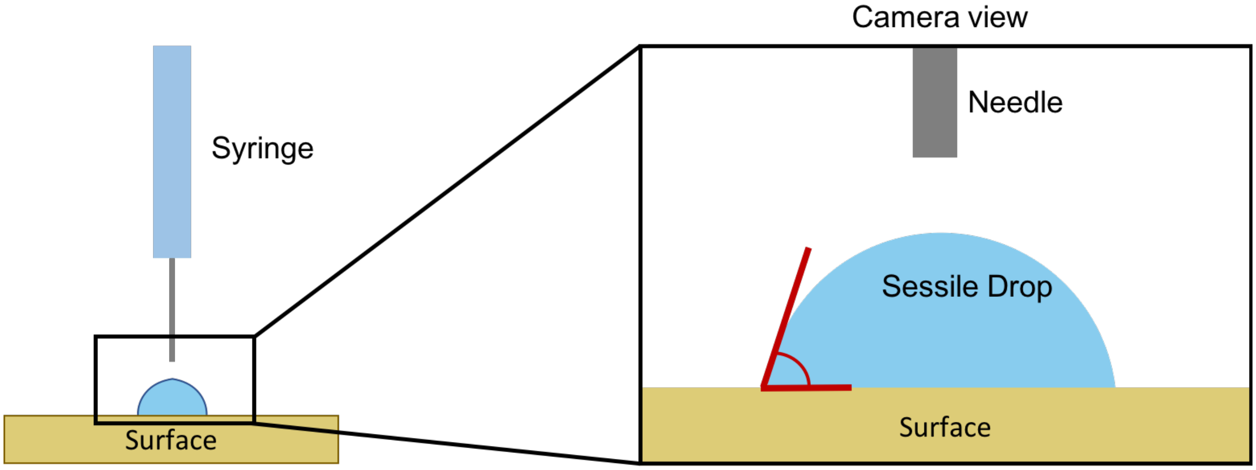

Figure 1-9: Instrument set-up for sessile drop data (left). The contact angle can be measured from a picture of the sessile droplet (right).

Chapter 2. WETTABILITY PROJECT SUMMARY

In order to resolve the mechanisms controlling soil wettability, I chose to work with a simple model system of one inorganic component (clay) and one organic component (phospholipids). My goal was to determine the roles of lipid melting temperature and lipid head-group chemistry in changing the wettability of montmorillonite clay. I accomplished this by using lipids with contrasting chemistry and a suite of experimental techniques.

2.1 MODEL SYSTEM

I chose to work with long-chain phospholipids and the clay montmorillonite. I selected montmorillonite because clay has been used to remediate water-repellent sandy soils in the past[41]. For the phospholipids, I selected phosphoethanolamine (PE) and phosphoglycerol (PG) lipids that I expected to be present in soils due to their prevalence in bacterial cell membranes[42,43]. The majority of my thesis will focus on PE and PG lipids; see **Section 7.1** for preliminary data on phosphocholine (PC) lipids.

These lipids allowed me to rigorously determine the relative effects of *lipid melting temperature* and *lipid-clay binding* on wettability. I selected the two headgroups, PE and PG, because PE is zwitterionic and binds to the negatively-charged montmorillonite surface, whereas the negatively-charged PG lipids do not bind. Therefore, I was able to easily compare the effects of lipid-clay binding on wettability. To compare the effects of melting temperature (e.g., whether the lipids were in a solid or liquid phase) on wettability, I chose two lipid tails per headgroup, one saturated lipid and one unsaturated lipid. These characteristics are summarized in **Table 2-1** and **Table 2-2.**

Table 2-1: Lipid properties.

Lipid Name	**Lipid Headgroup**	**Headgroup charge**	**Binds to clay surface?**	**Tail**	**State at room temperature**
DSPE 1,2-distearoyl-sn-glycero-3-phosphoethanolamine	PE	(+)/(—)	Yes	Saturated 18 Carbon	Solid
DOPE 1,2-dioleoyl-sn-glycero-3-phosphoethanolamine	PE	(+)/(—)	Yes	Unsaturated 18 Carbon	Liquid
DSPG 1,2-distearoyl-sn-glycero-3-phospho-(1'-rac-glycerol)	PG	(—)	No	Saturated 18 Carbon	Solid
DOPG 1,2-dioleoyl-sn-glycero-3-phospho-(1'-rac-glycerol)	PG	(—)	No	Unsaturated 18 Carbon	Liquid

Table 2-2: Lipid-montmorillonite binding characteristics and physical state at room temperature.

	Liquid	**Solid**
Binds to surface	DOPE	DSPE
Does not bind	DOPG	DSPG

In order to compare the results of my saturated PE lipid and my unsaturated PE lipid, it was necessary to introduce a third category of PE: a film of montmorillonite and DSPE that was prepared above DSPE's melting temperature. This category of PE will be referred to as "heated" or "melted" DSPE. The lipid distribution of melted DSPE in the film matched that of the unsaturated DOPE, and allowed direct comparison of the wettability without needing to account for a different distribution of lipid in the film[44] **(see section 2.3.1.3)**.

2.2 EXPERIMENTAL DETAILS

Chapter 3 contains detailed protocols for each technique summarized below, and Chapter 1 describes how each technique works in more detail. Methods were selected to encapsulate detail in the system from the molecular level, to the nanoscale, to the microscale, to the macroscale wettability.

2.2.1 *Sample preparation*

Each sample was prepared with the same procedure. Lipids were suspended in water, then mixed into aqueous suspensions of montmorillonite at known concentrations. Concentrations were calculated as the hypothetical, maximum coverage possible if the lipids covered the clay surface in a uniform bilayer:

$$\% \, Coverage = 100 * \frac{total\ lipid\ surface\ area}{total\ montmorillonite\ surface\ area} \qquad \text{2.1: Lipid coverage.}$$

The mixed lipid-clay solutions were then pipetted onto a freshly-cleaved mica surface and allowed to dry overnight.

2.2.2 *Molecular dynamics simulations*

At the smallest scale, the structure of the lipid aggregates and how those aggregates interacted with the clay surface was determined with simulations. These simulations were run by Dr. Nihit Pokhrel. For details, please see **Chapter 4**.

2.2.3 *Atomic force microscopy*

With AFM, I was able to directly image lipid aggregates on the clay surface and find the overall film topography. To accomplish this, I performed atomic force microscopy at two scales: tens of nanometers and tens of microns, using an Asylum Cypher ES and a Bruker ICON respectively. See section **2.2.3** for more detail on AFM.

2.2.4 *Fluorescence microscopy*

By incorporating a fluorescent lipid into the original lipid suspension, I was able to selectively stain the lipids. The fluorescence micrographs therefore are bright where there is more lipid and darker where there is less lipid. This technique efficiently captured the lipid distribution through the film over the scale of hundreds of microns. See also section **2.2.4**.

2.2.5 *Contact angle and droplet dynamics*

All wettability data was collected by setting a droplet of water on the samples, filming as it spread across the surface and imbibed into the sample, and then using custom MATLAB and Python scripts to extract the contact angle and radius over time. Please see sections **1.2.2** and **1.3.3** for a more detailed discussion of wettability, and Appendix A for the analysis scripts.

2.3 CHARACTERISTICS MEASURED

In order to determine how the lipids changed the overall wettability, I collected two types of characteristics: physical characteristics of the film and wettability characteristics. Physical characteristics consist of film parameters such as the lipid distribution through the film, while wettability refers to variables that define how water absorbs into the film. All variables are listed in **Table 2-3** and explained in the subsections.

Table 2-3: Categorization of experimental variables.

Wettability variables	**Physical variables**
Contact angle	Aggregate area density
K (1/TC)	Aggregate fraction on clay edges
a	Film topography
	Lipid distribution through the film

2.3.1 *Physical variables*

2.3.1.1 Lipid aggregates

At the smallest scales, simulation results and atomic force microscopy data provided information on how lipid aggregates interacted with the montmorillonite surface. From simulations, my co-authors predicted that the lipids should form spherical or cylindrical micelles or bilayer sheets in solution. Simulations results also showed that, in solution, PE lipids spontaneously adsorbed to the montmorillonite surface, while PG lipids did not[45] **(Figure 2-1).**

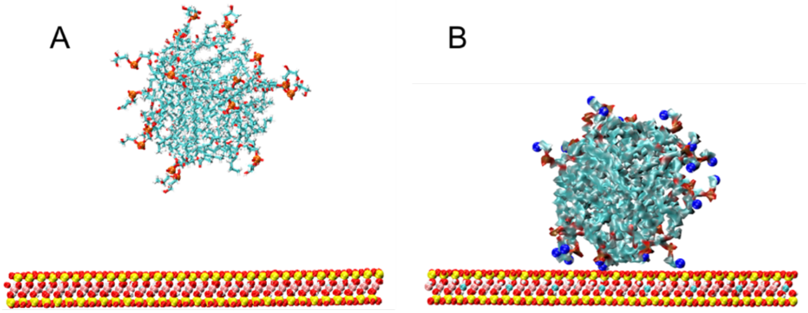

Figure 2-1: Lipid aggregate behavior in solution. A) PG lipid aggregates do not adhere to the clay surface[45]. B) PE lipid aggregates bind to the surface[44].

AFM topography and phase imaging showed the presence of small, roughly circular aggregates on the film surfaces. In some cases, the lipids instead formed bilayer sheets, identified by their characteristic height of 4-6 nm **(Figure 2-2)**.

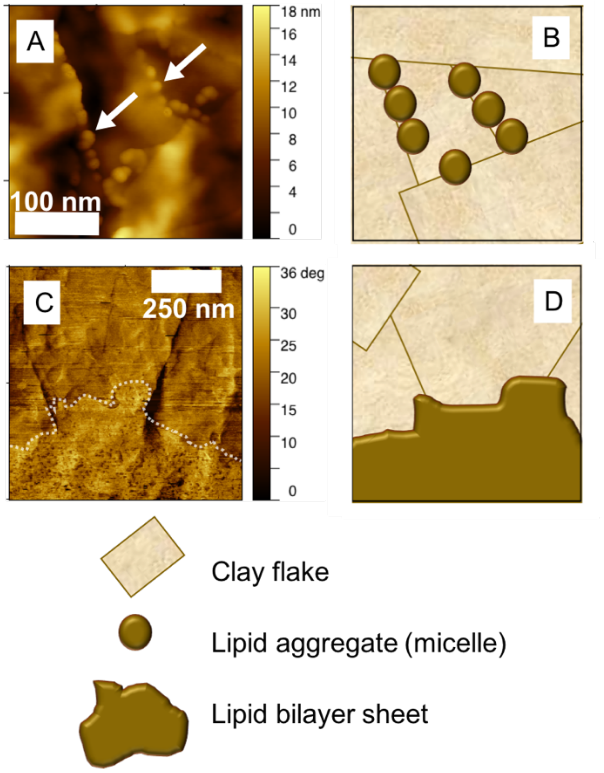

Figure 2-2: The main morphologies of lipids on the film surface and associated cartoons. (A) and (C) are both DSPG samples, but are representative of the morphologies observed for all lipids. A) Circular aggregates, in this case present along the edges of montmorillonite flakes, with a simplified representation in (B). C) An AFM phase image with a dotted outline along the edge of a bilayer lipid sheet, simplified in (D). Reproduced from Kessenich *et al.* 2020[45].

In the case of the small circular aggregates, I quantified their size, density, and the fraction that adhered to the edges of the clay flakes relative to the total number of aggregates. These characteristics are summarized in **Table 2-4**. The aggregate diameter falls between 4 and 14 nm for every lipid, though the liquid lipids tend to be denser, having a surface density on the order of 0.001 aggregates/nm^2 while the solid lipid density typically is on the order of 0.0001 aggregates/nm^2. With the exception of DOPE, higher concentrations of lipid are observed at clay edge sites.

Table 2-4: Lipid aggregate characteristics.

Lipid	Percent coverage	Average diameter (nm)	Diameter StDev (nm)	Aggregate/nm^2 estimate	Edge/total aggregates
DOPE	10	9.2	2.3	0.0010	0.10
	26	4.8	0.75	0.1684	0.22
	30	9.5	1.5	0.0023	n/a no visible edges
	40	8.0	1.5	0.0048	0.21
	50	7.1	1.1	0.0102	0.24
DSPE	10	9.4	1.5	0.0004	0.85
	26	6.9	1.6	0.0006	0.86
	30	8.5	1.4	0.0008	0.98
	40	12.5	2.3	0.0003	1.00
	50	Forms bilayer film			
DSPE heat	10	13.6	2.9	0.0007	0.74
	26	10.3	2.0	0.0009	0.97
	50	10.2	2.3	0.0119	0.17
DOPG	10	11.7	2.7	0.00020	0.89
	26	7.9	1.8	0.00111	0.80
	50	6.6	1.2	0.00200	0.11
DSPG	10	11.8	2.1	0.00077	1.00
	25	13.3	2.6	0.00041	0.97
	30	5.4	1.3	0.00349	0.92
	40	Forms bilayer film			
	50	Forms bilayer film			

2.3.1.2 Film topography

The surface topography of a material has potential to alter its wettability, usually by trapping air within folds on the surface. Therefore, I used a different AFM to collect 50×50 micron topography images of the lipid/clay films.

Quantifying these images posed a challenge. In order to preserve as much detail in the grayscale topography images as possible, I developed an analysis protocol as follows **(Figure 2-3)**.

First, in order to capture as much detail from the images as possible, I made three binary images per micrograph. The binary thresholds were selected as 25%, 50%, and 75% of the total gray values, such that the 25% threshold made all gray values below the 25th percentile white, and made the top 75% dark, and so on. Then each binary image was skeletonized. Skeletonization reduced each dark region to a single-pixel-wide line down the center of the region. Therefore, the 25% threshold preserved the most detail in the skeletonized image, and the 75% threshold preserved the least, as only the topmost 25% of the image was skeletonized. From this, I could determine which part of the film had the most influence on wettability.

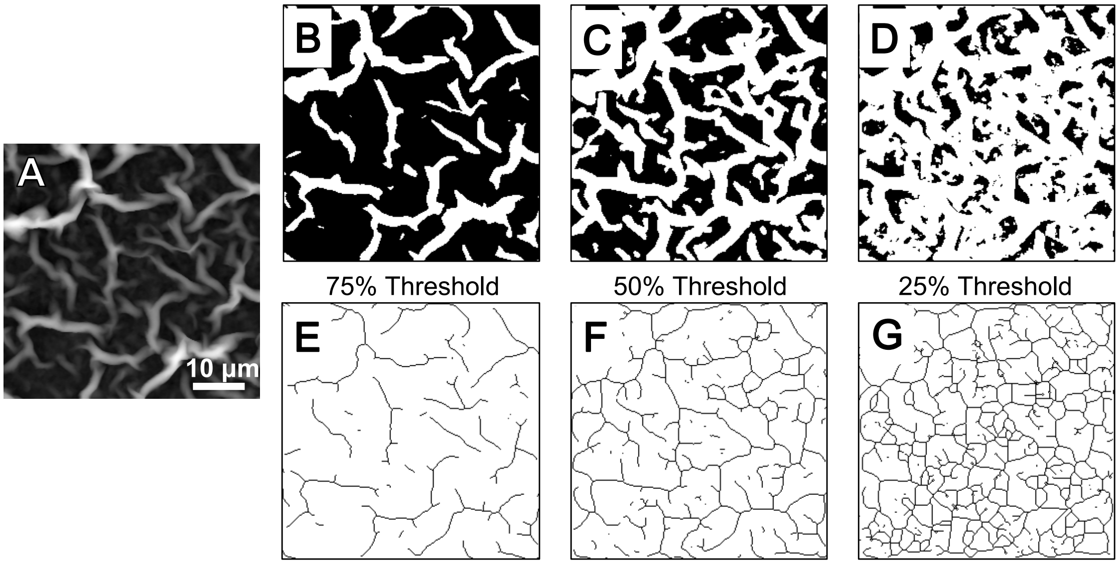

Figure 2-3: Example of image processing. A) Original grayscale AFM topography image. B) 75% binary threshold. C) 50% binary threshold. D) 25% binary threshold. E) skeletonized 75% threshold. F) skeletonized 50% threshold. G) skeletonized 25% threshold. Reprinted from Kessenich et al 2019[44].

Once skeletonized, the figures were quantified using two variables. The first, "junction density", is the number of pixels where the skeletonized lines meet, normalized to the number per square micron. The second, "skeleton ratio", is simply the ratio of dark to light pixels in the skeletonized image. For the film texture AFM images, these variables indicate the connectivity of the ridges on the film surface and could be related to the number of valleys that could form air pockets during wetting.

2.3.1.3 Lipid distribution

How organic material is distributed through soil is a long-standing and largely unresolved question[6]. To determine the lipid distribution in my model systems, I introduced a small quantity of fluorescent lipid into my samples. This allowed for the collection of fluorescence micrographs that were bright in areas with more lipid and dark in areas with less lipid **(Figure 2-4)**. I found that most of the lipids I studied were distributed throughout the film, except for DSPE, which instead was only present in isolated islands. For the distributed lipids, the brightness forms a similar pattern to the ridges in the film texture.

These fluorescence micrographs were quantified the same way as the film texture AFM images (see previous section). In this case, the junction density and skeleton ratio variables are proportional to the relative distribution of the lipids in the fluorescence micrographs. At the 75% binary threshold, the skeleton ratio agrees within error with the AFM 25% binary threshold values **(Table 4-3)**.

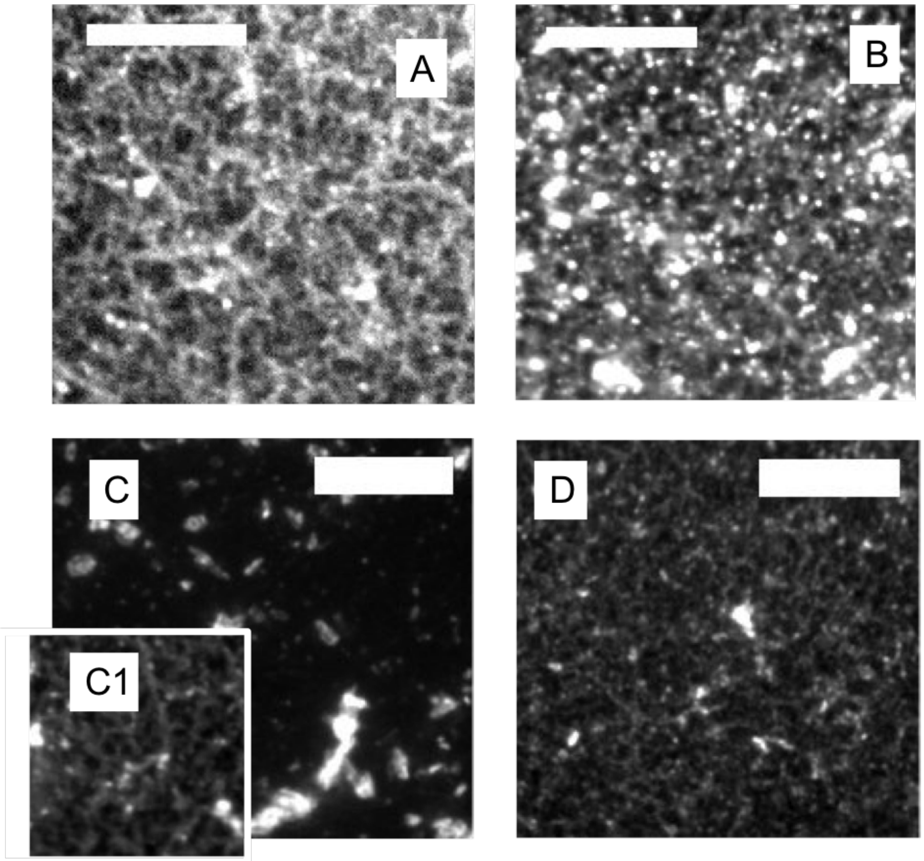

Figure 2-4: Fluorescence indicating lipid distribution. A) DSPG[45], B) DOPG[45], C) DSPE[44], C1) Melted DSPE[44] (note: same scale as C), D) DOPE[44]. All scale bars are 50 µm.

2.3.2 *Wettability variables*

2.3.2.1 Initial contact angle

Typically, the contact angle of a water droplet on the sample surface is used to define wettability in soil science. I collected this data for all samples **(Figure 2-5A)**. Note that a higher contact angle corresponds to a more hydrophobic surface. The melted/heated DSPE clearly changes the contact angle the most, with the PG lipids having the least effect.

Contact angle is connected to the surface energy of a material and can be complicated by surface topography. Contact angle also provides no information on the kinetics of water absorption into the material or water spreading across the surface. Therefore, I found it necessary to also monitor the droplet's shape over time in order to obtain kinetic information, as detailed in the next section.

2.3.2.2 Flow parameters K and a

Other than the initial contact angle, another common method of measuring wettability in soil science is the Water Droplet Penetration Time test (WDPT). However, its quantification rests on measuring the time required for a water droplet to be absorbed by the sample, which seemed subjective. For a more quantitative approach of defining the infiltration time of a water droplet, as detailed in Chapter 1, I analyzed the kinetics of droplet imbibition in my system with the following equation based off the work of Chao et al for a droplet of initial radius R_0 (**Equation 1.5**, reprinted here for clarity):

$$\frac{R}{R_0} = [1 + Kt]^a$$

The key variables I used to define wettability are the rate constant of imbibition *K,* which is the inverse time constant *TC,* and the parameter *a,* which relates to the fluid index or viscosity of the infiltrating liquid. Note that Newtonian fluids have a constant viscosity that does not change under stress. Newtonian fluids therefore have a fluid index $n = 1$, and non-Newtonian fluids have $n \neq 1$. In Eqn. 1, a is related to n by **Equation 1.7**:

$$a = \frac{n}{1 + n}$$

For further discussion of these equations, see sections **1.2.3** and **4.2**.

All of the a values calculated for the lipid/clay systems were consistent with a non-Newtonian, shear-thinning liquid (i.e., the liquid is *less* viscous when under strain). This was true also in the case of a pure montmorillonite film. In summary, *a* and *K* show if and how the lipids change the speed at which the droplet soaks into the film, and how they change the fluid viscosity during imbibition **(Figure 2-5)**.

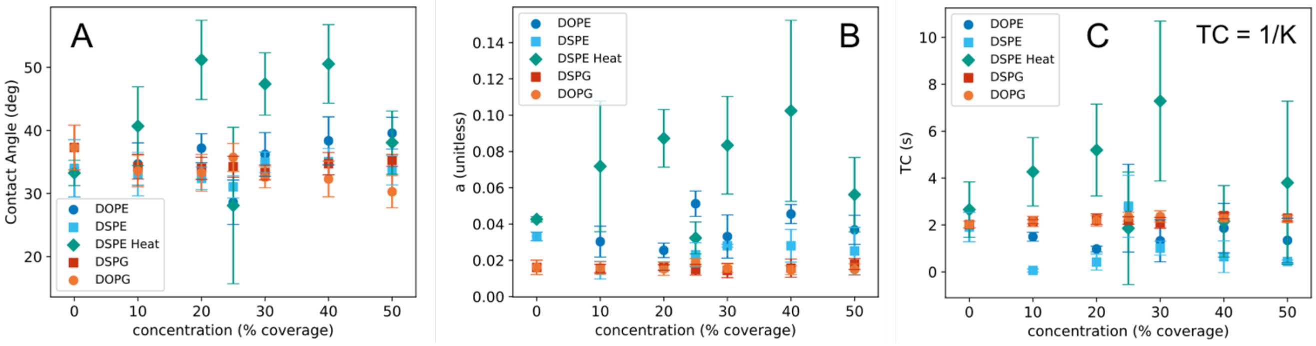

Figure 2-5: Measured wettability characteristics for lipid-clay systems. A) Contact angle. B) Fluid index proxy *a*. C) Time constant of imbibition, or 1/K. Error bars represent standard deviations. Reprinted from Kessenich *et al.* 2020[45].

Again, melted/heated DSPE causes the largest alteration in the wettability, this time by increasing the viscosity (higher *a*) towards that of bulk water and slowing down the flow during imbibition (higher TC) due to this higher viscosity.

2.4 DETERMINING THE CAUSE OF WETTABILITY CHANGES

As noted above, melted/heated DSPE causes the largest changes in all three wettability variables. Among the lipids tested, heated DSPE has the following unique combination of characteristics: it is solid, distributed through the film, binds to the mineral surface, and is found dominantly on the edge of montmorillonite flakes **(Table 2-5)**.

Table 2-5: Summary of lipid characteristics in a lipid-montmorillonite system.

Lipid	Binds to surface	Distributed through film	Solid at RT	Edge fraction >80%
Heated DSPE	**X**	**X**	**X**	**X**
DSPE	**X**		**X**	**X**
DOPE	**X**	**X**		
DSPG		**X**	**X**	**X**
DOPG		**X**		**X**

In order to determine the importance of lipid distribution and aggregate behavior, I identified linear relationships between physical variables and wettability variables by collecting the characteristics listed above at several concentrations of phospholipid (typically 10%, 25%, and 50% coverage), then plotting physical variables along one axis, wettability variables along the other, and obtaining a line of best fit through the points **(Figure 2-6)**.

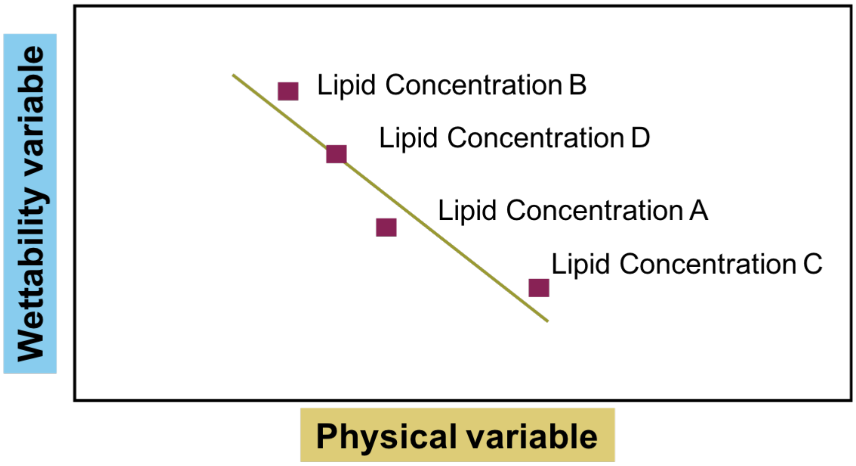

Figure 2-6: How linear fits were generated for wettability and physical variables.

I then identified the linear fits with the highest quality of fit (defined as an r^2 value greater than 0.8) and individually plotted each of those correlations. From there, I hypothesized potential reasons for a causative relationship between the physical and wettability variables. These results are summarized in **Table 2-6**.

For PE lipids, the overall lipid distribution through the film contributes the most to changing the wettability. I hypothesize that this is likely due to the lipids changing the spacing between individual montmorillonite flakes, and therefore the ability of water to flow between the flakes. Given that for heated DSPE, the lipid distribution correlated with wettability variables and the aggregate characteristics and topography did not, the lipid distribution likely has more influence on the wettability than aggregate characteristics. Revisiting DSPE's unique combination of characteristics, I conclude that the aggregate edge fraction likely does not change wettability, and the key characteristics are that heated DSPE is 1) solid, 2) distributed through the film, and 3) binds to the mineral surface.

While at first glance PG lipids appear to change the wettability via their aggregate characteristics, the r^2 value of the linear fits is misleading. The PG lipids barely change the wettability, and the linear fits do not mean much once the error bars are taken into account.

Table 2-6: Correlations of wettability variables with physical variables for the different lipids. Categories with r^2 values greater than 0.8 are marked with an X and shaded.

	Contact Angle/TC/a				
	Binds to surface			Does not bind	
	DOPE	DSPE	Heated DSPE	DOPG	DSPG
Aggregate characteristics	**x**	**x**		**x**	**x**
Lipid distribution	**x**		**x**		
Topography	**x**	**x**			

2.5 SUMMARY AND CONCLUSIONS

Overall, I found that PE lipids affected the wettability of lipid-montmorillonite films far more than PG lipids. Within the PE lipids, the heated DSPE had the largest effect. The fact that the non-binding PG lipids do not change wettability verifies findings as far back as 1988 that illustrate that waxes do not change wettability because the waxes do not bind to the minerals, whereas molecules with a moiety that could bind to the surface do change wettability[13]. More recently, these results support those of Cheng *et al*. 2010[18], who found a higher rise in contact angle associated with stearic acid (has a terminal COOH group that could bind to a surface) than with cholesterol or octadecane (nonpolar molecules without a binding moiety).

While the lipid aggregates do not appear to have much influence on wettability, these images provide unprecedented, direct visualization of how organic matter aggregates and binds to mineral surfaces.

Based on these results, I concluded that for these phospholipids, those that 1) bind to the montmorillonite surface, 2) have a distribution that is relatively continuous through the film, and

3) are solid at room temperature have the most pronounced effect on lipid/montmorillonite film wettability.

My publication on the PE lipids can be read in Chapter 4, and Chapter 5 contains my PG lipids manuscript.

Chapter 3. DETAILED METHODS

The purpose of this section is to lay out a detailed protocol for the soil wettability project, enabling others to exactly replicate the sample preparation process.

3.1 LIPID PREPARATION

Phospholipids were acquired either as powder or dissolved in chloroform. Powder lipids were dissolved in chloroform at known concentrations.

Proper storage of lipids in chloroform requires glass vials with Teflon caps or some other chloroform-safe material. For best results, the vials should be sealed first with a strip of Teflon sealing tape and then Parafilm, in order to minimize solvent evaporation **(Figure 3-1)**.

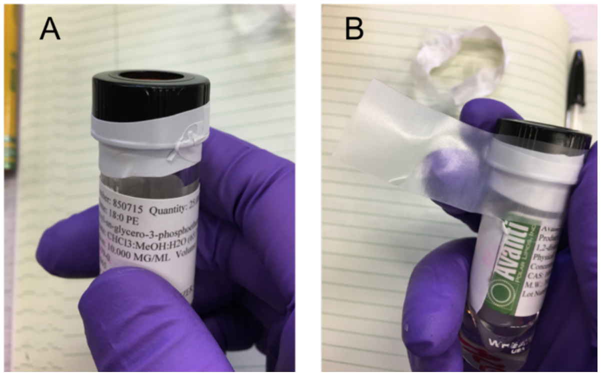

Figure 3-1: Teflon tape and Parafilm to prevent evaporation of chloroform. A) First, wrap the base of the vial cap in Teflon tape, then B) hold it in place with Parafilm.

To make aqueous lipid solutions, follow this altered gentle hydration protocol.

1. Clean a glass syringe for measurements. First rinse the needle with chloroform using a Pasteur pipette. Then fill and flush the syringe with chloroform ten times.
2. Allow lipid/chloroform solution to come to room temperature.

3. Measure out the desired quantity of lipid into a small test tube. The desired quantity should produce a 1 mM aqueous lipid solution.
4. Dry the lipid with compressed nitrogen gas. For best results, rotate the tube at a slight angle, to create a relatively even film of lipid at the bottom.
5. Put the lipid under vacuum for a minimum of one hour.
6. Add 18 MΩ water to the lipids. Put Parafilm over the tube and allow to hydrate uninterrupted for one hour.
7. Sonicate the lipids. For best results, line up the water level in the sonicator with the water level in the test tube.
    a. Depending on the lipid, different quantities of time are required to fully solubilize; up to 10-15 minutes may be necessary for DSPG.
    b. For lipids that are solid at room temperature, heating them to above their melting temperature before sonicating can be extremely helpful, with alternating 2 minutes of heating with 2 minutes of sonicating being ideal.
    c. Solubilization has been achieved when there is a cloudy or clear solution in the test tube, there is no visible dried lipid on the bottom of the test tube, and when vortexed, no visible chunks appear on the side of the tube.
    d. Some lipids, such as DOPC, go through two cloudiness stages: one where text cannot be read through the test tube, and one where text can be read through the solution. The second scenario is preferable.

3.2 Montmorillonite preparation

Montmorillonite suspensions may require determination of concentration. This can be done by measuring the weight of a glass slide, pipetting a milliliter of clay suspension onto the slide, and then drying it out (ideally overnight) and weighing again. Repeat three times for accuracy.

A concentration of 1 mg/mL is ideal for small-scale AFM imaging. 10-20 mg/mL is ideal for large-scale AFM imaging and wettability measurements. Sonicating the suspensions before measuring them out will ensure even distribution of the clay, which settles out over time.

3.3 Small-scale AFM sample preparation

This requires a 10 mm-diameter mica plate affixed to a metal/magnetic disk.

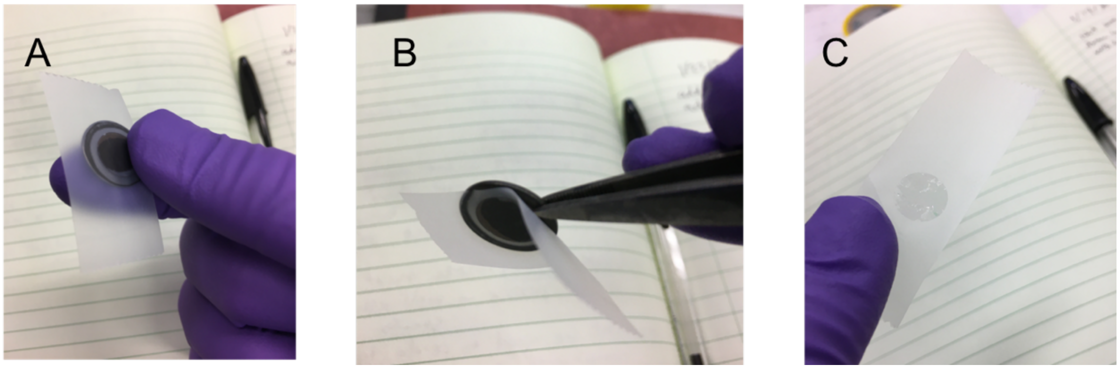

Figure 3-2: Cleaving mica. A) Press tape onto the mica plate. B) Firmly grasp the magnetic disk. C) Rip off the tape and check for a clean cleave, as seen here.

1. Calculate the ratio of lipid to clay desired.
2. Pipette out the 1 mg/mL montmorillonite suspension into a small test tube, taking care not to lose any to the sides of the tube.

3. Pipette in the lipid. Since this volume is typically quite small, pipette directly into the montmorillonite suspension. Vortex immediately.
4. Cleave the mica substrate with scotch tape. Aim for three complete cleaves. **(Fig. 3-2)**
5. Immediately before pipetting the lipid/clay mix onto the substrate, vortex it again for a couple of seconds. Then pipette out 30 µL. For even coverage of the mica plate, aim the tip of the pipette immediately above the center of the plate, and discharge smoothly in one motion.
6. Allow to dry in a dark, enclosed environment, such as in a box, overnight.

3.4 LARGE-SCALE AFM SAMPLE PREPARATION, FLUORESCENCE, AND WETTABILITY SAMPLES

These are prepared exactly the same way as in 2.3, but should be done with larger (20 mm diameter) mica plates glued to glass slides and 16 mg/mL clay. The volumes handled will be larger as well (100 µL lipid/clay suspension per mica plate). It is best to prepare the lipid solutions in 100 µL increments; larger quantities are difficult to dry and hydrate.

For fluorescent samples, add 1 mol% membrane-specific/lipid dye to the lipids. If the dye is in chloroform, add it to the lipids in chloroform at the beginning. Keep the samples in the dark to prevent bleaching of the dye; this is easily accomplished by wrapping the test tubes in tin foil during vacuum desiccation and rehydration.

For wettability measurements, prepare two 20 mm mica plates for each concentration. This will provide enough surface to obtain three droplet videos per plate for a minimum of six data points per concentration.

3.5 NOTE ON HEATED/MELTED DSPE

Section 2.3 steps 2, 3, and 5 should be performed above DSPE's melting temperature. I did this by setting the substrates on top of a heating block. Once step 5 was completed, the suspensions were allowed to dry on top of the heating block as well, then removed and stored/imaged/measured at room temperature. Do not leave the samples on the heating block for longer than the few minutes it takes to dry them out.

3.6 WETTABILITY MEASUREMENTS AND ANALYSIS

Use of an instrument with automated droplet placement is essential for acquiring wettability data (I used a Kruss DSA100). Droplets of uniform volume must be placed on the surface with the same force each time for comparison. Five droplets per lipid concentration is ideal.

Videos of each droplet should run for about a minute, and can be collected at 2-5 frames per second. These videos will then be processed through the Contact Angle Systematic script **(Appendix A)**, which extracts contact angle and droplet radius for each frame of the video.

The droplets typically have a "pinched" edge. The tangent line used to extract the contact angle should be adjusted to start above the pinch, so that the overall contact angle of the droplet is measured **(Figure 3-3)**.

Figure 3-3: Example of a sessile drop on a surface, with the contact angle marked by a red line.

3.7 NOTES ON ASYLUM CYPHER AFM IMAGING

Lipid/clay films are soft. Correspondingly, use of tapping mode and cantilevers with a 2 N/m spring constant is recommended for tapping mode topography in air.

1. Put the sample in instrument. Center the area of interest.
2. Add the holder/tip.
3. Manually move tip close to surface (within a few millimeters) with the knob on the front of the Cypher.
4. Move to the computer.
5. Right click the end of the tip and click "Spot on" to center the laser on the tip.
    a. If the tip isn't initially visible, click "home" and move the focus on tip to get in right area.
    b. A SUM value of 7-10 is ideal. Less indicates that the tip may be bent, and therefore isn't reflecting the laser back on to the photodiode.
    c. Hold the Shift key and click the arrows in the video screen to finely manipulate the laser position.

6. Once the laser has been centered on the tip, click “Set tip position”.
7. Move the focus down until either the sample surface is in focus, or the aperture’s shadow becomes sharp/in focus. Move the focus up a few clicks and click “Set sample position”.
8. Click “Move to Pre-Engage”.
9. Click “Zero PD”.
10. Open the Tune menu and do one tune with a range of 25 or so to find the main peak. (If the peak isn’t initially visible, open the “Thermal” window and right-click “Set drive frequency” from the 1st thermal peak.) Tune once again with a range of 5 and center the phase.
    a. Use the left side of the peak for repulsive regime, right side for attractive.
11. Change the Drive Amplitude. For these soft samples, a free amplitude of 150-300 mV is a good place to start.
12. Change the set point to 80-90% of the free amplitude.
13. Click Start Tip Approach.
14. Set the scan size to 2 µm and scan rate to 1.2 Hz, then click Frame Down.
15. Engage? Z will go all the way to 0 or 10 if not engaged; best is somewhere near the middle. The blue and red tracking lines should also match each other when engaged.
16. If engage and tracking are not achieved, lower the set point, and repeat 15-17 until Engage occurs. This may be down to a 50% set point.
17. Raise the gain for more resolution, and/or toggle the set point.
18. If achieving tracking/imaging is difficult:
    a. First try imaging a different location or a smaller scan size.
    b. If difficulty persists, bring the tip back to Pre-Engage and re-tune.

   c. Check if the free amplitude has changed and adjust the drive amplitude accordingly.
   d. Sometimes altering the cantilever position in the holder can fix imaging problems.
   e. If none of these actions improves imaging, use a new tip.

3.8 NOTES ON LARGE-SCALE AFM IMAGING (BRUKER ICON)

In order to get good resolution at the 50x50 micron scale, a scan rate of 0.1 Hz is ideal. Achieving excellent tracking will also require adjusting the set point and gain. Acquiring one image takes 40 minutes; bring a book.

3.9 IMAGE ANALYSIS: SKELETONIZING FLUORESCENCE AND AFM LIPID/CLAY DATA

1. Save all AFM images as 16-bit grayscale TIFFs, ensuring all have unique names.
2. Adjust the file paths in the binary_threshold.py script **(Appendix A)** and run. This script splits each image into three binary images, with the binary threshold at 25% of the total grayscale values for the first image, at 50% for the second, and 75% for the third.

a. Manually adjusting the thresholds can be done in ImageJ as follows:

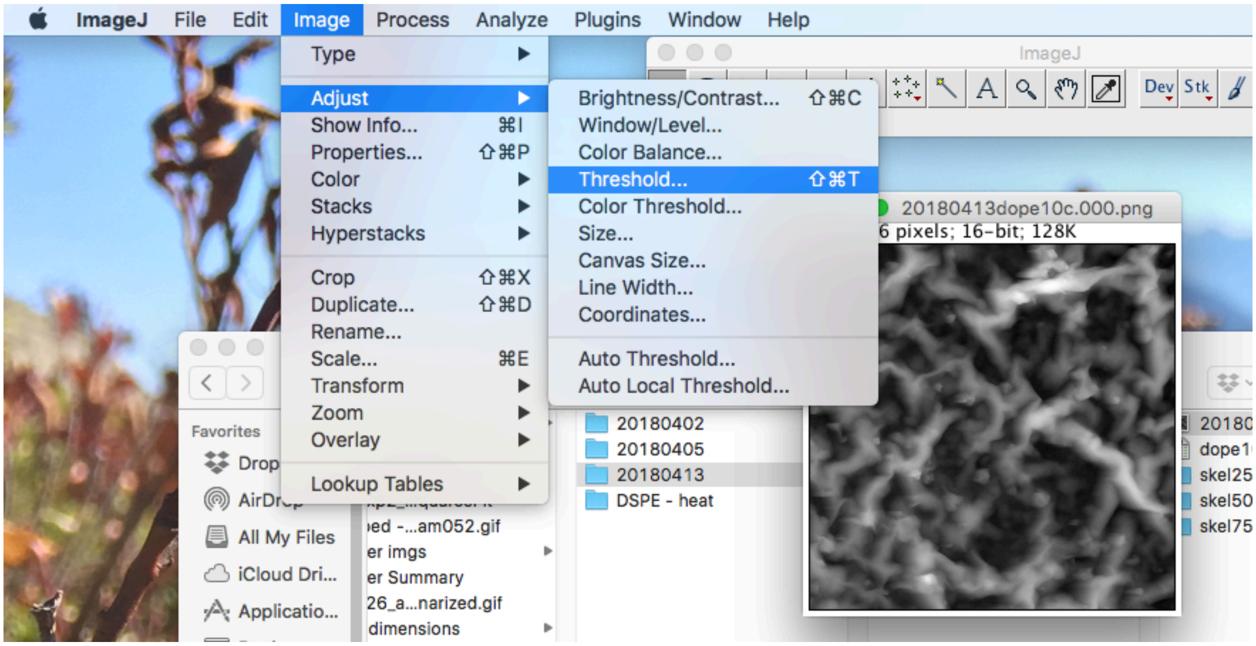

Figure 3-4: Adjusting the binary threshold in ImageJ.

i. Go to Image > Adjust > Threshold.

ii. This will open a histogram of gray values in the image. Check “Dark Background.” Adjust the sliders as shown, such that the percentage shown is as close to 25% as possible. (Note that at 25% of the histogram, you have made the top 25% of the image black, and the bottom 75% white. I call this a 75% threshold.)

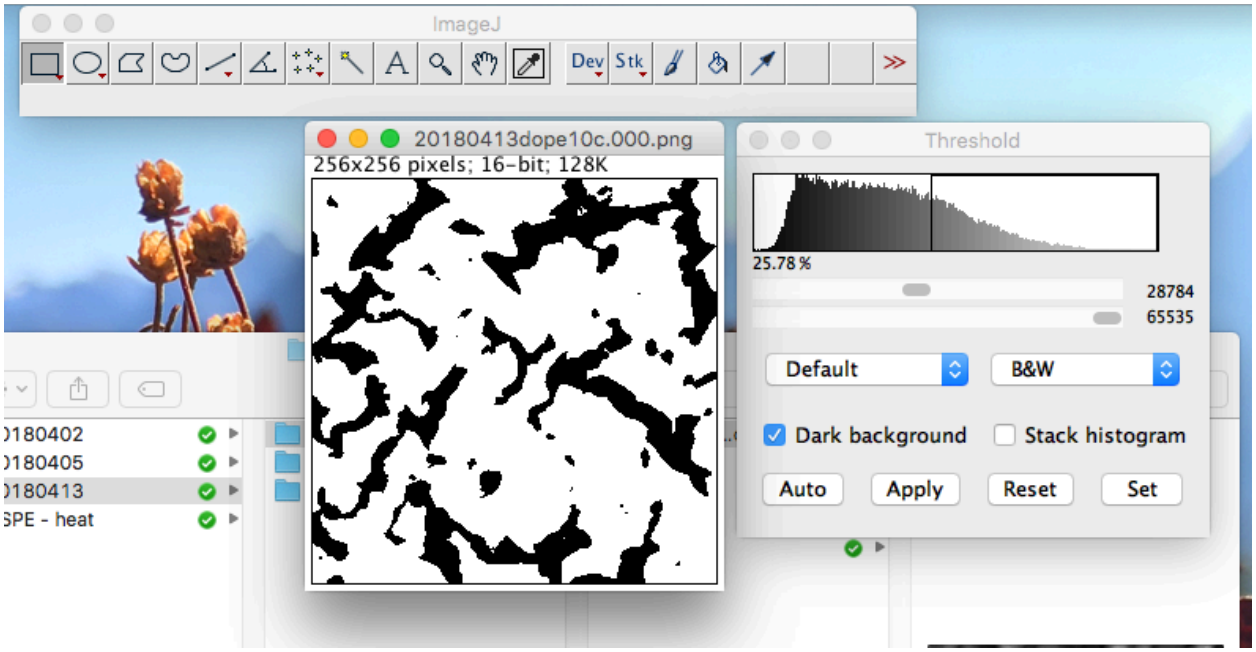

20180413dope10c.000.png

256x256 pixels; 16-bit; 128K

25.78 %

28784

65535

Default

B&W

☑ Dark background

☐ Stack histogram

Figure 3-5: The result of applying a binary threshold in ImageJ.

iii. Click “Apply.”

iv. Save the new, binarized image as a TIFF. Name it simply by adding “_bin75” to the original filename.

3. Open the binary images in Image J. For each, skeletonize by clicking Process > Binary > Skeletonize.

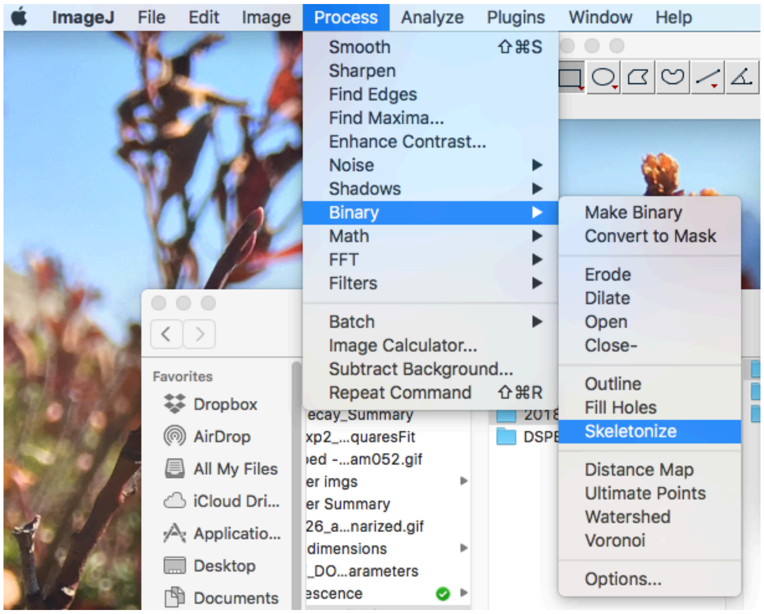

Figure 3-6: How to skeletonize an image in ImageJ.

4. Refer back to the original image and make sure the lines in the skeleton match up with the brightest portions of the original. Save the skeletonized image as a TIFF; name it by adding "_skel" to the filename.

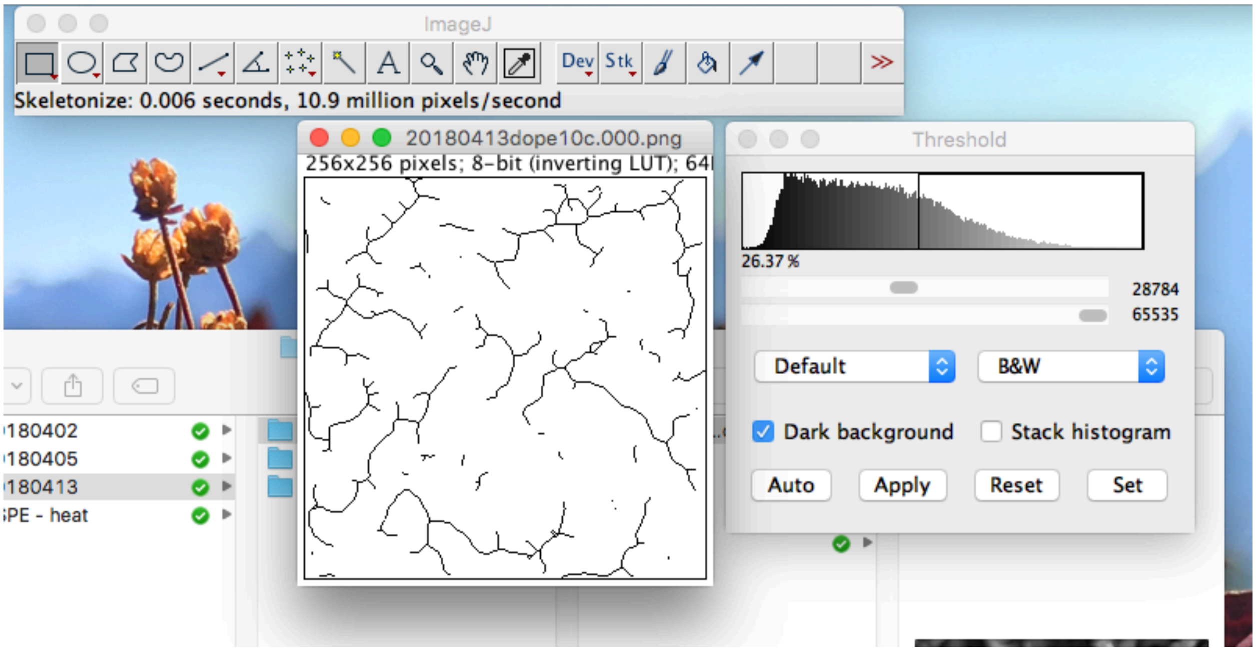

Skeletonize: 0.006 seconds, 10.9 million pixels/second

20180413dope10c.000.png
256x256 pixels; 8-bit (inverting LUT); 64

26.37 %
28784
65535
Default
B&W
☑ Dark background
☐ Stack histogram

Figure 3-7: The result of skeletonizing an image.

5. Install the "Analyze Skeleton" macro. To run it, go to Analyze > Skeleton > Analyze Skeleton.

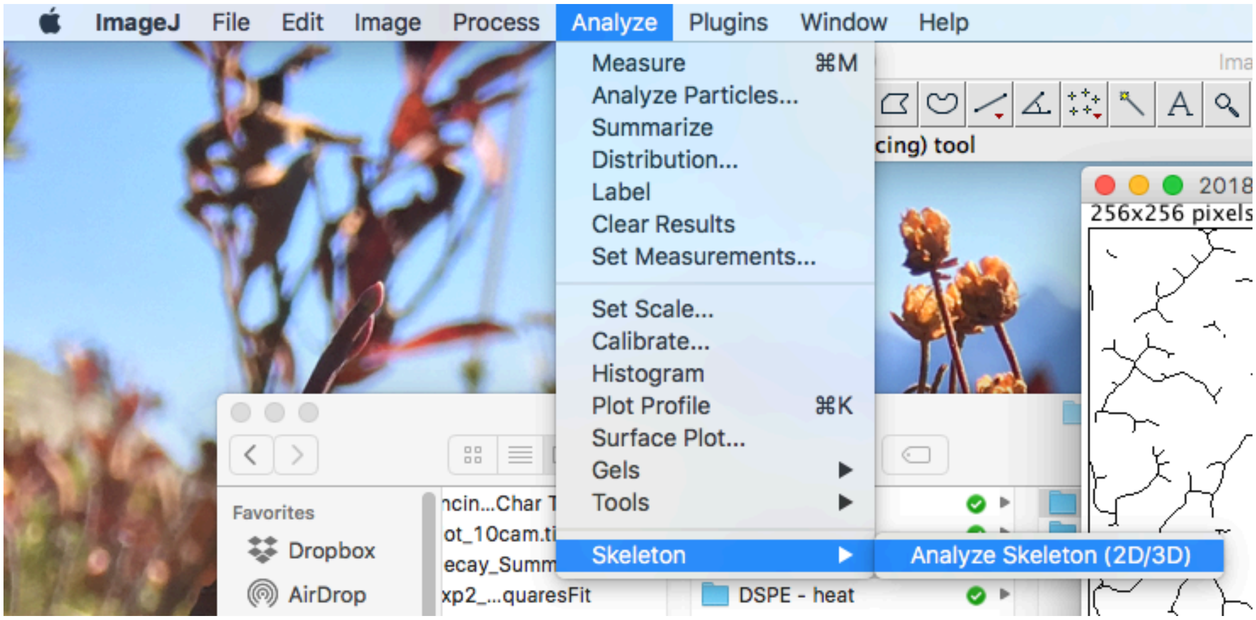

Figure 3-9: Where to find the Analyze Skeleton macro.

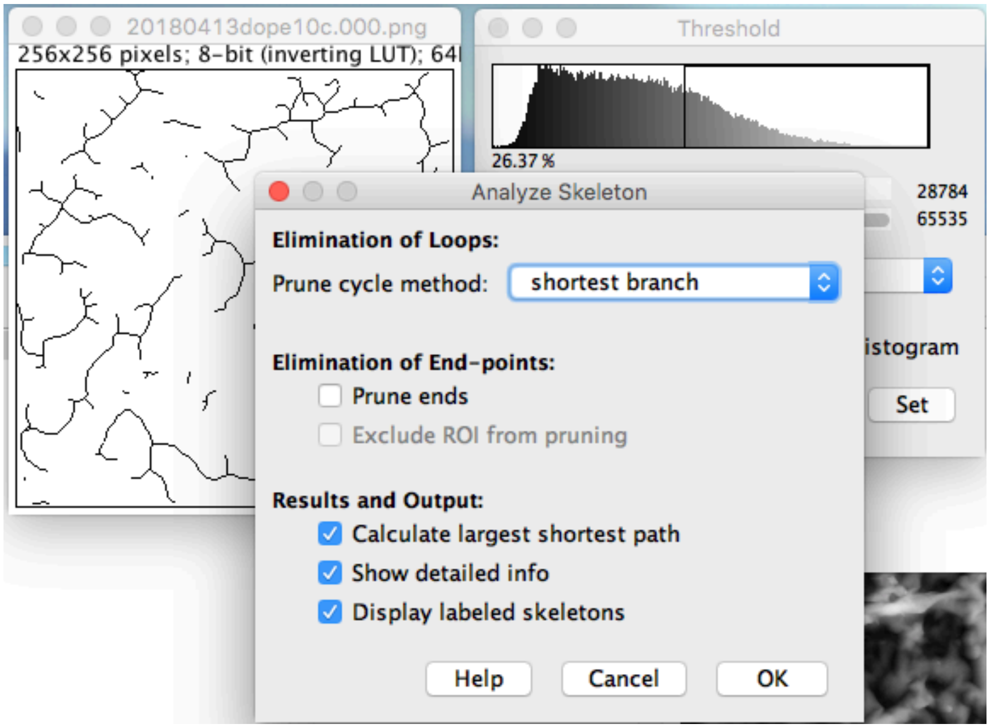

Analyze Skeleton

Elimination of Loops:

Prune cycle method: shortest branch

Elimination of End-points:

☐ Prune ends

☐ Exclude ROI from pruning

Results and Output:

☑ Calculate largest shortest path

☑ Show detailed info

☑ Display labeled skeletons

Figure 3-8: Setup of the Analyze Skeleton macro.

6. Set up the Analyze Skeleton as following:
7. Click “OK.” Find the window labeled “Results.” Save it as a CSV or Excel file; the only information needed is the column labeled “# Junctions.”

8. The resulting images should look like this, with the 75% threshold having the least number of lines and the 25% having the most:

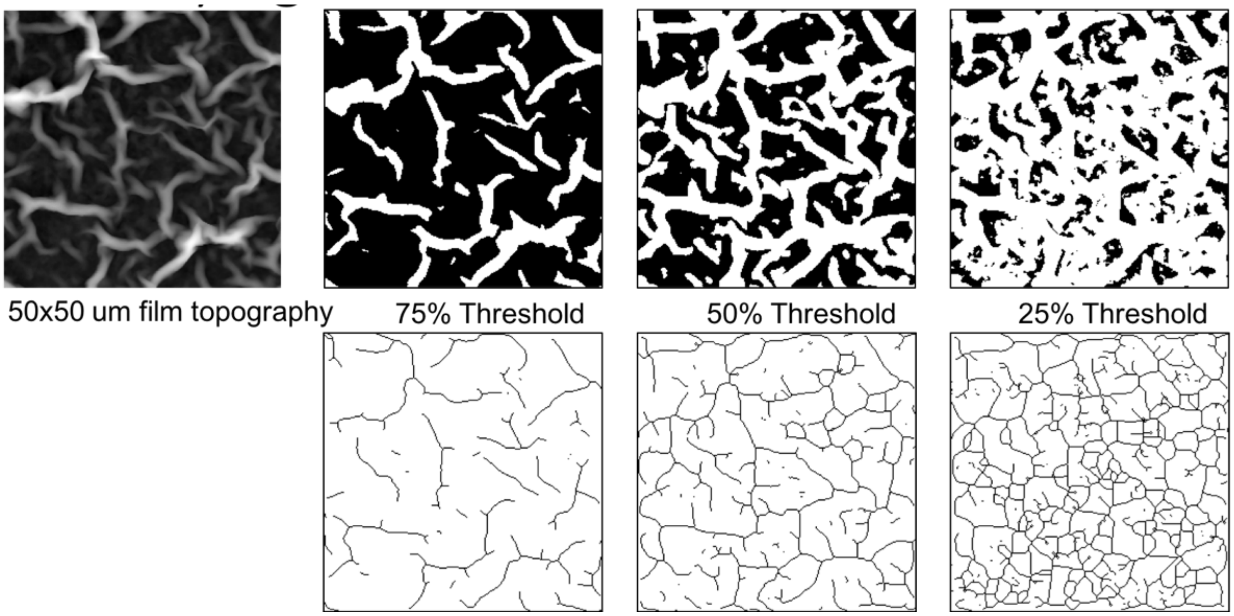

Figure 3-10: The results of processing one image.

9. Place all the skeletonized images in a folder and run them through the skeleton_loop.py python script to get the ratio of dark to light pixels in the skeletonized images. (Keep fluorescence vs. AFM images labeled as such. Otherwise images may wind up with the same names.)
10. Additional considerations for fluorescence data: first, crop out a chunk of the image that has even ‘illumination’ or focus. Otherwise, the binary images won’t have reliably “flat” thresholds.

Chapter 4. CONNECTING WETTABILITY, TOPOGRAPHY, AND CHEMISTRY IN A SIMPLE LIPID-MONTMORILLONITE SYSTEM

This chapter represents my first publication on the wettability project, and focuses on PE lipids. This is the final print version that was published in the Journal of Colloid and Interface Science in November 2019.

I personally carried out all the experimental work and most of the analysis presented in this paper. Dr. Nihit Pokhrel designed, ran, and analyzed the MD simulations.

4.1 MANUSCRIPT

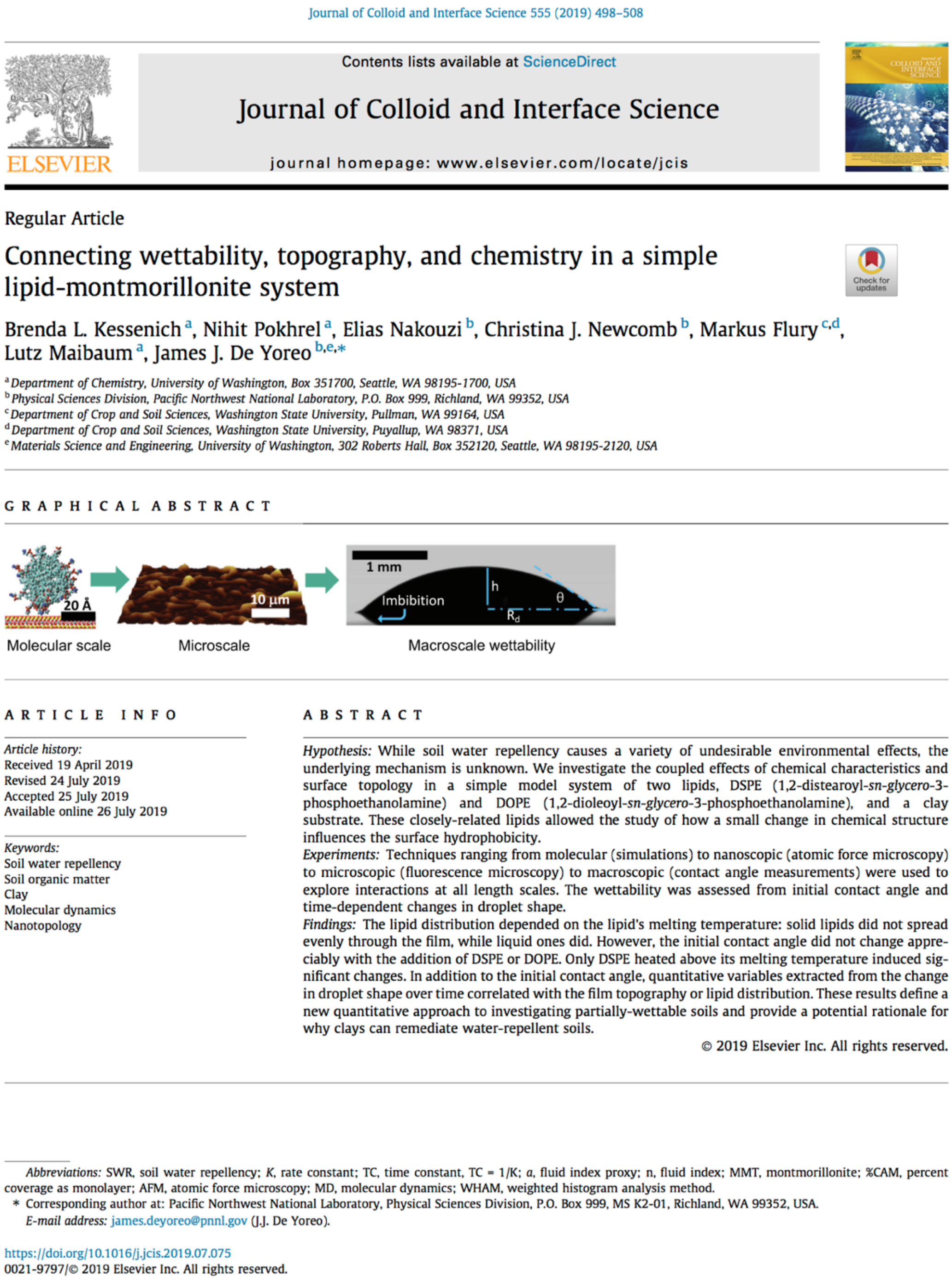

Journal of Colloid and Interface Science 555 (2019) 498–508

Contents lists available at ScienceDirect

Journal of Colloid and Interface Science

journal homepage: www.elsevier.com/locate/jcis

Regular Article

Connecting wettability, topography, and chemistry in a simple lipid-montmorillonite system

Brenda L. Kessenich [a], Nihit Pokhrel [a], Elias Nakouzi [b], Christina J. Newcomb [b], Markus Flury [c,d], Lutz Maibaum [a], James J. De Yoreo [b,e,*]

[a] Department of Chemistry, University of Washington, Box 351700, Seattle, WA 98195-1700, USA
[b] Physical Sciences Division, Pacific Northwest National Laboratory, P.O. Box 999, Richland, WA 99352, USA
[c] Department of Crop and Soil Sciences, Washington State University, Pullman, WA 99164, USA
[d] Department of Crop and Soil Sciences, Washington State University, Puyallup, WA 98371, USA
[e] Materials Science and Engineering, University of Washington, 302 Roberts Hall, Box 352120, Seattle, WA 98195-2120, USA

GRAPHICAL ABSTRACT

ARTICLE INFO

Article history:
Received 19 April 2019
Revised 24 July 2019
Accepted 25 July 2019
Available online 26 July 2019

Keywords:
Soil water repellency
Soil organic matter
Clay
Molecular dynamics
Nanotopology

ABSTRACT

Hypothesis: While soil water repellency causes a variety of undesirable environmental effects, the underlying mechanism is unknown. We investigate the coupled effects of chemical characteristics and surface topology in a simple model system of two lipids, DSPE (1,2-distearoyl-*sn-glycero*-3-phosphoethanolamine) and DOPE (1,2-dioleoyl-*sn-glycero*-3-phosphoethanolamine), and a clay substrate. These closely-related lipids allowed the study of how a small change in chemical structure influences the surface hydrophobicity.

Experiments: Techniques ranging from molecular (simulations) to nanoscopic (atomic force microscopy) to microscopic (fluorescence microscopy) to macroscopic (contact angle measurements) were used to explore interactions at all length scales. The wettability was assessed from initial contact angle and time-dependent changes in droplet shape.

Findings: The lipid distribution depended on the lipid's melting temperature: solid lipids did not spread evenly through the film, while liquid ones did. However, the initial contact angle did not change appreciably with the addition of DSPE or DOPE. Only DSPE heated above its melting temperature induced significant changes. In addition to the initial contact angle, quantitative variables extracted from the change in droplet shape over time correlated with the film topography or lipid distribution. These results define a new quantitative approach to investigating partially-wettable soils and provide a potential rationale for why clays can remediate water-repellent soils.

Abbreviations: SWR, soil water repellency; *K*, rate constant; TC, time constant, TC = 1/K; *a*, fluid index proxy; n, fluid index; MMT, montmorillonite; %CAM, percent coverage as monolayer; AFM, atomic force microscopy; MD, molecular dynamics; WHAM, weighted histogram analysis method.

* Corresponding author at: Pacific Northwest National Laboratory, Physical Sciences Division, P.O. Box 999, MS K2-01, Richland, WA 99352, USA.
E-mail address: james.deyoreo@pnnl.gov (J.J. De Yoreo).

https://doi.org/10.1016/j.jcis.2019.07.075
0021-9797/

1. Introduction

Soil contains a large, but poorly understood, carbon pool [1]. Soil organic carbon impacts many soil properties, including soil water repellency (SWR) [2]. Water repellent soils resist water infiltration and cause increased erosion [3,4], increased water overland flow [5], and decreased ability to support crops [6].

In spite of these environmental and agricultural impacts, a mechanistic understanding of SWR [7] is lacking, limiting the design of effective remediation protocols [8]. While there is an abundance of SWR field studies and investigations of natural organic matter [7,9] that has not been molecularly characterized [10,11], little work has been done on model surfaces with well-characterized compounds, with most focused on fatty acids [12–14]. Prior work with specific compounds has typically been done on quartz or quartz sands [13,15]. The results of these prior studies show that saturated fatty acids induce water repellency in sand, which tends to plateau after a critical amount of fatty acid has been added [12,14]. However, the clay fraction of soils has been found to be a key factor governing the rate of soil organic matter decomposition [16]; additionally, clays are sometimes mixed into hydrophobic sandy soils to ameliorate SWR [17] by an unknown mechanism [18]. Therefore, it is desirable to further explore the impact of clay-organic interactions on SWR.

The applicability of results from prior studies that imaged organics interacting with model mineral surfaces has also been limited because large flat surfaces were employed [7,8] rather than more soil-analogous particulate surfaces. Truong et al. [8] measured the water repellency of planar and particulate surfaces with organics, and imaged organics on a flat surface. Similarly, Kaltenbach et al. [7] both measured water repellency and performed imaging on a flat substrate. As montmorillonite clay particles are conducive to imaging, we hope to close this knowledge gap between the particulate nature of soils and the use of flat surfaces for imaging lipid adsorbates.

While the chemistry of lipids may influence SWR, surface roughness is also known to influence hydrophobicity [19–21]. The impact of surface roughness depends on its ability to trap air [19], which in turn depends on both the microscale and nanoscale surface topology [22]. *Therefore, the goal of this study is to advance a mechanistic understanding of SWR by considering both the chemistry of organic matter and the physical characteristics of model soil surfaces across length scales, with a focus on lipid-clay interactions and their role in altering such characteristics.*

Prior studies have determined that the lipid fraction of soil organic matter impacts soil hydrophobicity [23]. Lipids may be particularly important when considering seasonal cycling of SWR, as lipids have been proposed to change orientation, exposing either their hydrophilic or hydrophobic moieties, depending on environmental conditions [24]. Here we investigate a system of montmorillonite particulate films and two phospholipids with similar structures (Scheme 1) selected to allow us to distinguish the effects of melting temperature on water repellency and lipid-clay interactions. We explore the lipid-clay films from the molecular to millimeter length scales using a variety of techniques. Molecular dynamics simulations characterized the molecular-scale interaction of lipids and montmorillonite, as previously this scale has been left to speculation [12,15]. Atomic force microscopy (AFM) was utilized to observe features ranging from 1 nm to 50 μm. Fluorescence microscopy was employed to map the lipid distribution over tens to hundreds of microns. Contact angle and droplet diameter measurements at the mm scale were then used to measure the macroscopic hydrophobicity, as well as rates of droplet spreading and penetration.

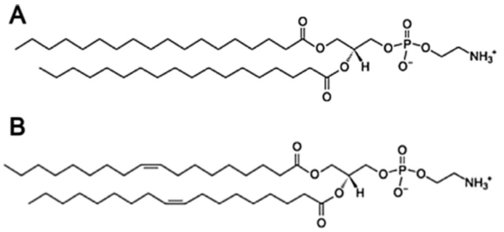

Scheme 1. Molecular structures of (A) DSPE and (B) DOPE; due to the double bonds in the tail, DOPE's melting temperature (−17 °C) is lower than that of DSPE (74 °C). Structures obtained from Avanti Polar Lipids.

Image analysis of both the AFM and fluorescence data was used to extract statistically sound measures of the characteristic features of the lipid films, including topography and lipid distribution. The mechanistic impact of these features on SWR was determined through quantitative correlations with the physical parameters that characterize the rates of droplet spreading and infiltration. We combined these methods to develop a quantitative picture of water repellency and its temporal dynamics to understand its severity and persistence over time [25] due to adaptive wetting processes that alter surface hydrophobicity [26].

2. Materials and methods

2.1. Materials

Montmorillonite (Na-SWy-2) of high purity obtained from the Clay Mineral Repository (Columbia, MO) was used for all experiments. The montmorillonite was size-fractioned by sedimentation. The <2 μm diameter fraction was then suspended in 5 M NaCl to saturate the clay with Na^+. Excess salt was removed by dialysis in 18 MΩ·cm deionized water [27]; this also prevented surface contamination by electrolytes. Phosphoethanolamine lipids (1,2-distearoyl-*sn-glycero*-3-phosphoethanolamine, DSPE and 1,2-dioleoyl-*sn-glycero*-3-phosphoethanolamine, DOPE) with purity >99% were purchased from Avanti Polar Lipids and stored in acid-washed vials. Phosphoethanolamine (PE) lipids were selected based on bacterial membrane compositions of 60–80 mol% phosphatidylethanolamine [28], which is common for gram-negative bacteria [29]. While 16-chain lipids may be more abundant for some bacteria [28], 18-chain lipids were chosen for this paper for ease of imaging. Even-numbered chain lengths were selected based on data from Ma'shum et al. [12], where even-numbered lipids were found to be predominant in soils. Lipids were selected for comparison of head group and tail group chemistry (Scheme 1). DOPE and DSPE have the same head group (phosphoethanolamine), but different tail chemistry (DOPE has one unsaturated bond per tail and DSPE is entirely saturated) and therefore different melting temperatures (−17 °C and 74 °C respectively).

2.2. Calculations

The area per PE-molecule was estimated at 60 Å^2, based on Feller [30] and Lewis and Engelman [31]. The montmorillonite surface area is known to be 22.7 m^2/g [32]; this excludes the interlayer area because the montmorillonite used was in the form of small flakes that were only one unit cell thick. The lipid concentration in an aqueous montmorillonite suspension was thus evaluated as:

$$\%CAM = \frac{Total\ area\ of\ lipid\ based\ on\ area\ per\ molecule}{Surface\ area\ of\ montmorillonite}$$

where %CAM is % Coverage as a Monolayer. While this calculation indicates the theoretical surface coverage of the lipid, it is not a statement of the actual coverage.

2.3. Sample preparation

For all imaging and contact angle experiments, samples were prepared with the same method, using techniques and materials that ensured purity and eliminated the effects of surface contamination. First, lipids dissolved in 99.8% pure chloroform (Avantor) were dried in a test tube, initially with nitrogen and then by vacuum for a minimum of 30 min. Afterwards, the lipids were solubilized in 18 MΩ·cm deionized water by gentle hydration (see SI 1.1). Lipids were added to test tubes with montmorillonite suspensions in water. The lipid/montmorillonite mixtures were vortexed for 5–10 s in order to thoroughly mix them. These mixtures were pipetted onto freshly cleaved mica surfaces and allowed to air-dry overnight in an enclosed, dark environment.

Montmorillonite suspensions of 1 mg/mL were used for AFM imaging at length scales under 5 μm. 16 mg/mL suspensions were used for fluorescence imaging, AFM imaging over 5 μm, and contact angle experiments to ensure continuous coverage of the mica plates over the length scale of the measurement.

For experiments with liquid-phase DSPE, the DSPE solution and montmorillonite suspension were both heated above DSPE's melting temperature of 74 °C, mixed above the melting temperature, dried above the melting temperature, and then imaged or measured at room temperature. These samples will be referred to as "heated DSPE" to distinguish them from the samples prepared with DSPE at room temperature.

Stearic acid/montmorillonite films were prepared by dissolving stearic acid powder (Sigma-Aldrich, 98.5% purity) in a chloroform solution. This solution was then added to an aqueous suspension of montmorillonite. While an aqueous suspension of clay is a reasonable proxy for natural soils, use of an organic solvent was necessary due to stearic acid's insolubility in water.

2.4. Atomic force microscopy

Tapping mode with AC240TS-R3 cantilevers was used for all imaging. AFM images with maximum dimensions of 5 μm were collected in air on an Asylum Cypher ES. AFM images 50 μm across were collected in air on a Bruker Dimension Icon. Images were processed in Gwyddion [33]. Additional details are available in SI 1.2.

2.5. Contact angle and droplet diameter

The contact angle of water was measured on lipid/montmorillonite films using a Kruss Drop Shape Analyzer 100 (Kruss GmbH, Hamburg, Germany). A water droplet size of 2 μL was used for all measurements per Shang et al. [34]; some variation in the volume deposited was typical for the instrument. Prior to measurement, samples were incubated at 43% humidity using solutions of saturated potassium carbonate. Static or initial contact angles were collected 0 s after deposition. The decay of contact angle over time was then monitored for 70 s. We collected five or more droplets per sample, except for heated DSPE, where only three droplets could be collected, due to the difficulty of drying the film evenly at high temperature. The contact angle and droplet dimensions (height and radius) were determined with a custom MATLAB script.

2.6. Fluorescence

Samples were prepared identically to those prepared for contact angle measurements, except that 1 mol % Rhodamine-DMPE dye was added to the lipids in chloroform. Images were taken on a Nikon Y-FL epifluorescence microscope and processed in ImageJ [35]. Rhodamine-DMPE fluoresces at 524 nm, while montmorillonite does not, so the micrographs depict the distribution of lipid within a continuous montmorillonite/lipid film.

2.7. Simulations

The clay model was based on the pyrophyllite unit cell structure, and all simulations contained a total of 96 unit cells. Four unit cells within the simulation had a cell formula $(Si_{31}Al)(Al_{14}Mg_2)O_{80}(OH)_{16}{\cdot}nH_2O$, as proposed by Cygan and coworkers [36]. We employed the CLAYFF force field, which consists of nonbonded (electrostatic and van der Waals) terms and accurately represents the local charge inhomogeneities formed around each specific substituted site in the clay. The charge neutral lipids were modeled by the CHARMM36 [37] forcefield and water was modeled using the TIP3P [38] forcefield at the desired temperatures. In each simulation box, the resulting net charge was balanced by adding interlayer Na+ ions, forming Na-Swy-2 montmorillonite.

The shapes of lipid aggregates were inferred from density profiles generated by the *gmx* density tool of gromacs. Binding energies were calculated using Replica Exchange Umbrella Sampling [39]. Convergence of these profiles was monitored as reported previously [40]. We biased the distance between the center of mass of all lipids and the clay surface using a harmonic potential of 500 (kJ/-mol)/nm^2, and exchange attempts were made every 2 ps between 28 replicas. The results of 28 biased replicas, each performed with a different distance from the clay surface, were combined using the weighted histogram analysis method (WHAM) [41]. Statistical uncertainties were estimated using the bootstrapping technique implemented in *g_wham* [42]. Additional detail is available in SI 1.3.

2.8. Image analysis

ImageJ plugins *Analyze Particle*, *Analyze Skeleton* [43,44], and *Tilted Rectangle* [45] were used to extract quantitative data from the AFM and fluorescence data. *Analyze Skeleton* was applied at three binary thresholds to capture varying levels of detail in fluorescence and large AFM images (Fig. 1). From the skeletonized data, two main parameters were extracted: junction density and inverse ridge separation. *Junction density* is the number of pixels where lines in the skeletonized image meet, averaged to the number of junctions per square micron. Junction density indicates the connectivity of the ridges in the AFM images, or of the lipid distribution in the fluorescence images. *Inverse ridge separation* is the fraction of black pixels in the image. The fraction of black pixels is proportional to the number of ridges (the brightest shapes in the original image). If there are fewer ridges in the image, the ridges are, on average, further apart. So, the fraction of black pixels is inversely proportional to the spacing between ridges; a small fraction of black pixels corresponds to a large ridge separation, and a large fraction corresponds to small ridge separation. Note that while we have chosen to interpret the fraction of black pixels as a measure of ridge separation, it is most directly a measure of how many ridges are above a certain elevation or brightness in the images. See also Fig. 4 and SI 1.4.

3. Results and discussion

3.1. Wettability

As measured by the static contact angle, neither DOPE nor DSPE significantly altered the water repellency of montmorillonite at the

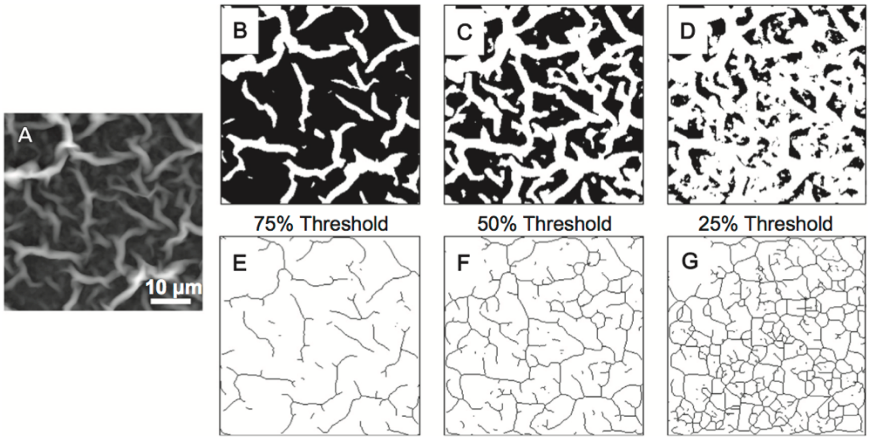

Fig. 1. Fluorescence and large AFM images (see also Fig. 4) were binarized at three different thresholds to capture all details. (A) An example of montmorillonite film topography, in grayscale, measured by AFM. (B) Image A binarized at the 75% threshold. A 75% threshold indicates that the bottom 75% of the image (by elevation) are darkened, leaving only the top 25% light. (C) At the 50% threshold, the top half of the image is light, and the bottom half is dark. (D) In the 25% threshold, only the bottom quarter of the image's elevation is darkened. The top 75% is light. (E–G) Once binarized, the images were skeletonized, wherein each white branch in B–D is reduced to a single-pixel-wide line running through the center of the binarized white branch. (E) At the 75% threshold, there are only a few ridges; only the tallest ridges are captured. (F) The 50% threshold captures the tallest ridges as well as some intermediately tall ridges. (G) Nearly all ridges are captured by the 25% threshold. The fraction of black/total pixels in the image is taken as the inverse separation between ridges; fewer black pixels correlates to a wider separation between ridges. See also SI figures S1 and S2.

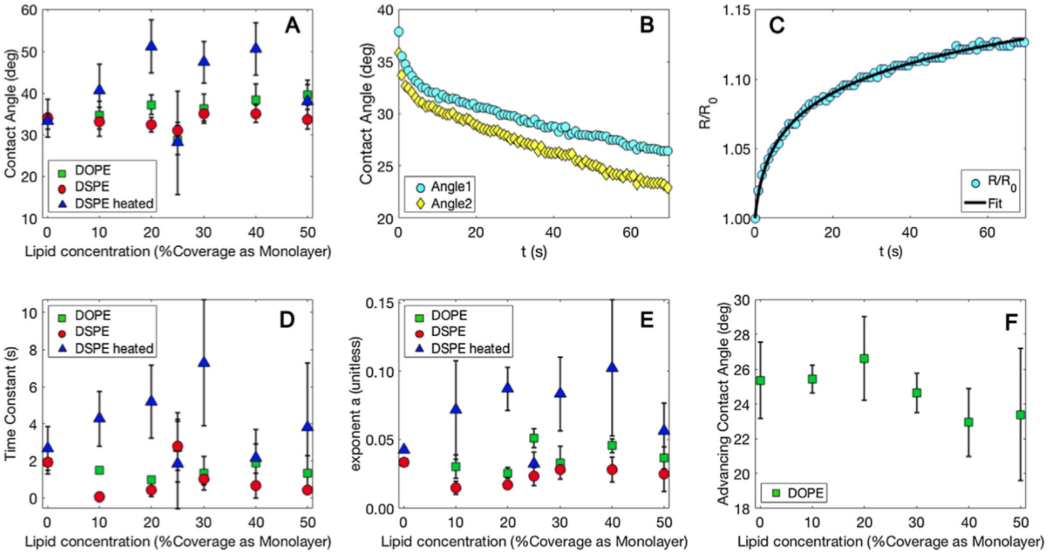

Fig. 2. (A) Initial contact angle vs lipid concentration for DOPE, DSPE, and heated DSPE. (B) Typical example of the dependence of contact angle on time, here for a montmorillonite film. Angle1 and Angle2 respectively mark the left and right side of the droplet. (C) Typical example of the dependence of droplet radius on time fit with Equation 3 for droplet spreading across a porous surface. (D) Time constant (1/K) for water droplets spreading across and soaking into lipid/montmorillonite films vs lipid concentrations for DOPE, DSPE and heated DSPE. (E) Exponent *a* of water droplets spreading across and soaking into lipid/montmorillonite films vs lipid concentration for DOPE, DSPE and heated DSPE. (F) Advancing contact angle vs lipid concentration for DOPE/montmorillonite films. All error bars represent standard deviations, and in some cases are smaller than the data point markers. Note that the larger error bars seen for heated DSPE in panels D and E arise from the small number of droplets used for the analysis owing to difficulty drying heated montmorillonite into an even film.

concentrations tested. However, heated DSPE did cause a moderate rise in contact angle at intermediate coverages (Fig. 2A). These findings contrast with trends seen in prior work comparing saturated and unsaturated fatty acids, where adding small amounts of polar organic molecules, such as stearic acid, induced significant water repellency [15] on quartz sand. These previous studies reported large increases in contact angle and indicated that the maximum water resistance occurred at 16 monolayer equivalents of stearic acid [12,13]. Our results show no such effect for phospholipids on montmorillonite.

To determine if stearic acid could induce the same effect on montmorillonite, stearic acid/montmorillonite films were prepared. Addition of up to one monolayer equivalent stearic acid (dissolved in chloroform) did not alter the contact angle. At 16 monolayer equivalents, only one of five droplets placed on the film exhibited a significantly higher contact angle (Fig. 3A), and that contact angle rapidly decayed over time. These results indicate that montmorillonite remains wettable even with a considerable concentration of polar amphiphilic molecules, and may provide a rationale for why adding clay to a sandy soil can reduce its water repellency.

Despite the relatively minor effects of lipids on the static contact angle, significant insights on wettability can be obtained through a more comprehensive analysis of the data. Static contact angle is merely the contact angle at the initial time, t = 0. This initial contact angle tells only a partial story of wettability, namely its *severity*. With time, the contact angle decays and the droplet spreads, because penetration of the droplet into the film reduces the static contact angle of water on the film. Thus, the droplet penetration time (see also the water droplet penetration time test, WDPT [2]) provides additional information on the temporal *persistence* of water repellency. As Fig. 2B and C show, the contact angle decreased continuously with time as the droplet's radius increased during its lateral spread across the surface.

The above behavior can be understood and analyzed to extract the key characteristics by considering the deposition of a droplet onto a porous film [46,47]. The initial contact angle reflects the static contact angle for the dry film. Subsequently, the droplet infiltrates the film and spreads laterally. Changes in the measured contact angle during this process depend on (1) film hydration, which alters the interfacial energy, and (2) the extent to which the droplet is able to respond to that change either by expanding or contracting. If the contact line is pinned, the droplet diameter will remain fixed, as will the measured contact angle as long as the amount of infiltration into the film is much smaller than the volume of the droplet. If the contact line is free to move, and the static contact angle decreases upon infiltration, the droplet diameter will increase as long as the measured contact angle exceeds the static advancing contact angle.

Our observations show that upon placement on the dry film, the diameter of the drop immediately began increasing, and the contact angle decreased accordingly. As shown in Fig. 2C, the droplet radius eventually reached a maximum value R_{max}, after which it was roughly constant. (If the droplet were monitored for a longer amount of time, eventually the droplet must begin to shrink as the amount of water infiltrating into the film becomes significant relative to the volume of the droplet.) This behavior is expected for a droplet of initial volume V_0 and radius R_0 spreading across a thin porous film that exhibits partial wetting by the droplet [46] (see Fig. S3 and SI S.2 for additional details, and references [46] and [47] for a complete mathematical model). While the radius expands, the dependence of the droplet's radius on time is expected to follow [47]:

$$\frac{R}{R_0} = [1 + Kt]^a \qquad (1)$$

where R_0 is the value of R at t = 0, *K* is an inverse time constant that depends on many physical parameters of the film and the fluid, and *a* is a constant that depends on the value of the fluid behavior index *n*. (The fluid index measures the extent to which a fluid's viscosity changes under strain.) The parameters *K* and *a* were determined by fitting R/R_0 vs. time with Eq. (1) for each droplet.

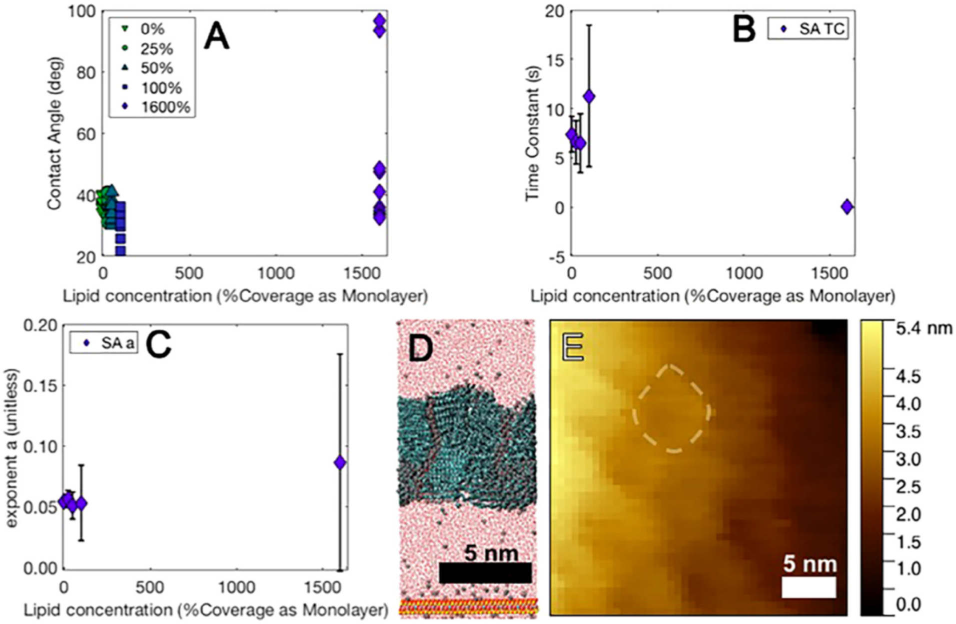

Fig. 3. (A–C) Dependence on stearic acid concentration of: (A) initial contact angle, (B) time constant and (C) exponent *a* for water droplets spreading across and soaking into stearic acid/montmorillonite films. Error bars represent one standard deviation. (D) Simulation results showing that stearic acid does not interact with montmorillonite in solution, but instead forms floating, interlocked crystals, where crystal boundaries are seen as roughly vertical discontinuities. (E) AFM image of a stearic acid/montmorillonite film at 1600% coverage showing crystallites (e.g., white outline) similar in size to lipid crystals seen in (D).

The meaning of *a* and of *K* is dependent upon whether the rate limiting process is the outward wicking of fluid through the film (imbibition) or the flow of liquid across the surface (spreading). Because the dry film has a larger static contact angle than the saturated film, the droplet cannot spread beyond the limit of the saturated zone. Thus, for films with poor permeability the droplet spreading rate is constrained by the rate of imbibition. In this imbibition-limited case, *K* represents the characteristic rate constant for that process and $a = n/(1 + n)$ [46]. In contrast, for highly permeable films the imbibition front stays ahead of the contact line of the droplet, and the rate of spreading across the surface is the limiting process. *K* then represents the characteristic rate constant for droplet spreading across the film's surface with $a = n/(3n + 7)$ [47]. Additionally, the time dependence of R/R_0 can be used to determine the static advancing contact angle, θ_{adv}, which occurs at R_{max} (Fig. 2F, SI Table S1).

A number of considerations indicate the rate of imbibition through the film is more rapid than the rate of spreading across the surface. This conclusion is supported by the observation that the volume remains essentially constant (<10% loss) out to R_{max} (Fig. S3D). If significant imbibition were to occur, then the volume would begin to decrease before the static advancing contact angle was achieved.

Additional information suggesting that imbibition is the limiting process was gathered from the parameter *a*. For our data, *a* generally lies between 0.02 and 0.1 (Fig. 2E). As discussed above, if we assume the measured value of *a* is determined by droplet spreading, then $a = n/(3n + 7)$ leads to $0.15 < n < 1$. A value of $n < 1$ implies the droplet is non-Newtonian and exhibits shear-thinning, as is expected, for example, for water-surfactant mixtures [48] or for water confined within clay layers [49]. However, neither scenario is expected for a water droplet spreading across the surface of the film, as very little lipid is present on the film surface relative to the size of the droplet and there is no confinement of the water. Thus, observed values of $n < 1$, indicating shear-thinning behavior or confinement, renders the scenario of droplet expansion limited by spreading across the surface highly unlikely. On the other hand, the mineral film is a mixture of montmorillonite particles and lipid; thus the dynamics of infiltration of water *through* the film could very well reflect a water-surfactant mixture, as well as the effects of confinement. Taking imbibition as the controlling process, $a = n/(1 + n)$, leading to $0.02 < n < 0.1$, which is consistent with a water-surfactant mixture and/or confined water within the film. *Therefore,* n *values indicative of shear-thinning are consistent with the imbibition-limited picture of film wetting.* While this data set does not provide any information on the influence of Cassie-Baxter or Wenzel wetting states on *n*, it is likely that the presence of a particular wetting state also alters *n*, *a*, and *K*.

3.2. Film topography and lipid distribution

While lipids might be expected to alter the characteristics of wetting through the direct chemical modification of water-film interactions, the effects could also be secondary due to impact of the lipids on film morphology. To understand whether changes in wettability seen upon addition of lipid were directly related to water interacting with the lipids or were a result of morphological changes, we quantified the morphological characteristics of the film, the lipids, and the effect of the latter on the former.

3.2.1. Film topography

The AFM data showed that aqueous montmorillonite suspensions dried into wrinkled films (Fig. 4A), with very similar results found for lipid/montmorillonite films. Fluorescence microscopy performed on montmorillonite/DOPE films revealed a similar pattern of ridges and junctions. Comparison of quantitative measures of film morphology (see Section 2.8 and Fig. 1), such as junction density and ridge length, show no difference between montmorillonite films and montmorillonite/lipid films at the 95% confidence level. Fluorescence microscopy showed that both DOPE and heated DSPE were distributed throughout the network of ridges on the surface, as well as in form of many small, bright spots within the network (Fig. 4B and D), while DSPE appeared only sporadically as large discrete patches for all investigated coverages (Fig. 4C).

3.2.2. Lipid morphology

When imaged at the sub-micron scale, the edges of individual montmorillonite flakes are easily identified and appear smooth (Fig. 5A). At this scale, the lipids display a range of morphologies (Fig. 5B–F). Small lipid aggregates, circular in cross-section, are

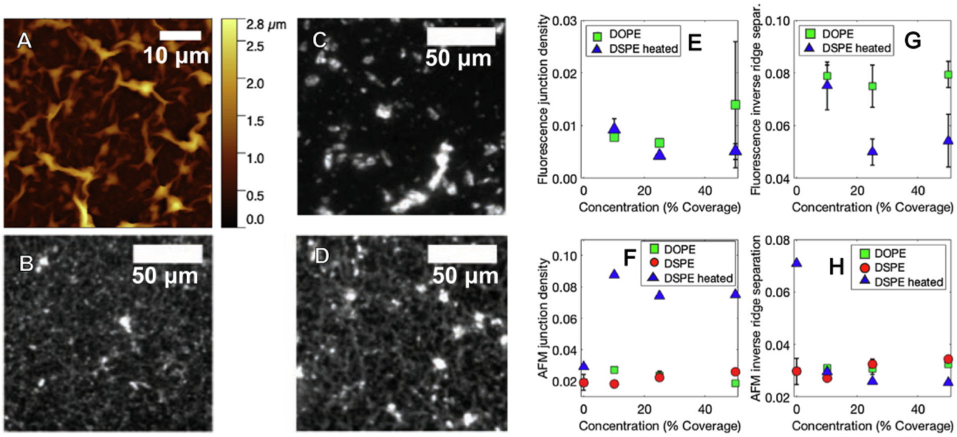

Fig. 4. Film texture and lipid distribution. (A) AFM image showing topography of a dried montmorillonite film. Ridges have a maximum height of <3 μm over a 50 × 50 μm² area. Montmorillonite/lipid films were similar in appearance. (B–D) Lipid distributions within montmorillonite/lipid films, seen by fluorescence microscopy for (B) DOPE, (C) DOPE and (D) heated DSPE. (E–H): Film topography variables across different concentrations of lipid, all at the 75% binary threshold. (E) Fluorescence junction density. (F) AFM inverse ridge separation. (G) Inverse ridge separation from fluorescence. (H) AFM junction density. Error bars represent one standard deviation.

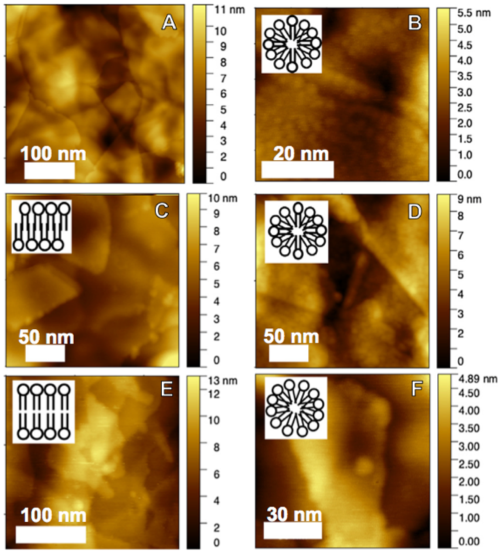

Fig. 5. Lipid morphology on the surface as determined by AFM and MD. Insets: cartoons of aggregate structure seen in MD (see Fig. 6). (A) Montmorillonite alone has crisp edges and smooth basal planes. (B) DOPE, 25% coverage. Micellar structure. (C) DSPE, 25% coverage. Interdigitated bilayer structure. (D) DOPE, 50% coverage. Micellar structure. (E) DSPE, 50% coverage. Bilayer structure. (F) Heated DSPE, 25% coverage. Micellar structure.

the dominant feature on montmorillonite. Based on the shape and height of the aggregates, we hypothesize that they begin as micelles when in a hydrated environment. For DSPE, about 85% of the aggregates occur on flake edges (Fig. 5C, SI Table S2). For DOPE, only 10–25% occur at edges; the rest are on montmorillonite basal surfaces (Fig. 5B). At 50% coverage, DSPE forms irregular bilayer films instead of small aggregates (Fig. 5E).

For morphologies with discrete aggregates, the surface density and the fraction present on edges were quantified, as these features could alter the porosity and accessibility of montmorillonite surfaces to water. The percent of aggregates on edges ranged from about 10% to 100%. Most samples had an aggregate density of less than one aggregate per square micron, but the density range extended to 100 times that value.

MD simulations suggest the structure of the aggregates ranges from micelles to patches of bilayer (Fig. 5 insets, Fig. 6) and that the distinct surface-bound aggregates first spontaneously form from individual lipid molecules before binding to the surface. The density of the lipid moieties can be used to infer the shape of surface-bound aggregates [50]. Density profiles of the nitrogen atoms in the lipid headgroup are asymmetric, showing there are more lipids that are bound to the surface than lipids that are not.

For DOPE, the nitrogen density at both 25% and 50% coverage falls drastically with distance, but does not completely vanish (Fig. 6D), becoming constant beyond 1 nm. The carbon peak for both aggregates is unimodal, suggesting the formation of a spherical micelle in both cases. For DSPE (Fig. 6E), however, both nitrogen and carbon profiles at 25% coverage exhibit bimodal distributions with negligible density in-between. For 50% DSPE, the nitrogen profile is bimodal, but that of carbon is unimodal. These distinct profiles correspond to interdigitated lipid bilayer arrangements and regular bilayer arrangement for 25% and 50% DSPE, respectively. In the heated state, DSPE at 25% behaves similarly to DOPE and forms a spherical micelle, but at 50% but the bimodal nature of the nitrogen density profile, which does not vanish between the peaks, implies formation of a cylindrical micelle (Fig. 6F). In all cases, the aggregates bind to the surface via the lipid headgroup, and the lipids arrange themselves in such a way that the tail groups are protected from exposure to water.

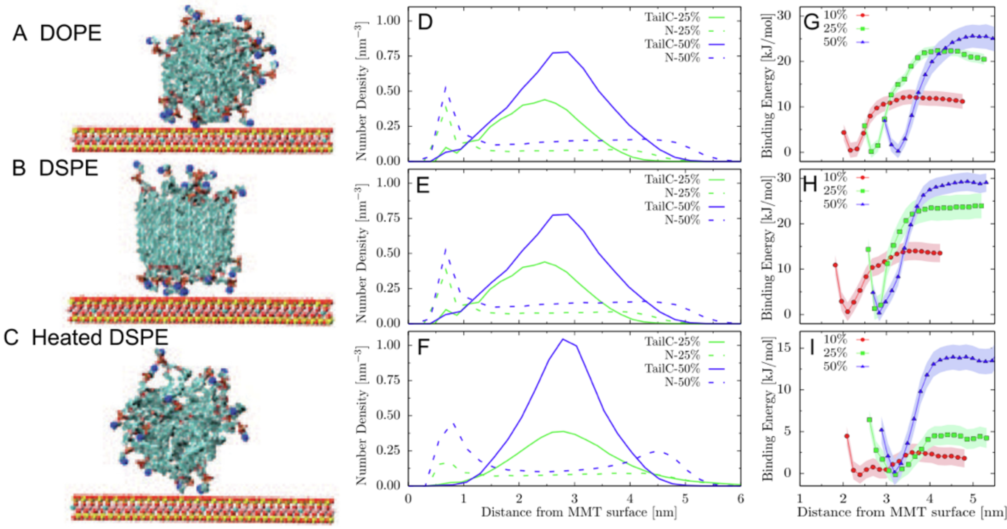

Fig. 6. Results from MD simulations. Representative simulation snapshots are shown in panel A, B, and C where lipid nitrogen is represented in blue, lipid phosphorous is represented in orange and oxygen in red. The clay oxygen, silicon, aluminum and magnesium are represented in red, yellow, pink and cyan respectively. The ions and water molecules in the simulation are not shown for clarity. Density plots for the aggregates are presented in D–F: DOPE (D), DSPE (E) and heated DSPE (F). The free energy of lipid aggregate binding to the surface of the montmorillonite is favorable for DOPE (G), DSPE (H), and heated DSPE (I).

Our results show that the binding becomes more favorable with increasing lipid concentration in all three lipids (Fig. 6G–I). The magnitude of the binding energy ranges from 10 kJ/mol to 30 kJ/mol for lipids at room temperature; these values decrease to a range of 2–12 kJ/mol for heated DSPE. The decrease in free energy for binding of heated DSPE is much lower than for DOPE and DSPE at room temperature.

3.2.3. Impact of lipid phase on lipid distribution and film morphology

The fluorescence microscopy data, such as those in Fig. 4, show that the liquidity of the lipid influences its distribution in the film. To determine if lipid distributions are correlated with film structure, those distributions were compared to the parameters characterizing the network of ridges and valleys seen in both AFM and fluorescence images. In the case of DOPE and heated DSPE, the ridge networks observed by fluorescence appear to match the topography seen by AFM (Fig. 4A vs B and D). Comparison shows that the ridge separation of DOPE as seen in fluorescence at 26% and 50% coverage does not differ statistically from the AFM topography of a montmorillonite film prepared at the same lipid concentration at the 95% confidence level, with the 75% binary threshold of fluorescence data most closely matching the 25% binary threshold of AFM data (SI Table S3). Thus, DOPE molecules are evenly distributed through the montmorillonite film at this scale, appearing brighter where the montmorillonite flakes stack into ridges.

Unlike DOPE and heated DSPE, the location of room temperature DSPE is not evident when comparing the AFM and fluorescence images. However, the shape and distribution of DSPE as seen by fluorescence is similar to the low-topography areas — i.e., the valleys — in the 50 μm AFM data. To quantitatively test if this correlation arises because DSPE is predominantly present in the valleys (Fig. 4A and C), the area and shape (as indicated by circularity, Feret diameter, and Feret minimum diameter) of DSPE patches and the film valleys were analyzed. With the exception of circularity, this analysis shows that DSPE patches are statistically the same size and shape as the valleys (SI Table S4). Given DSPE's high melting temperature of 74 °C, its immobility at room temperature may be responsible for its location within these valleys.

Table 1
Wettability and physical variables compared via linear regression. The regression was calculated with the film characteristics plotted on the x-axis and the wettability parameter on the y-axis. The variables were measured for multiple concentrations of lipid, such that three to six data points were used for each regression. See also Fig. 7.

Wettability parameters	Film characteristics (in final, room-temperature dry state)
Contact angle at t = 0	Ridge separation
Rate Constant *K*	Junction density
Exponent *a*	Aggregate density
	Fraction of aggregates on edge of flakes

The topography of the DOPE and DSPE films was generally similar, with the two lipids showing the same trends of ridge spacing and junction density for the concentrations used here (Fig. 4E–H). Heated DSPE, however, tends to follow different trends and has a different ridge spacing/junction density. There are two conclusions that follow from this observation. (1) DOPE and DSPE have similar effects on film topography, in spite of their drastically different distribution through the film and different physical states. (2) DOPE and heated DSPE have the same distribution in the film, but different film topography. Therefore, the physical state of the lipid – liquid or solid, respectively – matters considerably *if the lipid distribution is the same.*

3.3. Relationship between wettability and physical film parameters

The results presented above (Fig. 2A) show that the static contact angles for both DOPE and DSPE, within error, have little or no dependence on the lipid coverage for the range of coverages explored here, although there is a measurable trend for heated DSPE. Moreover, the rate at which the radius increases and the contact angle decays from its initial value exhibits a similar trend for these two lipids. To determine whether the physical film characteristics correlate with the wetting characteristics, we ran linear regressions comparing each wettability parameter to each physical characteristic. For example, the rate constant *K* is compared to the ridge separation for each lipid, then compared to the junction density, and so on until all possible pairs have been compared (Table 1).

The results (Figs. 7, S4, S5, and Table 2), show that several lipid-film characteristics exhibit significant correlations with the contact angle, *a*, or *K*. Parameters characterizing lipid morphology — the aggregate density and the fraction of aggregates on edges — only exhibit one significant correlation with the wettability: the fraction of DSPE aggregates on edges correlates with the initial contact angle. In contrast, parameters characterizing the film topography exhibit multiple correlations with the wettability. For heated DSPE the parameter *a* consistently correlates with ridge separation and junction density, occurring in the fluorescence data. However, for solid phase DSPE, this correlation is reflected in AFM data. For DOPE, the rate constant *K* and initial contact angle depend on the ridge separation measured by fluorescence and AFM imaging, and *a* correlates with ridge separation in fluorescence. (See the supplement for a complete breakdown of correlations.)

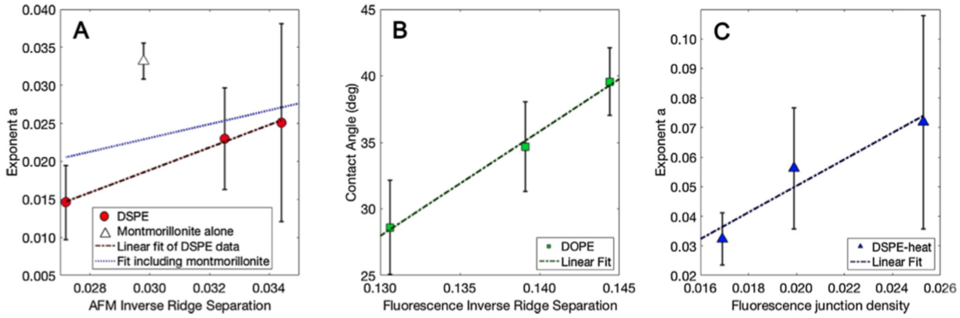

Fig. 7. Example correlations with $r^2 > 0.8$ between wettability parameters and physical characteristics. (A) DSPE: Junction density from AFM images of the film and exponent *a*, with and without including the pure montmorillonite data point. All data is from the 75% binary threshold. (B) DOPE: Fluorescence inverse ridge separation and initial contact angle. (C) Heated DSPE: Fluorescence junction density and exponent *a*. Error bars represent one standard deviation.

Table 2
Correlations for which $r^2 > 0.8$ are marked with X and shaded darker/purple. Weaker correlations are shaded lighter/more yellow. Wetting variables are labeled across the top, and physical variables down the side. Data points for montmorillonite alone are not used in the regressions. See Figs. 1 and 5 for physical variable visual references. Complete r^2 information is available in the SI.

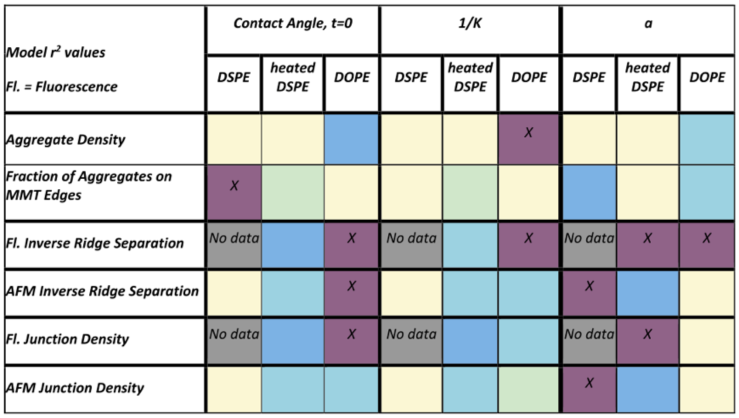

Model r^2 values *Fl. = Fluorescence*	*Contact Angle, t=0*			*1/K*			*a*		
	DSPE	*heated DSPE*	*DOPE*	*DSPE*	*heated DSPE*	*DOPE*	*DSPE*	*heated DSPE*	*DOPE*
Aggregate Density						X			
Fraction of Aggregates on MMT Edges	X								
Fl. Inverse Ridge Separation	No data		X	No data		X	No data	X	X
AFM Inverse Ridge Separation			X				X		
Fl. Junction Density	No data		X	No data			No data	X	
AFM Junction Density							X		

To interpret these results, it is important to distinguish between ridge separation as measured by AFM and as measured by fluorescence. The AFM images show all ridges regardless of how much lipid is present, whereas fluorescence only shows ridges with enough lipid to produce a fluorescence signal. So, a dependence of K or a on ridge separation seen in fluorescence for DOPE and heated DSPE is equivalent to a dependence on the lipid distribution in the film. On the other hand, because DSPE is present only as dispersed solid patches, the fluorescence does not provide any information on ridges. Thus, for DSPE, only correlations with AFM topography can be examined and any attempts to correlate the values of K or a on DSPE distribution must be based on assumptions about that distribution.

The differences in correlations for the three lipids indicate influence from both the lipid chemistry and physical state (Table 3). In fact, each of the three lipids is unique: DOPE is liquid and distributed uniformly through the film; DSPE is solid and present in discrete patches; heated DSPE is solid and distributed uniformly through the film. These differences appear in the value of the parameter a, which, as discussed above, can be used to calculate the fluid index of water imbibing into the clay and indicates the deviation of fluid behavior from Newtonian (Table 3). The data presented here show that even water penetrating a plain montmorillonite film behaves as a shear-thinning fluid, consistent with the work of others [49], but comparison of a for pure montmorillonite films with that for lipid-containing films shows that addition of lipid further alters the fluid index of water. Most notably, heated DSPE actually increased the fluid index, making water behave more like a Newtonian fluid than in the pure montmorillonite film. In contrast, DSPE and DOPE reduced the fluid index further, increasing the degree of shear-thinning of the water in the film (Table 3). The importance of the lipids on fluid behavior is additionally demonstrated by the correlations between a and either the ridge separation or the junction density, because the data points for pure montmorillonite films fall significantly off the trends seen with lipids (for example, Fig. 7A).

Examination of the correlations between the ridge separation and a and K suggest underlying physical reasons for the trends. For DOPE, a increases and K decreases with increasing ridge separation as measured by fluorescence. Larger ridge separation in fluorescence indicates less overall DOPE in the film, giving less water-lipid interaction and thus more Newtonian behavior (i.e., less shear thinning) and slower permeation.

In contrast to DOPE, for heated DSPE, a and K both decrease with ridge separation as measured by fluorescence. However, since DSPE is solid at room temperature where the droplet spreading

Table 3
Summary of how water behaves during infiltration of a montmorillonite/lipid film. Lipid state and distribution within the film alter water to be more or less Newtonian. More Newtonian water permeates the film more slowly than water with a high degree of shear thinning. Note that a Newtonian fluid has $a = 0.5$ in an imbibition-limited scenario. Also see Fig. 3D and E.

Water behavior with certain lipid conditions at *room temperature*	**Liquid lipid (DOPE)**	**Solid lipid (DSPE, heated DSPE)**
Even distribution in film	Maximum shear thinning, ($a \sim 0.03$)	Minimum shear thinning ($a \sim 0.07$)
Discrete distribution in film	No data	Maximum shear thinning, ($a \sim 0.03$)

characteristics are measured, despite its incorporation into the film in the heated (liquid) state, less lipid will be solubilized into the infiltrating water droplet than with DOPE. Moreover, because organic molecules sandwiched by clay flakes increase the d-spacing between flakes [51], heated DSPE, being a solid evenly distributed throughout the film, should increase the pore space. Thus, the infiltrating droplet should have less solubilized lipid and be less confined. As a result the droplet will further trend toward Newtonian behavior and infiltrate more quickly compared to the unheated lipids.

For solid DSPE, a decreased with increasing ridge separation as measured by AFM, but K shows no significant correlations with topographic features. Assuming DSPE is deposited only in the valleys (based on the fluorescence maps), a small ridge separation may mean *less* contact between water and the lipid, as the water would have to push into the valley in order to interact with DSPE. Thus, again, less lipid-water interaction leads to a smaller deviation from Newtonian behavior. Moreover, because DSPE exists only as discrete patches, its distribution has negligible impact on the rate of infiltration.

4. Conclusions

The findings presented above have a number of implications. First, the simple measurement of an initial contact angle is of limited utility in assessing soil–water interaction (Fig. 2B). The behavior of a droplet on a film of soil particles is dynamic and it is the characteristics of those dynamics that provide a quantitative measure of repellency. These characteristics include the rate constant K for infiltration and the fluid index parameter a (Fig. 2D and E), which provide physical insight into changes in a film's wettability (Tables 2 and 3).

Measurements as a function of lipid concentration in montmorillonite films show that phospholipids produce little or no increase in initial contact angle θ_i, with the change ranging from too small to measure for DSPE added at room temperature to as much as 18° for heated DSPE (Fig. 2A). Changes in K and a are also greatest for heated DSPE; both initially increase significantly with added lipid before falling off at higher concentrations. DOPE and DSPE show smaller initial decreases in K and a before rising back to initial values (Fig. 2E and F). These findings contrast with measurements performed on quartz substrates and quartz sands mixed with fatty acids [13], which exhibit large increases in θ_i (see Fig. 3). Thus, our findings provide a rationale for the common practice of mixing clays into sandy soils to reduce water repellency [17,18].

Film texture and lipid tail chemistry are the key features controlling wettability of a lipid/montmorillonite film. θ_i on the dry film, K, and a are all correlated with characteristics of film texture and/or lipid distribution including the average separation between ridges and junctions and, to a lesser extent, the density of lipid aggregates (Table 2). Overall, water behaves as a shear-thinning fluid when wetting the film (Fig. 2E), likely due to dissolution of lipid into the water and impacts on the pore size in the film. These factors are impacted by the lipid melting point; in the liquid state, lipid is evenly distributed throughout the film while solid lipid is not (Fig. 4). This difference in lipid distribution may offer insight into why water repellency has such drastic spatial variability within a single field site [9].

The measurements and simulations reported here focus on effects of lipid coverage and melting point on the water repellency of a montmorillonite film. The impact of head-group chemistry, as well as mixtures of compounds and multiple minerals, deserve further attention. Mixtures of compounds have been previously found to alter water repellency differently than individual compounds [8,15], and are more analogous to real soils. Consequently, quantifying the effect of mixing of compounds on water repellency should provide a bridge between the simple model system explored here and the far more complex scenario presented by real soils.

CRediT authorship contribution statement

Brenda L. Kessenich: Conceptualization, Formal analysis, Investigation, Methodology, Visualization, Writing - review & editing, Writing - original draft. **Nihit Pokhrel:** Formal analysis, Investigation, Methodology, Visualization, Writing - original draft. **Elias Nakouzi:** Formal analysis, Methodology, Resources, Writing - review & editing. **Christina J. Newcomb:** Conceptualization, Supervision, Writing - review & editing. **Markus Flury:** Resources, Writing - review & editing. **Lutz Maibaum:** Methodology, Supervision, Writing - review & editing. **James J. De Yoreo:** Conceptualization, Methodology, Supervision, Writing - original draft, Writing - review & editing.

Acknowledgments

We thank B. A. Legg for assistance with data analysis and Thomas Underwood for assistance with initial simulation set-up. Odeta Qafoku and John Loring (PNNL) provided processed montmorillonite. BLK is indebted to Prof. Sarah Keller and her group at UW for lipid expertise, wet lab space, and microscope use. BLK is supported by the National Science Foundation Graduate Research Fellowship Program under Grant No. DGE-1762114. Any opinions, findings, and conclusions or recommendations expressed in this material are those of the author(s) and do not necessarily reflect the views of the National Science Foundation. Sample synthesis, image analysis algorithms, and model development were supported by the US Department of Energy (DOE), Office of Basic Energy Sciences (BES) Chemical Sciences, Geosciences, and Biosciences Division at Pacific Northwest National Laboratory (PNNL). PNNL is a multiprogram national laboratory operated for DOE by Battelle under Contract No. DE-AC05-76RL01830. This work was facilitated though the use of advanced computational, storage, and networking infrastructure provided by the Hyak supercomputer system at the University of Washington. Atomic force microscopy was conducted at the Molecular Analysis Facility, a National Nanotechnology Coordinated Infrastructure site at the University of Washington which is supported in part by the National Science Foundation (grant NNCI-1542101), the University of Washington, the Molecular Engineering & Sciences Institute, the Clean Energy Institute, and the National Institutes of Health.

Appendix A. Supplementary material

Supplementary data to this article can be found online at https://doi.org/10.1016/j.jcis.2019.07.075.

References

[1] J. Lehmann, M. Kleber, The contentious nature of soil organic matter, Nature 528 (2015) 60–68.
[2] P.M. King, Comparison of methods for measuring severity of water repellence of sandy soils and assessment of some factors that affect its measurement, Austral. J. Soil Res. 19 (1981) 275.
[3] J.P. Terry, R.A. Shakesby, Soil hydrophobicity effects on rainsplash: Simulated rainfall and photographic evidence, Earth Surf. Process. Landforms 18 (1993) 519–525.
[4] J.F. Osborn, R.E. Pelishek, J.S. Krammes, J. Letey, Soil wettability as a factor in erodibility, Soil Sci. Soc. Am. J. 28 (1964) 294–295.
[5] J.V. Witter, P.D. Jungerius, M.J. ten Harkel, Modelling water erosion and the impact of water repellency, CATENA 18 (1991) 115–124.
[6] B. Marschner, K. Kalbitz, Controls of bioavailability and biodegradability of dissolved organic matter in soils, Geoderma 113 (2003) 211–235.

[7] R. Kaltenbach, D. Diehl, G.E. Schaumann, Links between nanoscale and macroscale surface properties of natural root mucilage studied by atomic force microscopy and contact angle, J. Colloid Interface Sci. 516 (2018) 446–455.

[8] V.K. Truong, E.A. Owuor, P. Murugaraj, R.J. Crawford, D.E. Mainwaring, Impact of particle nanotopology on water transport through hydrophobic soils, J. Colloid Interface Sci. 460 (2015) 61–70.

[9] K. Müller, M. Deurer, P. Jeyakumar, K. Mason, C. van den Dijssel, S. Green, B. Clothier, Temporal dynamics of soil water repellency and its impact on pasture productivity, Agric. Water Manage. 143 (2014) 82–92.

[10] L.N. Soucémarianadin, B. Erhagen, M.B. Nilsson, M.G. Öquist, P. Immerzeel, J. Schleucher, Two dimensional NMR spectroscopy for molecular characterization of soil organic matter: application to boreal soils and litter, Org. Geochem. 113 (2017) 184–195.

[11] S. Cheng, S.H. Doerr, R. Bryant, C.J. Wright, Effects of isopropanol/ammonia extraction on soil water repellency as determined by atomic force microscopy, Soil Sci. Soc. Am. J. 74 (2010) 1541–1552.

[12] M. Ma'shum, V.C. Farmer, Origin and assessment of water repellency of a sandy South Australian soil, Soil Res. 23 (1985) 623–626.

[13] D.a.L. Leelamanie, J. Karube, A. Yoshida, Characterizing water repellency indices: contact angle and water drop penetration time of hydrophobized sand, Soil Sci. Plant Nutr. 54 (2008) 179–187.

[14] L. Petridis, H. Ambaye, S. Jagadamma, S.M. Kilbey, B.S. Lokitz, V. Lauter, M.A. Mayes, Spatial arrangement of organic compounds on a model mineral surface: implications for soil organic matter stabilization, Environ. Sci. Technol. 48 (2014) 79–84.

[15] K. Mainwaring, I.L. Hallin, P. Douglas, S.H. Doerr, C.P. Morley, The role of naturally occurring organic compounds in causing soil water repellency, Eur. J. Soil Sci. 64 (2013) 667–680.

[16] J. Hassink, Preservation of plant residues in soils differing in unsaturated protective capacity, Soil Sci. Soc. Am. J. 60 (1996) 487–491.

[17] I. McKissock, E.L. Walker, R.J. Gilkes, D.J. Carter, The influence of clay type on reduction of water repellency by applied clays: a review of some West Australian work, J. Hydrol. 231 (2000) 323–332.

[18] G. McHale, M.I. Newton, N.J. Shirtcliffe, Water-repellent soil and its relationship to granularity, surface roughness and hydrophobicity: a materials science view, Eur. J. Soil Sci. 56 (2004) 445–452.

[19] A.B.D. Cassie, S. Baxter, Wettability of porous surfaces, Trans. Faraday Soc. 40 (1944) 546–551.

[20] M. Nosonovsky, B. Bhushan, Roughness optimization for biomimetic superhydrophobic surfaces, Microsyst. Technol. 11 (2005) 535–549.

[21] Y.C. Jung, B. Bhushan, Contact angle, adhesion and friction properties of micro- and nanopatterned polymers for superhydrophobicity, Nanotechnology 17 (2006) 4970.

[22] Russel J. Crawford, Elena P. Ivanova, Chapter two: Natural Superhydrophobic Surfaces, Elsevier, 2015.

[23] E. de Blas, M. Rodríguez-Alleres, G. Almendros, Speciation of lipid and humic fractions in soils under pine and eucalyptus forest in northwest Spain and its effect on water repellency, Geoderma 155 (2010) 242–248.

[24] S.H. Doerr, R.A. Shakesby, R.P.D. Walsh, Soil water repellency: its causes, characteristics and hydro-geomorphological significance, Earth-Sci. Rev. 51 (2000) 33–65.

[25] J. Letey, M.L.K. Carrillo, X.P. Pang, Approaches to characterize the degree of water repellency, J. Hydrol. 231 (2000) 61–65.

[26] H.-J. Butt, R. Berger, W. Steffen, D. Vollmer, S.A.L. Weber, Adaptive wetting—adaptation in wetting, Langmuir 34 (2018) 11292–11304.

[27] J.S. Loring, H.T. Schaef, R.V.F. Turcu, C.J. Thompson, Q.R.S. Miller, P.F. Martin, J. Hu, D.W. Hoyt, O. Qafoku, E.S. Ilton, et al., In situ molecular spectroscopic evidence for CO_2 intercalation into montmorillonite in supercritical carbon dioxide, Langmuir 28 (2012) 7125–7128.

[28] J. Gmeinfr, H.H. Martin, Phospholipid and lipopolysaccharide in proteus mirabilis and its stable protoplast l-form, Eur. J. Biochem. 67 (1976) 487–494.

[29] A.J.D. Siervo, A.D. Homola, Analysis of caulobacter crescentus lipids, J. Bacteriol. 143 (1980) 1215–1222.

[30] S.E. Feller, R.M. Venable, R.W. Pastor, Computer simulation of a DPPC phospholipid bilayer: structural changes as a function of molecular surface area, Langmuir 13 (1997) 6555–6561.

[31] B.A. Lewis, D.M. Engelman, Lipid bilayer thickness varies linearly with acyl chain length in fluid phosphatidylcholine vesicles, J. Mol. Biol. 166 (1983) 211–217.

[32] M. Dogan, A.U. Dogan, F.I. Yesilyurt, D. Alaygut, I. Buckner, D.E. Wurster, Baseline studies of the clay minerals society special clays: specific surface area by the Brunauer Emmett Teller (BET) method, Clays Clay Miner. 55 (2007) 534–541.

[33] Gwyddion, Available at http://gwyddion.net/ (accessed: 20th December 2018).

[34] J. Shang, M. Flury, J.B. Harsh, R.L. Zollars, Contact angles of aluminosilicate clays as affected by relative humidity and exchangeable cations, Colloids Surf. A: Physicochem. Eng. Aspects 353 (2010) 1–9.

[35] ImageJ, Available at: https://imagej.net/Welcome (accessed: 19th June 2018).

[36] R.T. Cygan, J.-J. Liang, A.G. Kalinichev, Molecular models of hydroxide, oxyhydroxide, and clay phases and the development of a general force field, J. Phys. Chem. B 108 (2004) 1255–1266.

[37] R.B. Best, X. Zhu, J. Shim, P.E.M. Lopes, J. Mittal, M. Feig, A.D. MacKerell, Optimization of the additive CHARMM all-atom protein force field targeting improved sampling of the backbone ϕ, ψ and side-chain $\chi1$ and $\chi2$ dihedral angles, J. Chem. Theory Comput. 8 (2012) 3257–3273.

[38] W.L. Jorgensen, J. Chandrasekhar, J.D. Madura, R.W. Impey, M.L. Klein, Comparison of simple potential functions for simulating liquid water, J. Chem. Phys. 79 (1983) 926–935.

[39] Y. Sugita, Y. Okamoto, Replica-exchange molecular dynamics method for protein folding, Chem. Phys. Lett. 314 (1999) 141–151.

[40] N. Pokhrel, L. Maibaum, Free energy calculations of membrane permeation: challenges due to strong headgroup-solute interactions, J. Chem. Theory Comput. 14 (2018) 1762–1771.

[41] S. Kumar, J.M. Rosenberg, D. Bouzida, R.H. Swendsen, P.A. Kollman, The weighted histogram analysis method for free-energy calculations on biomolecules. I. The method, J. Comput. Chem. 13 (1992) 1011–1021.

[42] J.S. Hub, B.L. de Groot, D. van der Spoel, g_wham—a free weighted histogram analysis implementation including robust error and autocorrelation estimates, J. Chem. Theory Comput. 6 (2010) 3713–3720.

[43] I. Arganda-Carreras, R. Fernández-González, A. Muñoz-Barrutia, C. Ortiz-De-Solorzano, 3D reconstruction of histological sections: application to mammary gland tissue, Microsc. Res. Tech. 73 (2010) 1019–1029.

[44] Analyze Skeleton. Available at: https://imagej.net/AnalyzeSkeleton. (accessed: 18th July 2018).

[45] Courtesy of Dr. B. A. Legg.

[46] T.C. Chao, O. Arjmandi-Tash, D.B. Das, V.M. Starov, Simultaneous spreading and imbibition of blood droplets over porous substrates in the case of partial wetting, Colloids Surf. A: Physicochem. Eng. Aspects 505 (2016) 9–17.

[47] T.C. Chao, O. Arjmandi-Tash, D.B. Das, V.M. Starov, Spreading of blood drops over dry porous substrate: Complete wetting case, J. Colloid Interface Sci. 446 (2015) 218–225.

[48] W.-J. Kim, S.-M. Yang, Effects of sodium salicylate on the microstructure of an aqueous micellar solution and its rheological responses, J. Colloid Interface Sci. 232 (2000) 225–234.

[49] H.-H. Liu, L. Li, J. Birkholzer, Unsaturated properties for non-Darcian water flow in clay, J. Hydrol. 430–431 (2012) 173–178.

[50] J. Das, C. Eun, S. Perkin, M.L. Berkowitz, Restructuring of hydrophobic surfaces created by surfactant adsorption to mica surfaces, Langmuir 27 (2011) 11737–11741.

[51] K.J. Shah, M.K. Mishra, A.D. Shukla, T. Imae, D.O. Shah, Controlling wettability and hydrophobicity of organoclays modified with quaternary ammonium surfactants, J. Colloid Interface Sci. 407 (2013) 493–499.

4.2 SUPPLEMENTARY INFORMATION

Brenda L. Kessenich[1], Nihit Pokhrel[1], Elias Nakouzi[2], Christina J. Newcomb[2], Markus Flury[3], Lutz Maibaum[1], James J. De Yoreo*[2,4]

[1]Department of Chemistry, University of Washington Box 351700, Seattle, WA 98195-1700

[2] Pacific Northwest National Laboratory, Physical Sciences Division, P.O. Box 999 Richland, WA 99352

[3] Washington State University, Department of Crop and Soil Sciences, 2606 W Pioneer, Puyallup, WA 98371

[4] University of Washington, Materials Science and Engineering, 302 Roberts Hall, Box 352120, Seattle, WA 98195-2120

*Corresponding Author (james.deyoreo@pnnl.gov)

The information contained in this supplement is intended to clarify methods and provide additional detailed results. Additional information is provided for sample preparation, imaging, simulation set-up, and image analysis. We include extra background information for why the physical droplet model was selected, and show a comparison of the droplet's actual volume and shape change over time with the mathematical predictions. Further, we provide tables of values from the figures in the paper, most critically of *a* and *K*. Tables of other variables, such as lipid aggregate size and area density, are also included. To support conclusions drawn in the paper about the lipid distribution within the film, we also provide tables comparing fluorescent lipid distribution and AFM topography. Finally, we include a complete table of r^2 values for the correlation plots, as well as correlation plots for which $r^2 > 0.8$.

S.1 Experimental details

1.1 "Gentle Hydration" method of creating aqueous lipid solutions. After drying the lipid/chloroform solution to the bottom of the test tube, the dried lipid film was allowed to hydrate in 18 MΩ·cm water uninterrupted for one hour, then was sonicated and heated in two minute cycles until all the lipid was in solution. Heating at 60 °C was required to fully solubilize lipid films. (Paper section 2.3)

1.2 AFM imaging parameters. Cypher AFM: AC240TS cantilevers are N-doped silicon with a nominal spring constant of 2 N/m and a frequency of 70 kHz. Most images were collected with a drive amplitude of 200-300 mV and scan rate of 1.2 Hz.

Icon AFM: Images were collected with a scan rate of 0.1 Hz, a drive amplitude of 300 mV, and an amplitude setpoint of 130 mV. (Paper section 2.4)

1.3 MD simulation set-up. We performed all simulation using Gromacs 5.1.4[46] with the Plumed 2.3[47] plugin under periodic boundary conditions. Temperature and pressure were maintained using a velocity-rescaled thermostat and the Parrinello-Rahman barostat, respectively. Long range electrostatic interactions were computed using the PME[48] method with a Fourier spacing of 0.12 nm. The real space Coulombic interaction was calculated up to 1.2 nm. Van der Waals interactions were calculated using a cutoff of 1.2 nm. Bond lengths were constrained using the LINCS algorithm[49]. Initial configurations were generated by inserting lipid molecules into previously equilibrated clay/water systems at random positions. These configurations were energy minimized and then equilibrated for 10 ns. After the system was equilibrated, production runs were simulated for 500ns. (Paper section 2.7)

1.4 Further explanation of image processing. An example of the image processing procedure outlined in section 2.8 is presented here.

First, **Figure 4-1** shows the step-by-step simplification of the original image to the skeleton. One ridge is highlighted to help guide the eye. In **Figure 4-1**, the ridge is in grayscale. In **Figure 4-1B**, as the ridge is above the threshold, it is now simply made of black pixels rather than grayscale pixels. In **Figure 4-1C**, the ridge is further reduced to a line which is one pixel wide and defined by the center of the black region. The skeletonized image provides information on the interconnectedness of the ridges, in the form of junction pixels where lines meet. It also provides information on ridge spacing, based off of the ratio of black pixels to total pixels.

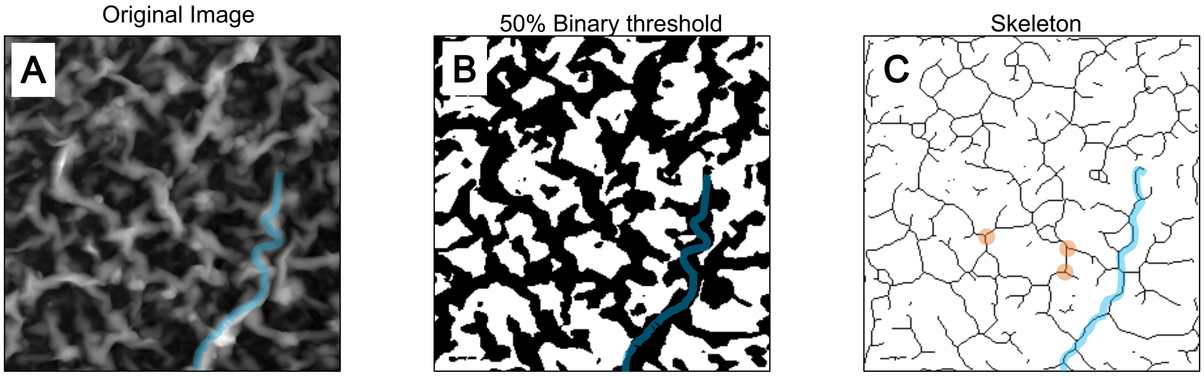

Figure 4-1: (S1) An example of image processing with annotation. (A) The original grayscale AFM image; 50x50 µm. (B) After the image is binarized at the 50% threshold, it is black above the threshold and white below. (C) The binarized image is then skeletonized. Each ridge has been reduced to a line that is one pixel wide. In (A), (B), and (C), the same ridge is highlighted in blue for clarity. In (C), several junctions – where two or more lines meet – are highlighted with orange circles.

Figure 4-2 shows the histogram of the number of pixels vs the gray scale value for each threshold and stage of processing. **Figure 4-2A** shows the histogram for the original image, which contains a multitude of gray values, ranked from 0 to 255 (white to black, respectively). The second column (**Figure 4-2B,D,F**) shows histograms for the binarized image at each threshold. The 25% threshold contains the largest amount of detail (the largest number of ridges), as only the lowest 25% of the image has been turned into white pixels, and the upper 75% has been turned into black pixels which will then be skeletonized. The 50% and 75% focus on progressively fewer. The 75% threshold preserves only the very highest ridges.

The third column (**Figure 4-2C,E,G**) shows the histograms of the skeletonized image at each threshold. The 25% threshold will always have more black pixels than the 50% threshold, which in turn has more than the 75% threshold. But, when these skeletons are compared to other images, they provide information on the relative interconnectedness and spacing of the ridges.

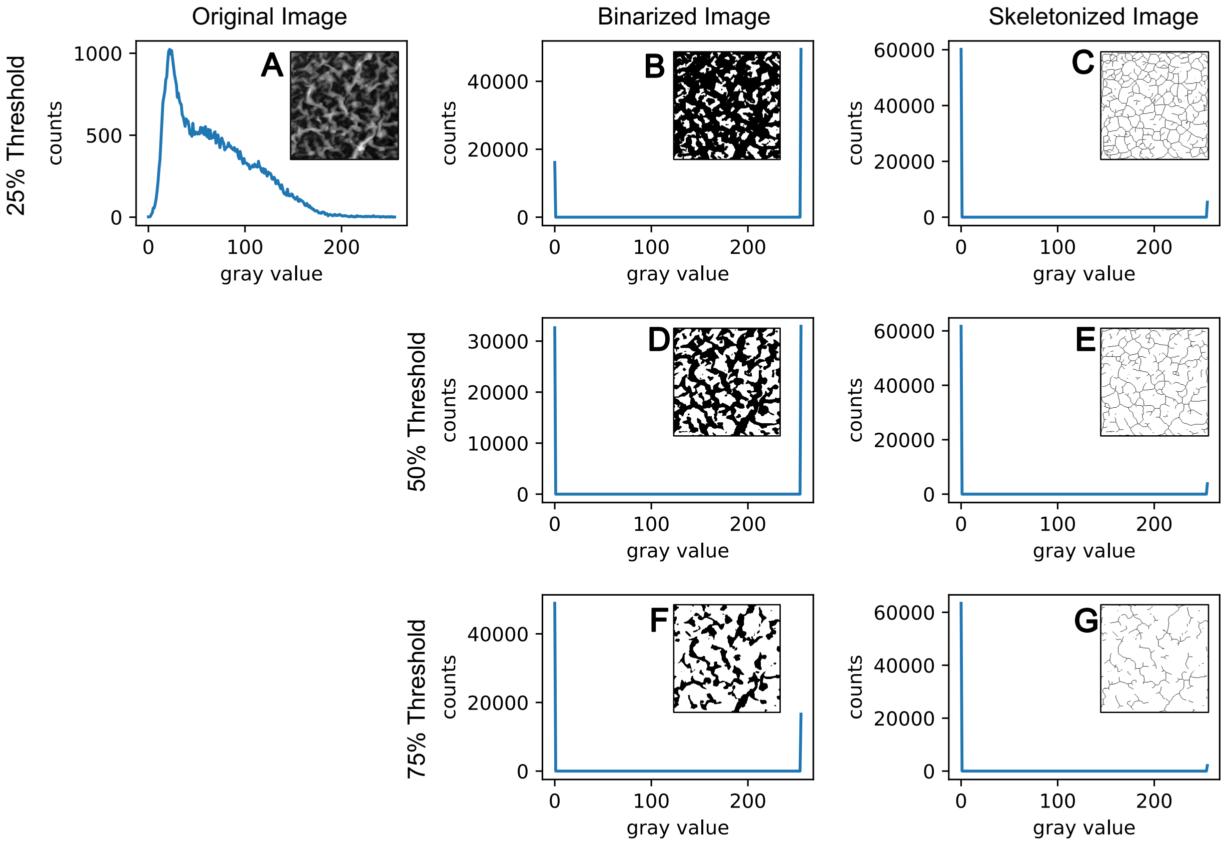

Figure 4-2: (S2) A complete example of image processing with histograms for each step. In the x-axis of each histogram, a value of 0 corresponds to white, a value of 255 corresponds with black, and each intermediate value is a unique gray. There are 65535 pixels in each image. The y-axis denotes the number of pixels having a particular gray value. Insets are the image at each step in processing. (A) The original grayscale image, 50x50 µm. Note the histogram has a variety of grays. (B) The result of binarizing the image at the 25% threshold; the lower 25% of (A) is now white, and the remaining values – those above the threshold – are black. (C) The result of skeletonizing (B). (D) and (E) represent the same process for the 50% threshold, and (E) and (F) are for the 75% threshold.

S.2 Physical model of droplet spreading and infiltration. Assuming the droplet is a spherical cap of radius R_d (**Figure 4-S3A,B**), the contact angle θ_c is related to the height *h* of the drop and the radius R_d through:

$$\frac{h}{R_d} = \csc\theta_c - \cot\theta_c \qquad \text{4.1 Droplet height}$$

The data exhibit reasonable agreement in the time dependence between the measured value of *h/R_d* vs time and that calculated from θ_c vs time using Eqn. 1 **(Figure 4-S3C)**. Therefore, the droplets can be approximated as a spherical cap, though the difference in magnitude of h/R_d indicated the droplets were slightly flatter than expected from the spherical cap model.

Second, because the film is much thinner than the droplet, during the initial spreading process, the volume V is constant and is given by:

$$V = \frac{2}{3}\pi \frac{R_d^3}{\sin^3\theta_c}\left[1-\frac{3}{2}\cos\theta_c+\frac{1}{2}\cos^3\theta_c\right] \qquad \text{4.2: Droplet volume}$$

The measured dependence of volume on time as calculated from equation 2 shows that volume is fairly constant on the timescale of the experiments (**Figure S3D**). We observed a decrease in droplet volume of approximately 10% over the course of 70 s. For a film only 10 µm thick, we

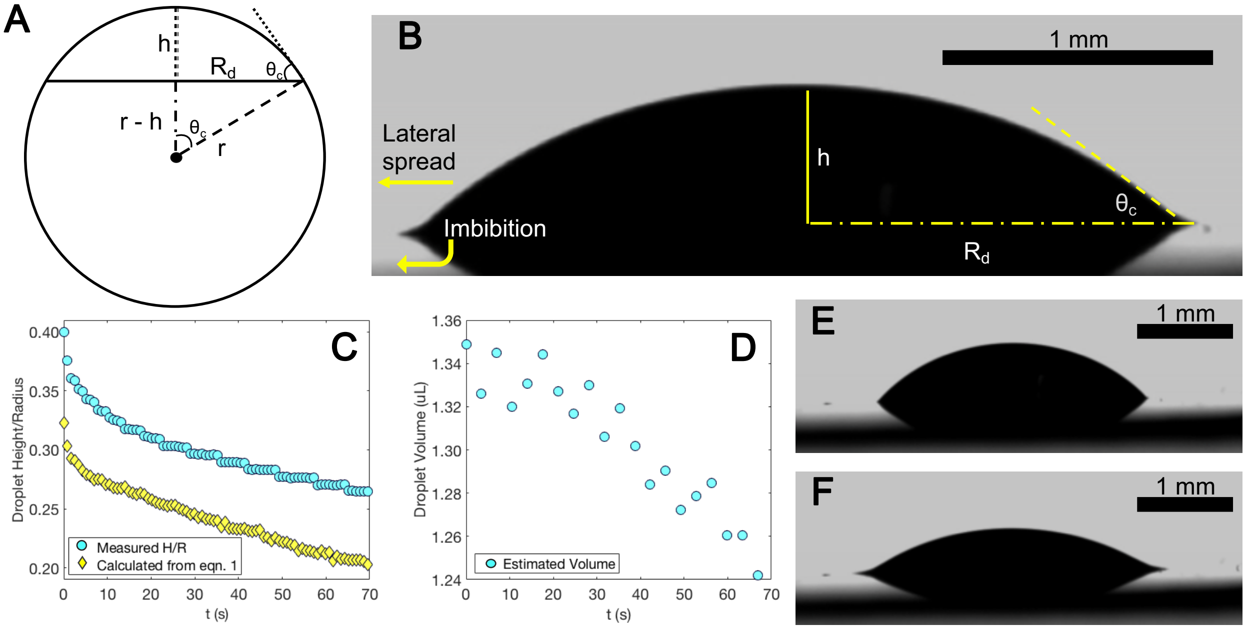

Figure 4-3: (S3) (A) The geometry of a spherical cap. A spherical cap is a section of a sphere cut off by a plane through the sphere. The simplest example of a spherical cap is a hemisphere, which occurs when R_d = r. (B) An example of a droplet on the film's surface with height h, radius R_d and contact angle θ_c marked, as well as the direction of lateral spread and imbibition. Lateral spread is not associated with a change in volume, while imbibition is associated with a decrease in volume. (C) Measured height/radius and calculated height/radius for a spherical cap. (D) Estimate of droplet volume based on the geometry of a spherical cap. (E) Example of a droplet 1s after deposition onto a clay/lipid film. (F) The same droplet after 70s.

estimate two-thirds of this volume loss could be evaporation, but for films greater than 20 µm thick, evaporation would not contribute appreciably to the volume loss.

Third, during the period of radius expansion, the dependence of the radius on time is expected to follow[28]:

$$\frac{R}{R_0} = [1 + Kt]^a \qquad \text{4.3 Droplet radius (1.5)}$$

where R_0 is the value of R at t=0, K is an inverse time constant that depends on many physical parameters of the film and the fluid, and a is constant depending on the value of the fluid behavior index n.

S.3 Values of *a, K,* and advancing contact angle

Table 4-1 shows the values of K, a, and, in the cases where the data on R(t) extend to R_{max}, the value of θ_{adv}.

Table 4-1: (S1) Values of the exponent a, time constant, and rate constant K for all samples. Values of θ_{adv} provided for lipid concentrations which reached R_{max} in the timespan of the experiment. Error is the standard deviation of all measurements.

Sample (% Coverage)	***a* average**	**Time constant, TC (s)**	***K* (*K* = 1/TC) (1/s)**	**Advancing CA (°)**
Montmorillonite 0	0.033 ± 0.002	1.9 ± 0.6	0.52 ± 0.17	25 ± 2
DOPE 10	0.030 ± 0.009	1.50 ± 0.19	0.67 ± 0.08	25.5 ± 0.8
DOPE 20	0.026 ± 0.004	0.98 ± 0.12	1.0 ± 0.13	27 ± 2
DOPE 25	0.051 ± 0.007	2.7 ± 1.9	0.4 ± 0.3	n.d.
DOPE 30	0.033 ± 0.012	1.3 ± 0.9	0.8 ± 0.5	24.6 ± 1.2
DOPE 40	0.046 ± 0.005	1.9 ± 1.1	0.5 ± 0.3	23 ± 2
DOPE 50	0.037 ± 0.008	1.3 ± 0.9	0.7 ± 0.5	23 ± 4
DSPE 10	0.015 ± 0.005	0.06 ± 0.07	16 ± 17	n.d.
DSPE 20	0.017 ± 0.002	0.4 ± 0.3	2.4 ± 1.9	n.d.
DSPE 25	0.023 ± 0.007	2.8 ± 1.3	0.36 ± 0.17	n.d.
DSPE 30	0.028 ± 0.0008	1.0 ± 0.3	1.0 ± 0.3	n.d.
DSPE 40	0.028 ± 0.009	0.6 ± 0.7	1.5 ± 1.6	n.d.
DSPE 50	0.0251 ± 0.013	0.44 ± 0.07	2.3 ± 0.4	n.d.
Montmorillonite Heated 0	0.0426 ± 0.0015	2.7 ± 1.2	0.38 ± 0.17	n.d.
Heated DSPE 10	0.07 ± 0.04	4.3 ± 1.5	0.23 ± 0.08	n.d.
Heated DSPE 20	0.087 ± 0.016	5 ± 2	0.19 ± 0.07	n.d.
Heated DSPE 25	0.032 ± 0.009	2 ± 2	0.5 ± 0.7	n.d.
Heated DSPE 30	0.08 ± 0.03	7 ± 3	0.14 ± 0.06	n.d.
Heated DSPE 40	0.10 ± 0.05	2.2 ± 1.5	0.5 ± 0.3	n.d.
Heated DSPE 50	0.06 ±0.02	4 ± 3	0.3 ± 0.2	n.d.

S.4 Lipid aggregate data

Table 4-2: (S2) Simulation average diameters are likely lower than experimental diameters due to box size constraints, and the number of available lipid molecules. Error is indicated by standard deviation on diameter measurements.

Lipid and % Coverage	Experimental average diameter (nm)	Simulation average diameter (nm)	Aggregate density estimate (1/nm^2)	Edge/total aggregates
DOPE 10	9 ± 2	4.02 ± 0.12	0.0010	10%
DOPE 26	4.8 ± 0.8	5.40 ± 0.13	0.1684	21%
DOPE 30	9.5 ± 1.5	n.d.	0.0023	n/a
DOPE 40	8.1 ± 1.5	n.d.	0.0048	21%
DOPE 50	7.1 ± 1.1	7.0 ± 0.2	0.0102	24%
DSPE 10	9.4 ± 1.5	2.88 ± 0.09	0.0004	85%
DSPE 26	6.9 ± 1.6	5.71 ± 0.14	0.0006	86%
DSPE 30	8.5 ± 1.4	n.d.	0.0008	98%
DSPE 40	12 ± 2	n.d.	0.0003	100%
DSPE heated 10	13 ± 3	4.34 ± 0.14	0.0007	74%
DSPE heated 26	10 ± 2	5.1 ± 0.2	0.0009	97%
DSPE heated 50	10 ± 2	7.1 ± 0.2	0.0119	17%

S.5 Lipid distribution data

Table 4-3: (S3) Comparison of fluorescence and AFM data for DOPE. Error indicates standard deviation; for samples where only one image was captured, two significant figures are presented.

Data Type and Binary Threshold	Sample	Ridge Separation	Junctions/µm^2
Fluorescence 50%	**DOPE 26% coverage**	0.131 ± 0.015	0.018 ± 0.003
Fluorescence 50%	**DOPE 50% coverage**	0.144 ± 0.011	0.04 ± 0.03
Fluorescence 75%	**DOPE 26% coverage**	0.075 ± 0.008	0.0067 ± 0.0007
Fluorescence 75%	**DOPE 50% coverage**	0.079 ± 0.005	0.014 ± 0.012
AFM 25%	**Montmorillonite**	0.08 ± 0.03	0.11± 0.06
AFM 25%	**DOPE 26%**	0.074 ± 0.011	0.09 ± 0.02
AFM 25%	**DOPE 50%**	0.10	0.14

Table 4-4: (S4) Comparison of the shape of DSPE patches in fluorescence to the shape of valleys seen in AFM topography. Circularity returns a value of 1 for a perfect circle. The Feret diameter indicates the maximum distance across a shape when it is sandwiched between two planes; the minimum Feret diameter is the minimum distance across the shape. Error indicates standard deviation. (There is no binary threshold because DSPE occurs in isolated patches, not as a complex network requiring multiple binary thresholds to visualize multiple levels of detail.)

Data Type	Sample	Circularity	Feret diameter (μm)	Minimum Feret diameter (μm)
Fluorescence	DSPE 10% coverage	0.913 ± 0.002	3.85 ± 0.18	2.6 ± 0.2
Fluorescence	DSPE 26% coverage	0.884 ± 0.009	3.84 ± 0.10	2.42 ± 0.06
Fluorescence	DSPE 50% coverage	0.838 ± 0.019	4.3 ± 0.5	2.6 ± 0.3
AFM “Valleys”	Montmorillonite 50% binary threshold	0.65 ± 0.09	4.6 ± 1.0	2.8 ± 0.7

S.6 Linear correlations: complete table and plots for correlations with $r^2>0.8$

Table 4-5: (S5) r^2 values from linear regressions for lipid-montmorillonite films. Wetting variables are labeled across the top, and physical variables down the side. For AFM film data, the MMT characteristics are not included in these regressions; they reduce the goodness of the fit, indicating that there are chemical influences at play in addition to the physical ones investigated here (see **Figure 7A**). The results are color-coded such that high r^2 values are darker/purple and smaller r^2 values are lighter/yellow. Correlations for which there are no data are marked n.d. and gray. (See **Figure 2** for definitions of “Ridge Separation” and “Junction Density”, as well as a visual reference for the various binary thresholds; see **Figure 7** for a visual reference on “Aggregate Density” and “Fraction of aggregates on clay edges”.)

Model r^2 values Fl. = Fluorescence	**Contact Angle, t=0**			**1/K**			**a**		
	DSPE	**DSPE-heat**	**DOPE**	**DSPE**	**DSPE-heat**	**DOPE**	**DSPE**	**DSPE-heat**	**DOPE**
Aggregate Density	0.00	0.09	0.77	0.18	0.10	0.85	0.10	0.01	0.59
Fraction of Aggregates on MMT Edges	0.86	0.33	0.03	0.14	0.34	0.07	0.63	0.15	0.41
Fl. Inverse Ridge Separation, 25% Binary Threshold	n.d.	0.69	0.95	n.d.	0.68	0.69	n.d.	0.86	0.29
Fl. Inverse Ridge Separation, 50% Threshold	n.d.	0.65	0.99	n.d.	0.64	0.92	n.d.	0.83	0.59
Fl. Inverse Ridge Separation, 75% Threshold	n.d.	0.59	0.88	n.d.	0.58	1.00	n.d.	0.78	0.84
AFM Inverse Ridge Separation, 25% Threshold	0.06	0.49	0.35	0.01	0.47	0.07	0.87	0.69	0.02
AFM Inverse Ridge Separation, 50% Threshold	0.03	0.48	0.42	0.02	0.47	0.11	0.92	0.68	0.01
AFM Inverse Ridge Separation, 75% Threshold	0.00	0.31	0.88	0.15	0.30	0.57	0.99	0.51	0.18
Fl. Junction Density 25% Threshold	n.d.	0.78	0.74	n.d.	0.77	0.39	n.d.	0.92	0.07
Fl. Junction Density, 50% Threshold	n.d.	0.71	0.76	n.d.	0.70	0.41	n.d.	0.88	0.08
Fl. Junction Density, 75% Threshold	n.d.	0.59	0.81	n.d.	0.57	0.48	n.d.	0.77	0.12
AFM Junction Density, 25% Threshold	0.06	0.51	0.39	0.01	0.50	0.10	0.88	0.71	0.01
AFM Junction Density, 50% Threshold	0.03	0.48	0.57	0.03	0.47	0.23	0.92	0.69	0.01
AFM Junction Density, 75% Threshold	0.04	0.49	0.24	0.02	0.47	0.02	0.91	0.69	0.06

All plots with $r^2 > 0.8$.

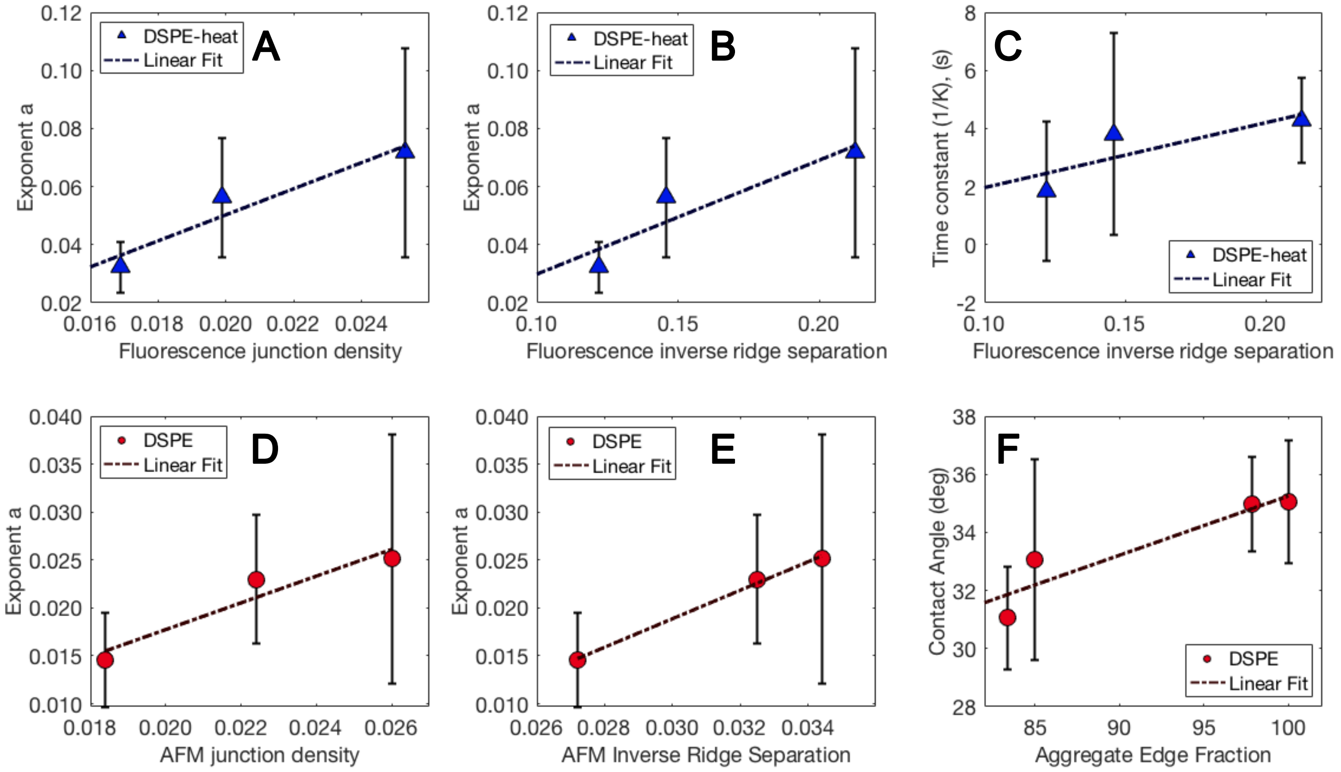

Figure 4-4: (S4) Correlations of physical and wettability variables for DSPE. A-C are for DSPE, D-F are heated DSPE. (A) Inverse ridge separation and exponent *a*. (B) Junction density from AFM images of the film and exponent *a*. (C) Aggregate edge fraction and contact angle. (D) Fluorescence ridge separation and time constant for heated DSPE. (E) Fluorescent ridge separation and *a*. (F) Fluorescent junction density and *a*.

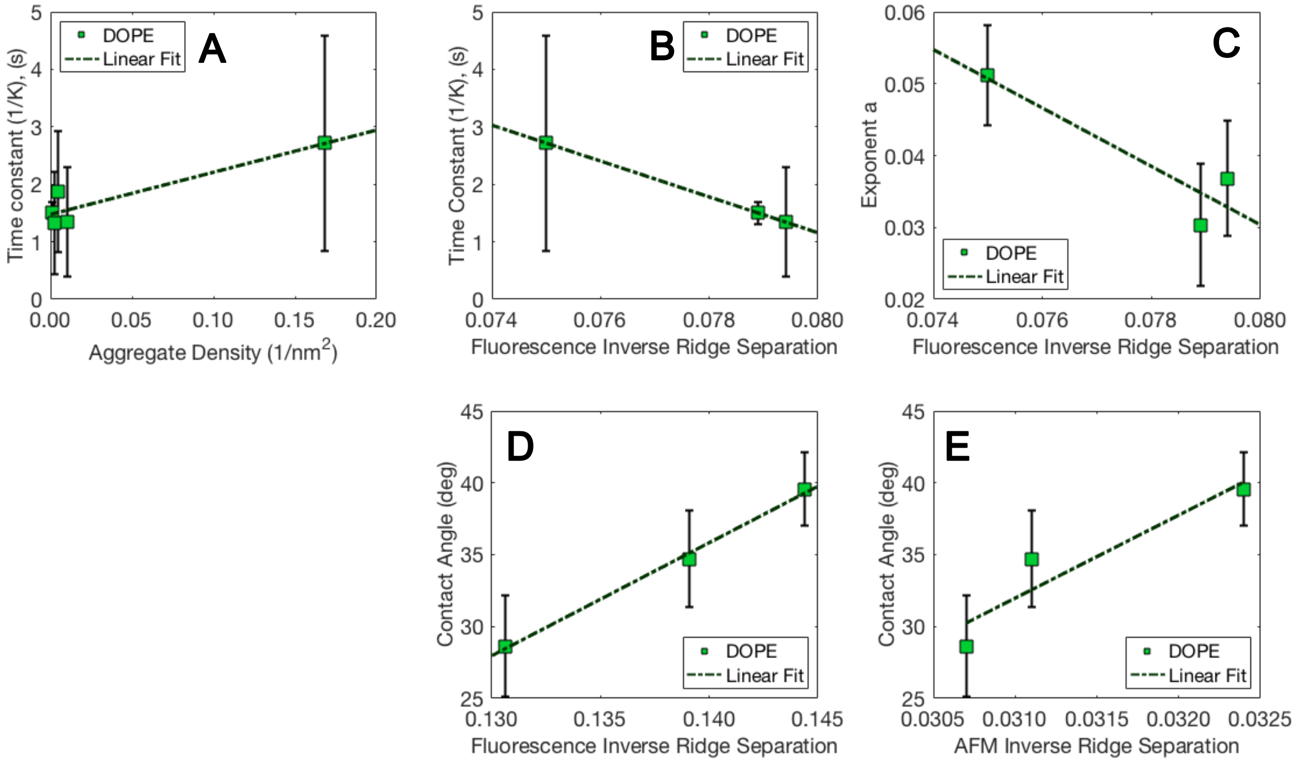

Figure 4-5: (S5) Correlations with $r^2>0.8$ between wettability parameters and physical characteristics for DOPE. (A) Aggregate density and time constant. (B) Ridge separation (AFM) and contact angle. Note that we measure inverse ridge separation. (C) Ridge separation (fluorescence) and contact angle, from the 50% binary threshold. (D) Fluorescence ridge separation and time constant (1/K), from the 75% binary threshold. (E) Fluorescence ridge separation and exponent *a*.

Chapter 5. NEGATIVELY-CHARGED LIPIDS EXHIBIT NEGLIGIBLE EFFECTS ON THE WATER REPELLENCY OF MONTMORILLONITE FILMS

This chapter contains a manuscript that I originally submitted to ACS Omega in February 2020. The text appearing in this chapter is the version I re-submitted to ACS Omega on March 16, 2020 after addressing one round of peer review on the initial submission. The paper was accepted at ACS Omega in May 2020 and appeared online on May 15, 2020.

I carried out most of the experimental work and analysis presented in this paper. Joshua K. Kibue performed some AFM imaging and image analysis. Dr. Nihit Pokhrel designed, ran, and analyzed the MD simulations.

5.1 MANUSCRIPT

Authors: Brenda L. Kessenich[a], Nihit Pokhrel[a], Joshua K. Kibue[b], Markus Flury[c], Lutz Maibaum[a], James J. De Yoreo[b,d]*

[a] University of Washington Department of Chemistry, [b] University of Washington Department of Materials Science and Engineering, [c] Washington State University Department of Crop and Soil Sciences, [d] Pacific Northwest National Laboratory Physical Sciences Division

*Corresponding Author

Keywords: lipids, clay, non-Newtonian flow, nanotopography

Abstract

Amphiphilic molecules can alter the wettability of soil minerals. To determine how the headgroup chemistry of amphiphiles determines these effects, we investigate a system of the clay montmorillonite with long-chain phospholipids. We use phosphatidylglycerol (PG) phospholipids to contrast with our previous work using phosphatidylethanolamine lipids (PE). Zwitterionic PE lipids can sorb to the negatively-charged montmorillonite surface, whereas negatively-charged PG lipids cannot. Employing a suite of techniques from molecular dynamics, atomic force microscopy, fluorescence microscopy, and contact angle measurements, we define sample characteristics from molecular scale structure to the macroscopic wettability. We find that PG lipids do not significantly alter montmorillonite wetting characteristics, such as the contact angle, flow viscosity, and the characteristic timescale for droplet imbibition. In comparing PE and PG lipid/clay films, we find that, among the phospholipids compared, they must have three characteristics in order to change clay/lipid film wettability: they must bind to the mineral surface, be solid at room temperature, and have a relatively continuous distribution throughout the film.

Introduction

Soil water repellency (SWR) is a phenomenon in which soils do not readily absorb and retain water[22]. While SWR negatively affects a number of environmental phenomena, such as causing non-uniform water infiltration[50] and increasing surface runoff and erosion[51], the underlying mechanisms that cause it are not well understood.

Organic matter in soil is generally considered a main source of SWR[52]. Numerous prior studies suggested that amphiphilic molecules have a particularly pronounced impact on SWR[13]. Most previous work characterizing SWR has been done with either natural organic matter[16] or bulk soils[17]. While such studies show that different soils have different degrees of water repellency and that organic matter and soil water content are important factors controlling water repellency, only a few studies determine the underlying mechanisms by performing both imaging and wettability measurements on a particulate surface[12]. Therefore, in order to determine the mechanism by which lipids cause SWR, we investigated model systems consisting of one lipid and one particulate mineral.

Previously, we analyzed a system of montmorillonite and zwitterionic phosphatidylethanolamine (PE) lipids[44]. One saturated PE lipid, DSPE (1,2-distearoyl-sn-glycero-3-phosphoethanolamine) and one unsaturated PE lipid, DOPE (1,2-dioleoyl-sn-glycero-3-phosphoethanolamine) were studied in order to determine if the state of the lipid — liquid or solid — altered wettability. We found that the liquid, unsaturated lipid and the solid, saturated lipid had very different distributions in the film at the nanoscopic and microscopic levels. The solid, saturated DSPE was present as isolated islands in the film, while liquid, unsaturated DOPE was distributed throughout the sample film. The most significant alteration of wettability (as measured by contact angle and imbibition kinetics) occurred when DSPE was melted, and then mixed with the montmorillonite particles before cooling, creating a situation where a solid lipid was distributed throughout the film. Previous literature reports have hypothesized that water flow in clay is non-Newtonian[30], that is, the liquid viscosity changes under stress. Our results agree with these prior reports, as we found that the spreading characteristics of water droplets on the films implied that the water exhibited non-Newtonian behavior in the form of shear-thinning (reduction of viscosity) during imbibition into the film[30]. Relative to clay alone, melted DSPE caused water to have a *higher, more viscous* fluid index and, therefore, more Newtonian behavior than was present in the clay alone. This suggested that a solid lipid distributed through the film could change the wettability more than a solid, non-distributed lipid or a liquid, distributed lipid. In all cases, the PE lipids were able to sorb to the montmorillonite surface.

For this work, we selected lipids that do not readily bind with mineral surfaces, and thus should have a less pronounced effect on wettability. To this end, we investigated the mechanisms by which water repellency is altered by negatively-charged phosphatidylglycerol (PG) lipids on montmorillonite. Due to the PG headgroup's negative charge, PG lipids are not expected to sorb to the montmorillonite planar surface. One saturated, solid lipid (DSPG) and one unsaturated, liquid lipid (DOPG) were investigated for direct comparison with DSPE and DOPE. All four lipids (DOPE, DSPE, DOPG, and DSPG) have two 18-carbon tails. Our results indicate that both the headgroup and tailgroup chemistry influence lipid-induced changes in SWR.

Experimental

Techniques were selected to encompass scales from molecular to macroscopic. At the smallest scale, molecular dynamics simulations provide information on the type of aggregates formed by the lipids and the binding strength of those aggregates to the mineral surface. Atomic force microscopy and fluorescence microscopy were used to characterize the film surface and distribution of lipid through the films. Wettability was measured with the water contact angle, flow viscosity, and kinetics of infiltration. A complete description of the methods and materials used is provided in Kessenich et al. 2019 and the associated supplement[44].

2.1 Materials and sample preparation. The lipids DOPG (1,2-dioleoyl-sn-glycero-3-phospho-(1'-rac-glycerol)) and DSPG (1,2-distearoyl-sn-glycero-3-phospho-(1'-rac-glycerol)) were acquired from Avanti Polar Lipids. Montmorillonite was purchased from the Clay Minerals Society and further ion-exchanged to fully saturate the sorption sites with sodium cations. Lipid/montmorillonite films were prepared as follows. Lipids were suspended in water via the gentle hydration method for making small unilamellar vesicles. However, it is known that PG lipids do not readily form vesicles in aqueous solution[53].

The lipids were then mixed with montmorillonite suspensions, at ratios where the surface area of lipid added was known, assuming a monolayer lipid coverage on the mineral surface:

$$\%\,Coverage = 100 * \frac{total\ lipid\ surface\ area}{total\ montmorillonite\ surface\ area} \tag{1}$$

Equation 1 does not represent the true coverage, only a theoretical maximum coverage as a lipid monolayer (reported as percent coverage as monolayer, %CAM). An area per molecule[54,55] of 60 Å^2 and a montmorillonite surface area[56] of 22.7 m^2/g were used.

The aqueous mixtures of lipid and clay were then pipetted onto freshly-cleaved mica surfaces and allowed to air dry overnight. For wettability measurements, fluorescence microscopy, and large-scale AFM, 16 mg/mL montmorillonite suspensions were used. 1 mg/mL montmorillonite was used for small-scale AFM.

2.2 Atomic force microscopy (AFM). To identify lipid aggregates on the surface of the films, an Asylum Cypher ES was utilized to image at scales under 5 μm. To image the film topography, a Bruker ICON was used to image at scales of 50 μm. In all cases, imaging was performed with Asylum AC240TS cantilevers, which have a spring constant of 2 N/m and a frequency of 70 kHz.

2.3 Molecular dynamics (MD) simulation. The system was modeled the same way as in our previous paper using a CLAYFF force field for the montmorillonite, CHARMM36 force field for the lipids, and the TIP3P forcefield for the water[44]. The shapes of the DSPG lipid aggregates were also inferred in a similar way; we computed the density of tail carbon atoms and head phosphorus atoms, as DSPG does not have a nitrogen atom in the headgroup. We calculated the binding energy of a single DSPG lipid onto the surface of the clay using Replica Exchange Umbrella Sampling where we bias the distance between the phosphorous atom in the lipid head and the surface of the clay. We simulated 35 windows each 0.1 nm apart with a constraint of 500 (kJ/mol)/nm^2. All other simulation protocols remain the same as in the previous paper.

2.4 Fluorescence microscopy. To map the distribution of lipid within the film across hundreds of microns, 1 mol % Rhodamine-DMPE dye was mixed into the lipids prior to film preparation. The resulting distribution of fluorescence intensity was imaged with a Nikon Y-FL epifluorescence microscope. Brightness in the fluorescence images is proportional to the amount of lipid present in a given location.

2.5 Wettability. Initial contact angle and droplet shape over time were monitored with a Kruss DSA100. Five or more droplets were observed for each sample. In addition to the initial contact angle, the droplets were video-recorded for 70 s as they spread out and imbibed into the sample films. The radius was extracted using a custom MATLAB script and fit with Equation 2 using Python's Scipy *optimize.curve_fit* function.

We determined the wettability of our systems with a method adapted from Chao et al[27,28]. Briefly, a water droplet is placed on the sample surface, and the change in the droplet radius is monitored over time. The radial expansion of a droplet spreading across a porous surface where the fluid can also infiltrate into the sample is described as follows:

$$\frac{R}{R_0} = [1 + Kt]^a \tag{2}$$

where R is the droplet radius, R_0 is the droplet radius at t = 0, K is an inverse time constant ($TC = 1/K$), and a is a proxy for the fluid index. K depends on a number of material properties of the film and fluid. For our system, a is related to the fluid index n by:

$$a = \frac{n}{1+n} \tag{3}$$

The fluid index n indicates the deviation of fluid behavior away from that of a Newtonian fluid. In a Newtonian fluid, the fluid viscosity is independent of strain, the fluid index $n = 1$ and $a =$

0.5. Shear-thinning fluids, which have reduced viscosity under strain, have $n < 1$ and $a < 0.5$, while shear-thickening fluids have $n > 1$ and $a > 0.5$.

The wettability variables of initial contact angle, *TC*, and *a* will be used below to characterize the wettability of the films.

2.6 Image processing and quantification. Fluorescence and large area (50x50 μm^2) AFM images of sample topography were analyzed using the same procedure as in our previous publication. Briefly, each image was turned into a binary image at three different thresholds: 25%, 50%, and 75% **(Figure 1)**. The threshold percentage (e.g, 25%) renders everything below the that percentile of the gray value white and everything above it black. Using multiple thresholds enables capture of morphological detail that would be lost if only one threshold was used.

After binarization, each image was skeletonized with ImageJ, which reduces the dark portions of the binarized images to a line one pixel wide down the center of the prior black region. The skeletonized images were then analyzed with the ImageJ macro *Analyze Skeleton* to obtain the number of pixels where the lines meet, which gives an indication of the interconnectedness of the AFM topography. Junctions are reported as the number of junction pixels per square micron.

The ratio of dark to light pixels in the skeletonized images were also recorded, as this gives an indication of ridge spacing in the case of AFM topography images, and of lipid density in the case of fluorescence images. The ratio will henceforth be abbreviated as the "skeleton ratio." For AFM topography images such as **Figure 1A**, the skeleton ratio is inversely proportional to the separation of the ridges in the topography. For fluorescence images such as in **Figure 4**, the skeleton ratio reflects the degree to which the lipid spreads through the film (a film with very patchy lipid distribution will have a small skeleton ratio, and a film with a more continuous lipid distribution will have a larger skeleton ratio).

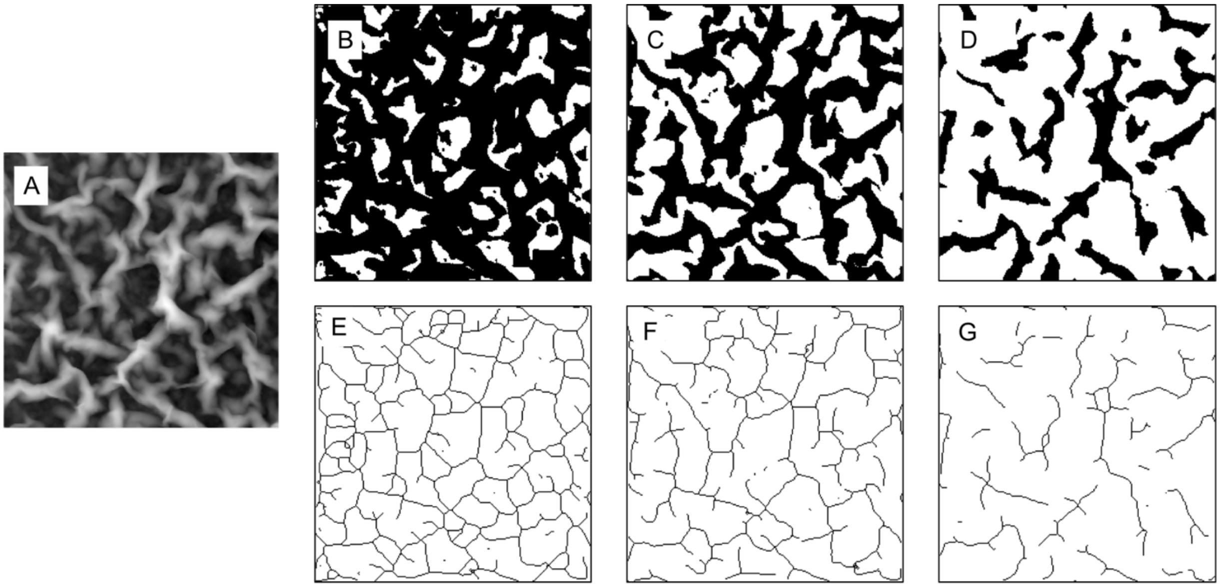

Figure 5-1: An example of image processing for a 50x50 µm DOPG/montmorillonite film. The image is first turned into a binary image at three thresholds: B) a 25% threshold where only the bottom 25% of the image was left white, C) the bottom 50% of the image is light, and D) the bottom 75% of the image is white. The binary images are then skeletonized (E-G). This reduces a complex grayscale image to one-pixel-wide lines which can be easily counted and quantified. The ratio of dark/light pixels in the skeletonized images will be referred to as the "skeleton ratio."

Results & Discussion

3.1 Lipid morphology. AFM imaging showed two dominant lipid morphologies on the film surface: small, roughly circular lipid aggregates and bilayer sheets **(Figure 2, Figure S5)**. Relative to PE lipids, PG lipid aggregates strongly preferred edge sites on the montmorillonite flakes **(Table 1, Figure 2, Figure S2)**. DSPG formed spherical aggregates under 30% coverage, and formed patchy bilayer sheets above 30% coverage **(Figure 2B, 2C)**. This behavior is similar to that of the saturated lipid DSPE, which switched from forming small aggregates to forming bilayers at 40% coverage. We conclude that this change in morphology is linked to the state of the lipid at the temperature at which the film is prepared, as both DSPE and DSPG are solid at room temperature, while DOPG and DOPE, which continue forming spherical aggregates at higher coverage, are liquid at room temperature. (DSPE can be forced to form spherical aggregates at higher coverage by preparing the films above its melting temperature; this case will be referred to as “melted DSPE” or “heated DSPE”.)

Aggregate heights were measured for DSPG at 25% coverage. Aggregates ranged in height from 0.3 nm to 6.4 nm, with the average height at 2.8 ± 1.7 nm. As the average aggregate was around 13 nm in diameter, the taller heights (> 2 nm) are consistent with a hemi-micellar surface structure. Shorter heights may represent collapsed micelles or hemimicelles.

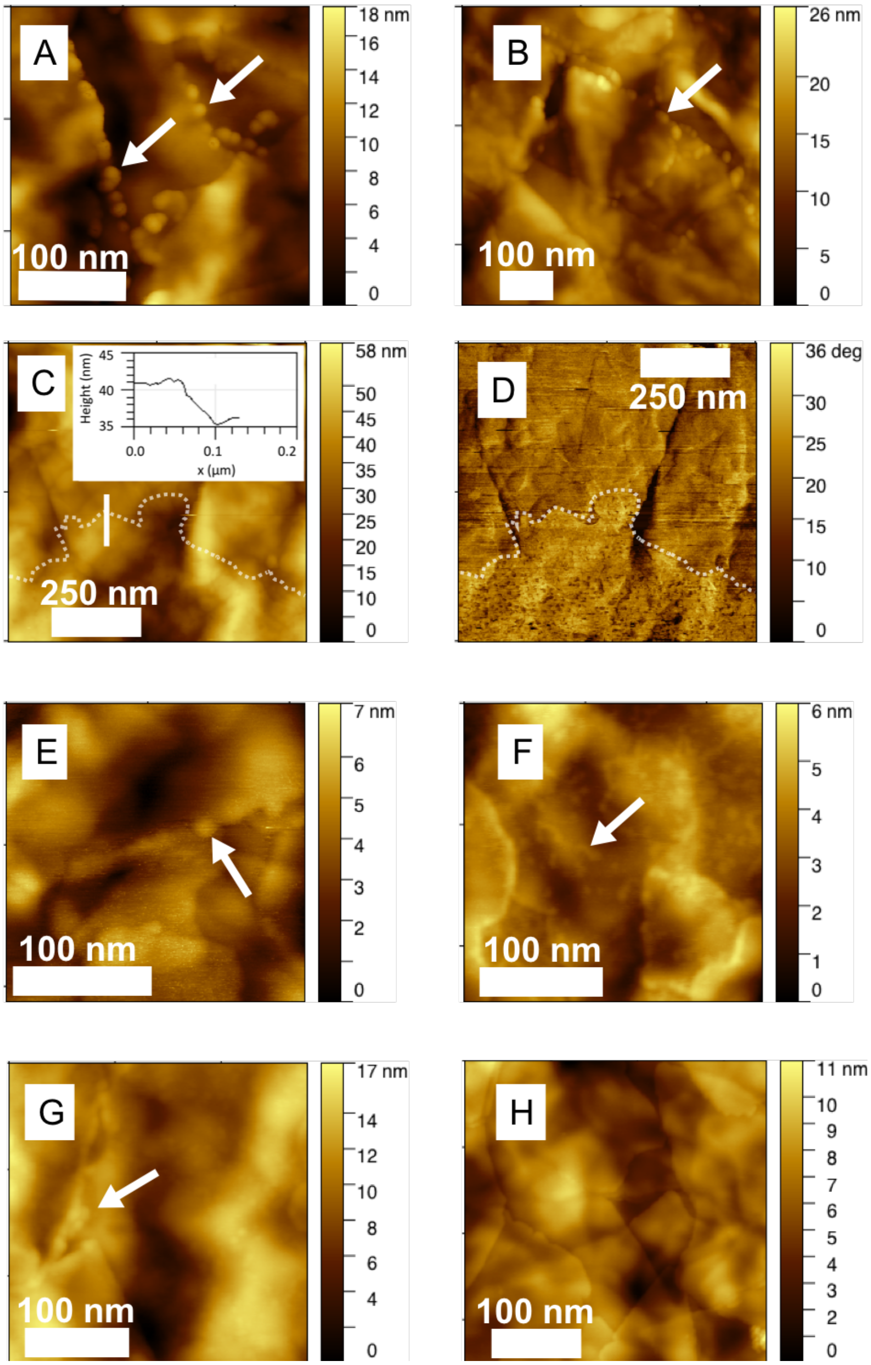

Figure 5-2: Lipid aggregates on montmorillonite imaged with AFM topography. Arrows indicate typical aggregates. See the SI for a cartoon version of this figure for additional clarification of the features present. A: DSPG at 10% coverage. B: DSPG at 25% coverage. C: DSPG at 50% coverage. Inset: Height profile of the edge of a DSPG bilayer on the surface. Additional height profiles are presented in Figure S3. D: Phase image of C, which more clearly shows the DSPG bilayer in the lower portion of the image. The DSPG bilayer is outlined in both C and D. E: DOPG 10% coverage. F: DOPG 25% coverage. G: DOPG 50% coverage. H: Montmorillonite with no lipid added. Panel reprinted with permission from Kessenich et al., 2019 J. Colloid Interface Sci. 555, 498–508, copyright 2019 Elsevier.

Table 5-1: Fraction of aggregates on clay flake edges out of the total number of spherical aggregates counted. Typically, over 30 aggregates were counted for each sample, except for DOPG 10% coverage, which was difficult to image. The number of aggregates on the edge was then divided by the total number of aggregates to obtain the fraction of aggregates on the edge.

Lipid	% Coverage	Fraction of aggregates on clay edges	Aggregate diameter (standard deviation)
DOPG	10	0.89	11.7 ± 2.7
	25	0.80	7.9 ± 1.8
	50	0.11	6.6 ± 1.2
DSPG	10	1.00	11.8 ± 2.1
	25	0.97	13.3 ± 2.6
	30	0.92	5.4 ± 1.3
	40	NA; forms bilayers	NA; forms bilayers
	50	NA; forms bilayers	NA; forms bilayers

3.2 Simulation results. Molecular dynamics suggests DSPG lipids, which have negatively charged headgroups, do not bind to the surface **(Figure 3)**. The montmorillonite surface is also negatively charged, so the lipids are repelled from it, and freely float in water instead (note that water molecules are not shown in **Figure 3** for clarity). A single DSPG lipid molecule prefers bulk water by 2 kJ/mol over the montmorillonite surface. The maximum in the free energy profile lies at the surface of the clay. This also means that the aggregates seen on the montmorillonite with AFM **(section 3.1)** were most likely forced onto the surface by the drying process. As is the case with single lipids, the aggregates also prefer the bulk water. The headgroups orient towards the water, forming perfect spherical micelles at 25% coverage or cylindrical micelles at 50% coverage. We infer this from the symmetric nature of all four number density profiles in **Fig. 3 D**. The tail density profiles for both coverages is unimodal. The phosphate density for 25% does not have any peak, and that of 50% is bimodal.

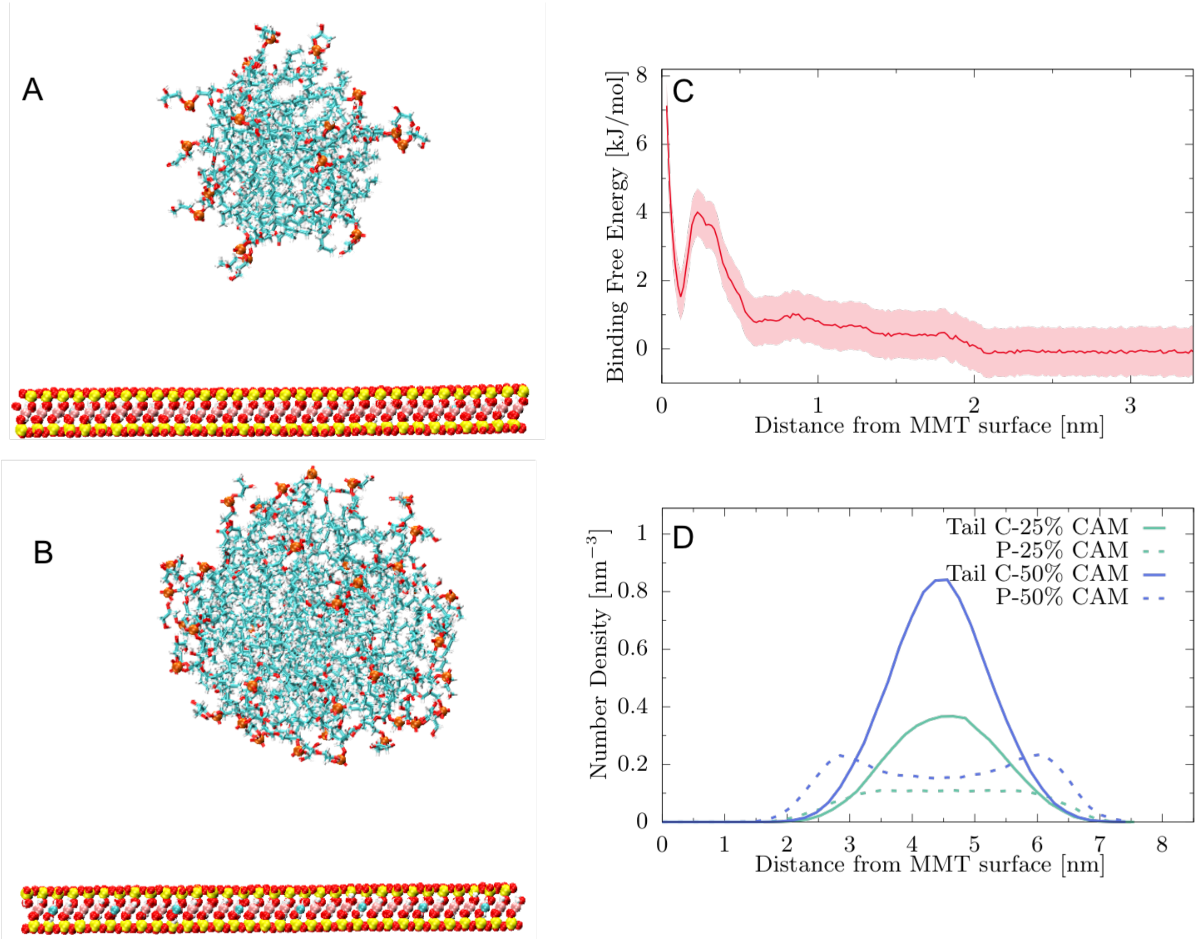

Figure 5-3: Results from MD simulations. Representative simulation snapshots are shown in panel A (25% CAM) and B (50% CAM), where lipid phosphorous is represented in orange and oxygen in red. The clay oxygen, silicon, aluminum and magnesium are represented in red, yellow, pink and cyan respectively. The ions and water molecules in the simulation are not shown for clarity. The free energy of single lipid aggregate binding to the surface of the montmorillonite is not favorable for single DSPG molecules (C). Density plots for the freely floating aggregates are presented in D.

3.3 Lipid distribution in the film. Both DOPG and DSPG are relatively continuously distributed through the film **(Figures 4, S7)**. As seen before, the web-like pattern in the fluorescence is linked to the film's texture at the scale of tens of microns. However, DSPG is solid at room temperature and, as such, we expected its distribution to be discontinuous, consisting of isolated aggregates that tend to lie away from the ridges, as was the case with DSPE[44] **(Figure 4C).** The reason for the difference between the distribution of DSPG and DSPE is unclear. DSPG's melting temperature, 55°C, is lower than DSPE's of 74°C, so we hypothesize that in between these temperatures, there is a melting point that divides continuous from discrete distributions or a temperature range over which the distribution transitions from continuous to discrete. We hypothesize that such a temperature could be the critical temperature separating the formation of micelles and the formation of bilayers. As shown in the MD simulations, DSPG forms spherical micelles in solution **(Figure 3)**, whereas DSPE aggregates were in the form of bilayers[44].

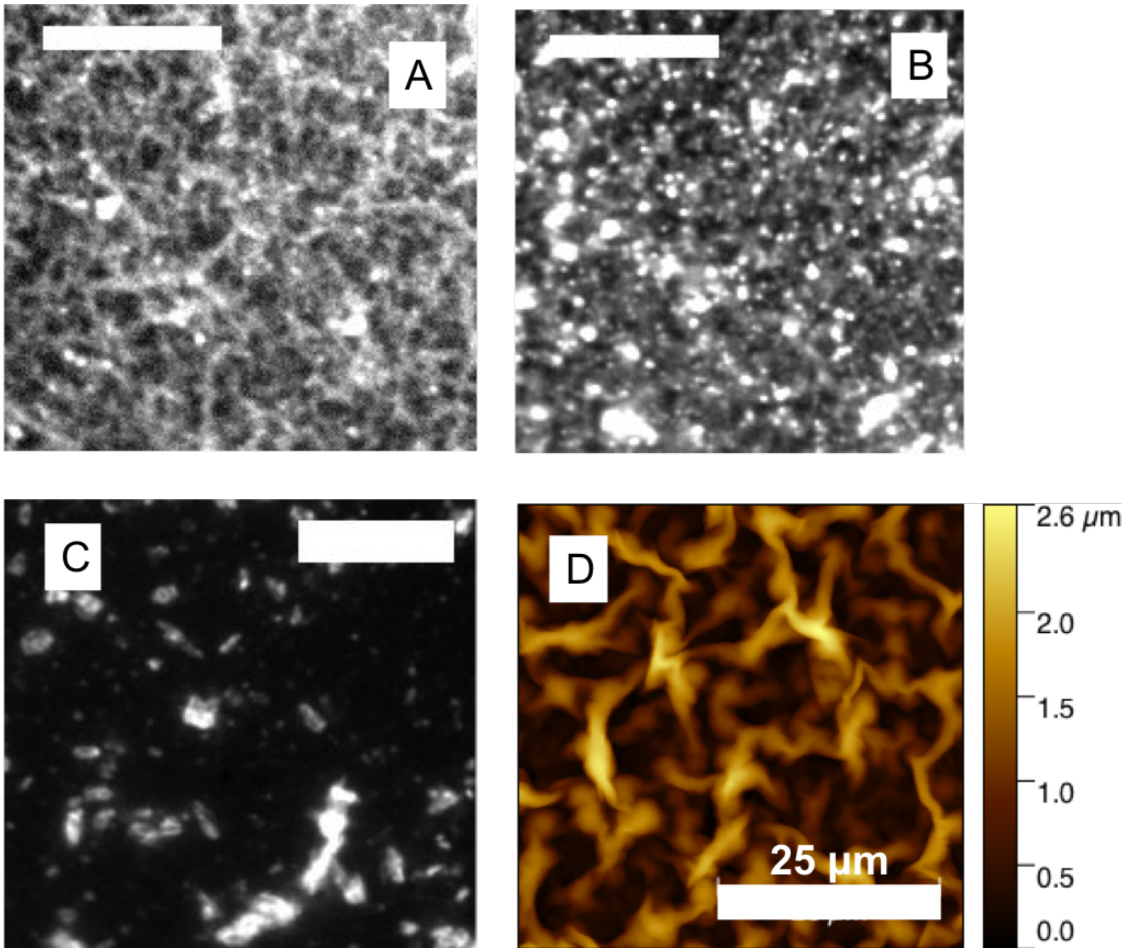

Figure 5-4: Film topography and lipid distribution. A-C) Fluorescence images of the film. Scale bars are 50 µm. Brighter regions contain more lipid, and darker areas contain less lipid. A) DSPG at 26% coverage. B) DOPG at 26% coverage. C) DSPE at 26% coverage; reprinted with permission from Kessenich et al., 2019 J. Colloid Interface Sci. 555, 498–508, copyright 2019 Elsevier. D) AFM image of the film topography. For additional fluorescence images, please refer to the SI.

3.4 Wettability. DSPG does not significantly change the contact angle or the value of *a*. DOPG reduces the contact angle slightly, but does not alter either the fluid index proxy *a* or the time constant of imbibition *TC* **(Figure 5A-C, Figure S4)**. Humidity likely changes *a,* as the *a* measured for montmorillonite in these experiments was lower than that reported in our previous paper and the only known factor that was different was the laboratory's relative humidity. For the previous paper, the wettability was measured at between 30% and 40% relative humidity, whereas this data was collected between 40% and 50% humidity. Both sets were collected at 29°C.

That PG lipids do not significantly change *a* or TC is unsurprising, given that non-Newtonian flow — i.e., degree of shear thinning — (see **eqn. 2**) in clay is due to water-clay interactions. Therefore, if the PG lipids do not stick to the clay and thus alter the interfacial water-clay interactions, no change in fluid behavior is expected.

Among all lipids tested, melted DSPE caused the largest changes in contact angle, *a,* and *TC* **(Figure 5A-C, Table 2)**. The PG lipids caused the least change, with DOPE and DSPE having intermediate effects. The primary difference between the PG and PE lipids is that the PG lipids do not bind to the clay surface, while PE lipids do bind. Therefore, we conclude that, in order to alter wettability, the lipids must have a headgroup that interacts with the montmorillonite surface.

The degree of shear thinning is not, in the case of the PG lipids, linked to the time constant of imbibition **(Figure 5D and S5)**, but as there is essentially no variation in either *a* or *TC*, this finding is also reasonable given that the time constant must be affected by the fluid viscosity. In contrast, for the PE lipids where both parameters vary over a substantial range, there is a strong correlation between water that exhibits less shear thinning (larger, more viscous *a*) and slower flow (larger *TC*) **(Figure 5D).** There is also a strong relationship between higher contact angle and lower degree of shear thinning (larger *a*) for heated/melted DSPE **(Figure 5E, eqn. 3)**. This suggests that, for some lipids, more surface hydrophobicity and less shear thinning are linked. This result is consistent with the conclusion in our previous study[44] that heated DSPE leads to less shear thinning, because the molten lipid, which spreads throughout the film, solidifies upon cooling and thus creates larger separations between the individual montmorillonite flakes as the film dries. These larger spaces mitigate the shear thinning effect of smaller inter-flake separation in the lipid-free film. However, while there is also a positive correlation between contact angle and time constant **(Figure 5F)**, that correlation is weaker. Thus the other materials factors that impact *TC*[18] appear to weaken the correlation between surface hydrophobicity and the speed of imbibition even when surface hydrophobicity and degree of shear thinning are strongly correlated.

Table 5-2: The percent difference between the measurement on plain montmorillonite and the measurement with lipid that most deviates from the montmorillonite value. Darker colors indicate a larger difference.

	Largest % difference for each lipid and each wettability variable				
	Binds to surface			**Does not bind to surface**	
	DOPE	**DSPE**	**DSPE-melted**	**DOPG**	**DSPG**
Contact Angle	**-16**	**-9**	**+54**	**-19**	**-11**
TC (1/K)	**-49**	**-97**	**+174**	**+17**	**+19**
a	**+54**	**-56**	**+140**	**+17**	**+11**

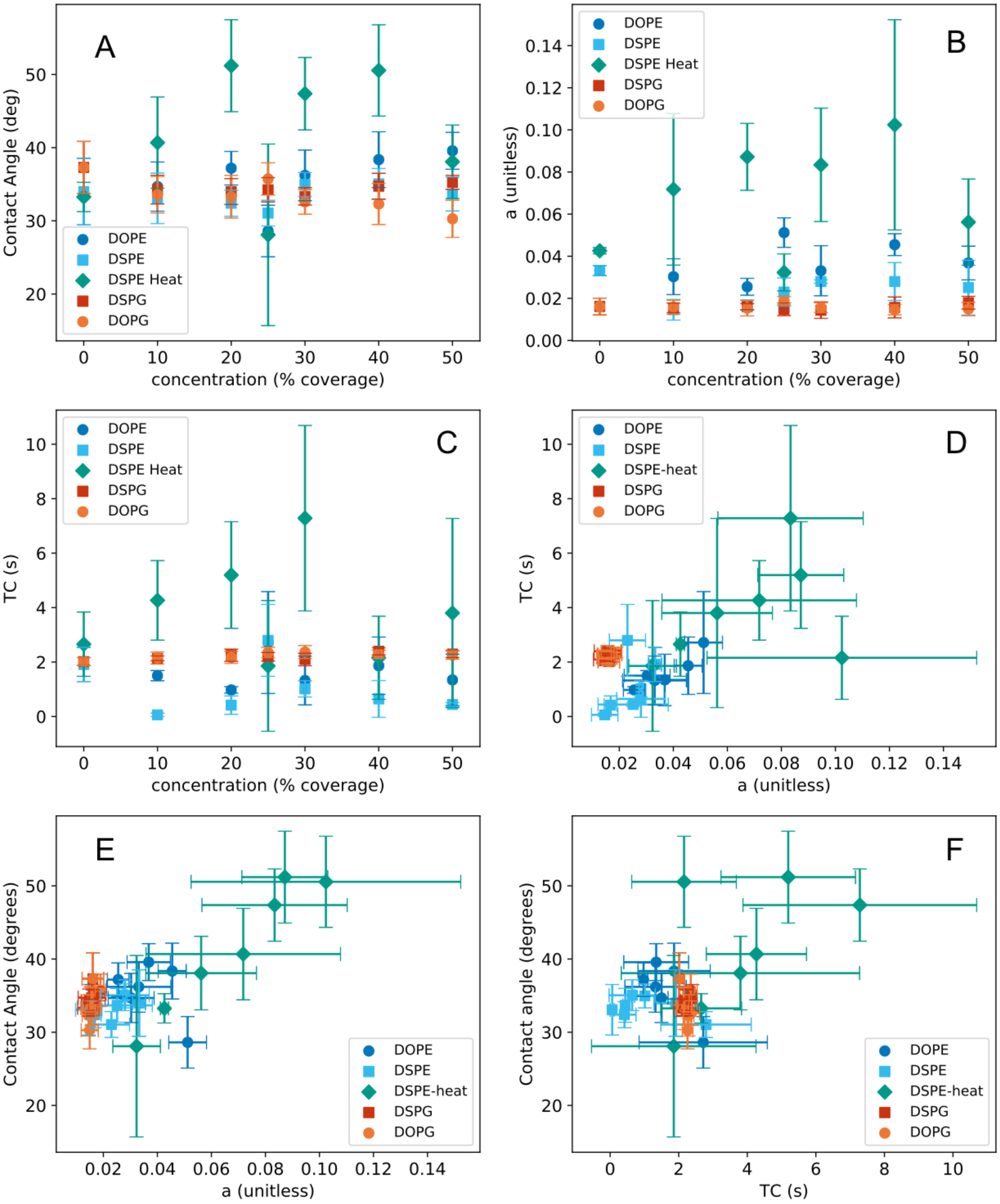

Figure 5-5: Comparison of PE and PG lipid wetting characteristics. Error bars indicate standard deviations. (A) Contact angle. (B) Exponent a. Note that the value of a is likely lowered by increased humidity. (C) Time constant TC. (D) Comparison of the time constant TC and flow viscosity (a) for PE and PG lipids. (E) Comparison of the contact angle and a. (F) Comparison of the contact angle and TC. PE data reprinted with permission from Kessenich et al., 2019 J. Colloid Interface Sci. 555, 498–508, copyright 2019 Elsevier. See Fig. S4 and S5 to view PG data on expanded axes.

3.5 Connections between wettability (a, TC, contact angle) and physical parameters (lipid aggregate density and location, lipid distribution, and film topography). Relative to PE lipids, PG lipids exhibited few strong correlations between wettability and physical variables **(Table 3, Figures 6, S8, S9, Table S2)**. As the PG lipids have limited impact on *a* and *TC,* even strong linear correlations have little causative meaning.

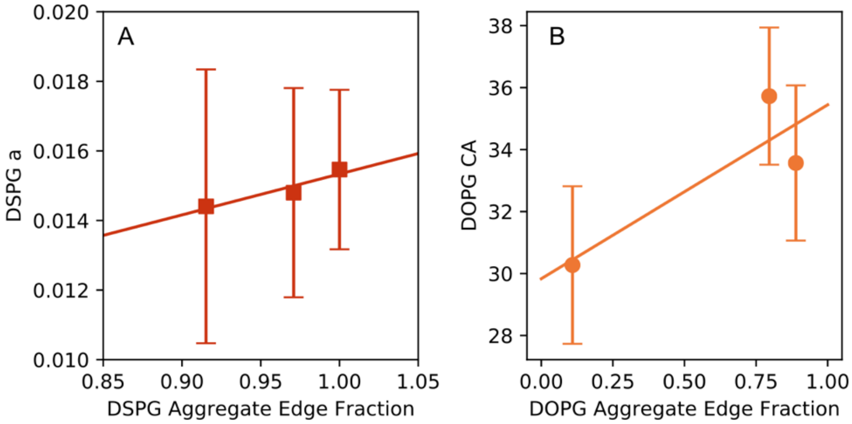

Figure 5-6: Correlations between a physical variable (the fraction of lipid aggregates present on clay flake edges) with wetting variables: A) DSPG *a* values, and B) DOPG contact angle.

For DSPG, the contact angle showed correlations with the size, density, and edge preference of the lipid aggregates **(Figure 6B)**, but the error bars preclude strong conclusions about the mechanistic implications, if they exist at all. *TC* correlated with aggregate diameter and fluorescence measure of lipid distribution, but these lines were essentially flat given that *TC* does not vary much over the concentrations investigated **(Figure S8).** However, the sudden increase in *TC* at 40% coverage, which is the same concentration that DSPG switches from forming spherical aggregates to forming bilayer patches, is potentially of note. The value of *a* for DSPG is also correlated with aggregate edge preference, though the error bars on *a* indicate that this correlation is unlikely to represent a true causative relationship **(Figure 6A)**.

DOPG exhibited even fewer correlations than did DSPG. A tentative connection exists between contact angle and aggregate edge preference **(Figure 6B)**. Since aggregates on the edge of clay flakes could alter pore space or how the surface traps air, this correlation may actually represent causation. *TC* is correlated with measures of the topography, but these points were present in a tight cluster, so a causative relationship between these factors is unlikely **(Figure S9)**.

The limited changes in PG-montmorillonite film wettability that are observed are mostly correlated to measures of the aggregate distribution on the surface **(see section 3.1.1)**. By contrast, measures of lipid distribution across hundreds of microns had the largest impact on PE-montmorillonite film wettability[44]. Therefore, we conclude that headgroup chemistry not only determines trends in wettability, but the mechanism by which wettability is altered may also change with headgroup chemistry.

Table 5-3: An overview of correlation strength for linear comparisons of PG wetting variables to physical variables. Wetting variables are listed across the top, and physical variables down the side. Refer to **Figures 5-1 and 5-2** for definitions of the physical variables. The cell shading indicates the value of the r^2. Darker colors indicate a higher r^2, and lighter colors indicate a lower r^2. Pairings with and r^2 value > 0.80 are also marked with an X. See **Table S2** for a complete listing of r^2 values.

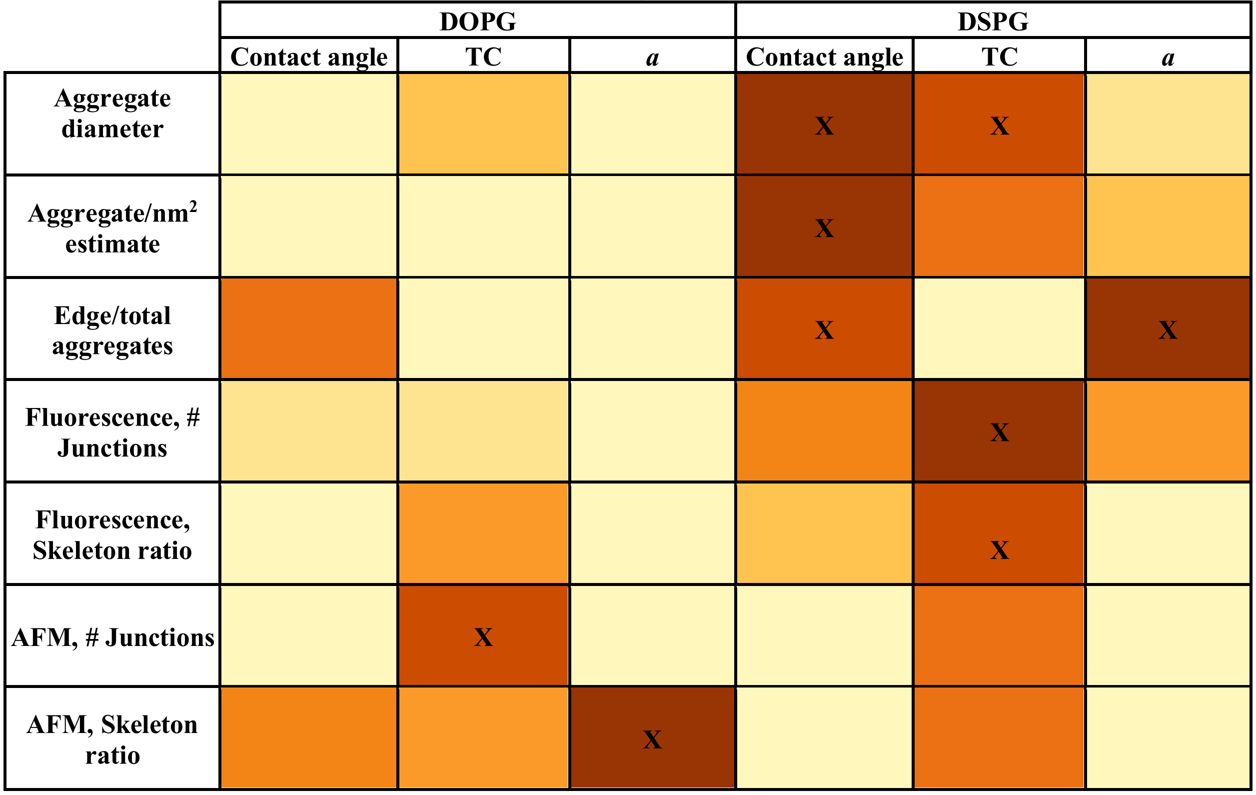

	DOPG			**DSPG**		
	Contact angle	**TC**	***a***	**Contact angle**	**TC**	***a***
Aggregate diameter				X	X	
Aggregate/nm^2 estimate				X		
Edge/total aggregates				X		X
Fluorescence, # Junctions					X	
Fluorescence, Skeleton ratio					X	
AFM, # Junctions		X				
AFM, Skeleton ratio			X			

Summary & Conclusions

Whether and to what degree phospholipids affect montmorillonite wettability depends on both the lipid head and tail chemistry. Overall, melted DSPE caused the largest changes in the measured wettability variables, raising the contact angle, fluid index, and time constant for imbibition. Thus, we hypothesize that in order to change the contact angle, imbibition time constant, and fluid index, a lipid must (1) interact strongly with the clay surface, (2) be solid at room temperature, and (3) be relatively continuously distributed through the film. DSPG meets criteria (2) and (3) but does not bind to the surface, and thus does not alter wettability as drastically as melted DSPE. As soil wettability also depends on whether the soil is wet or dry[50], our results suggest that even in a dry state, PG lipids do not alter wettability.

In the case of PG lipids, which do not bind to the clay surface, there is additionally no relationship between the degree of shear thinning in clays and the time constant of imbibition. For PE lipids, which do bind, there is a positive linear trend for longer time constants and lower shear thinning. PE lipids overall caused greater magnitude changes in *a, TC,* and contact angle. Therefore, we conclude that phospholipids that bind to the clay surface have the most influence on wettability and that influence is maximized when the lipids can be distributed throughout the clay film in a liquid state, but exist in a solid state at the temperature of exposure to water. This latter conclusion highlights the potential role that temperature may play in the development of high SWR due to lipid-soil interactions during wetting and drying cycles. Our results support the use of clay as a method of SWR remediation, given its intrinsic hydrophilicity and resistance to organic-induced hydrophobicity among the molecules studied here.

Acknowledgments

We thank Odeta Qafoku and John Loring (PNNL) for providing processed montmorillonite and Elias Nakouzi (PNNL) for the development of image analysis routines for contact angle measurements. BLK is grateful for lipid expertise, wet lab space, and microscope use through Prof. Sarah Keller and her group at UW. BLK is supported by the National Science Foundation Graduate Research Fellowship Program under Grant No. DGE-1762114. Any opinions, findings, and conclusions or recommendations expressed in this material are those of the author(s) and do not necessarily reflect the views of the National Science Foundation. Sample synthesis, image analysis algorithms, and model development were supported by the US

Department of Energy (DOE), Office of Basic Energy Sciences (BES) Chemical Sciences, Geosciences, and Biosciences Division at Pacific Northwest National Laboratory (PNNL). PNNL is a multiprogram national laboratory operated for DOE by Battelle under Contract No. DE-AC05–76RL01830. This work was facilitated though the use of advanced computational, storage, and networking infrastructure provided by the Hyak supercomputer system at the University of Washington. Atomic force microscopy was conducted at the Molecular Analysis Facility, a National Nanotechnology Coordinated Infrastructure site at the University of Washington which is supported in part by the National Science Foundation (grant NNCI-1542101), the University of Washington, the Molecular Engineering & Sciences Institute, the Clean Energy Institute, and the National Institutes of Health.

Author Information. Corresponding author: James J. De Yoreo, james.deyoreo@pnnl.gov

Supporting Information. Table of wettability data, plots of all contact angle data points, aggregate height and diameter data, PG wettability data on expanded axes, comparison of PG wettability variables, cartoons of lipid surface morphology, additional fluorescence micrographs, table of all R^2 values, linear regression plots for all variables with $R^2 > 0.8$

5.2 SUPPLEMENTARY INFORMATION

S1. Wettability data. All data points for the measured contact angle are presented in **Figure S1**. Note that there could be two populations of contact angle in the montmorillonite film, one at 42° and one at 34°. The 42° population does not exist in the samples with lipid but the 35° population persists. Average wettability data points for each concentration of lipid are presented in **Table S1.**

Table 5-4: (S1) All wettability data for PG samples. Reported errors are standard deviations.

Sample	Lipid Concentration (% CAM)	Contact angle error (°)	Contact angle error (°)	Time constant (s)	Time constant error (s)	Average *a*	*a* error
Montmorillonite	0	37.3	3.5	2.0	0.1	0.016	0.004
DOPG	10	33.6	2.5	2.1	0.2	0.016	0.003
	20	33.3	2.9	2.2	0.2	0.015	0.004
	25	35.7	2.2	2.4	0.2	0.019	0.002
	30	32.6	1.7	2.4	0.2	0.016	0.002
	40	32.3	2.8	2.3	0.2	0.015	0.002
	50	30.3	2.5	2.3	0.2	0.015	0.003
DSPG	10	34.3	2.0	2.1	0.1	0.015	0.002
	20	34.0	1.8	2.3	0.2	0.016	0.001
	25	34.2	1.7	2.2	0.2	0.015	0.003
	30	33.3	1.2	2.1	0.2	0.014	0.004
	40	34.7	1.8	2.4	0.1	0.016	0.005
	50	35.3	1.0	2.3	0.1	0.018	0.003

S2. Addendum to 3.1.1 Lipid Aggregate Behavior. Overall, the fraction of aggregates on edges is always under 30% or over 70%. We speculate that this may be due to aggregate size determining how easily the aggregates could slide between montmorillonite flakes, but plotting the aggregate size versus the edge fraction does not yield any obvious trends **(Figure S2)**. Aggregate heights measured for the DSPG 25% sample are provided in **Figure S2B.** Additional height profiles for the bilayer sheet present in the DSPG 50% sample are provided in **Figure S3**.

S3. TC vs. a. PG wettability variables are plotted on an expanded axis in **Figure S4.** For PG lipids, there is no relationship between *a* and *TC* **(Figure S5)**.

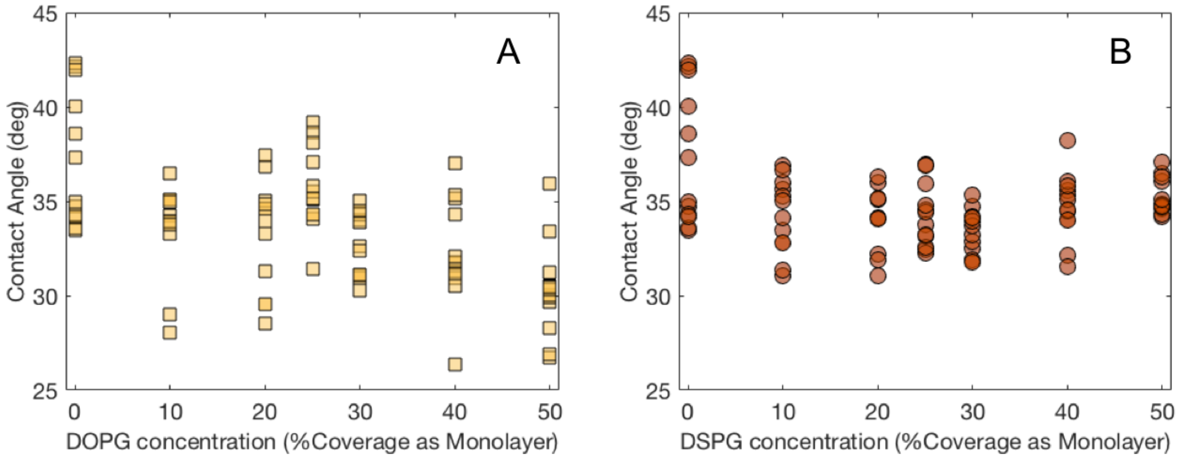

Figure 5-7: (S1) All contact angle data points.

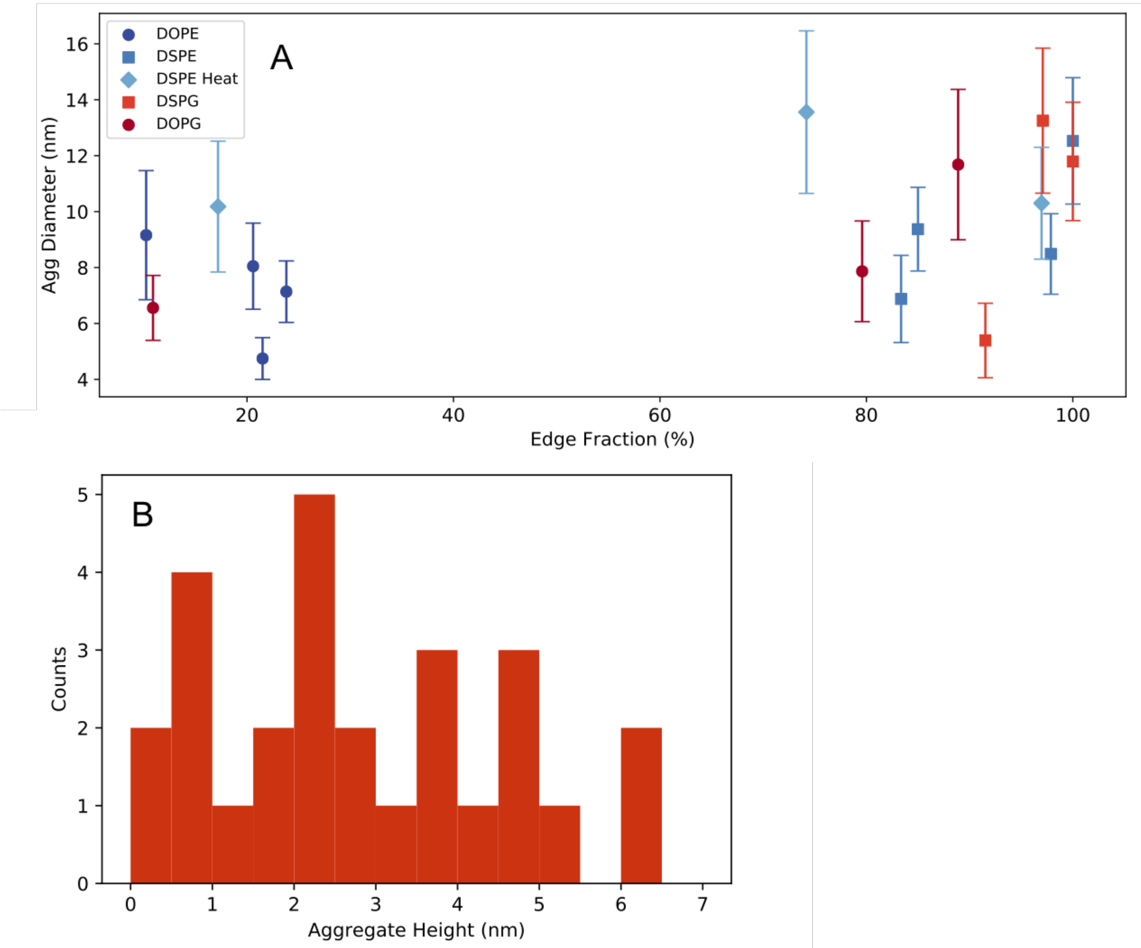

Figure 5-8: (S2) Aggregate characteristics. (A) Aggregate diameter and the fraction of aggregates on clay edge sites are unrelated. (B) Aggregate heights for DSPG at 25% coverage. Mean = 2.8 nm, standard deviation = 1.7 nm. Each bin is 0.5 nm.

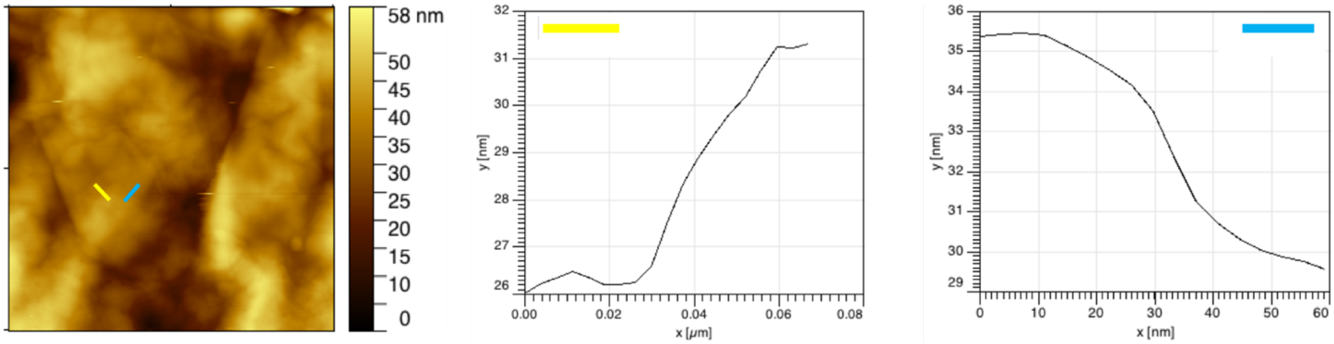

Figure 5-9: (S3) Additional height profiles for the bilayer seen in the DSPG 50% concentration.

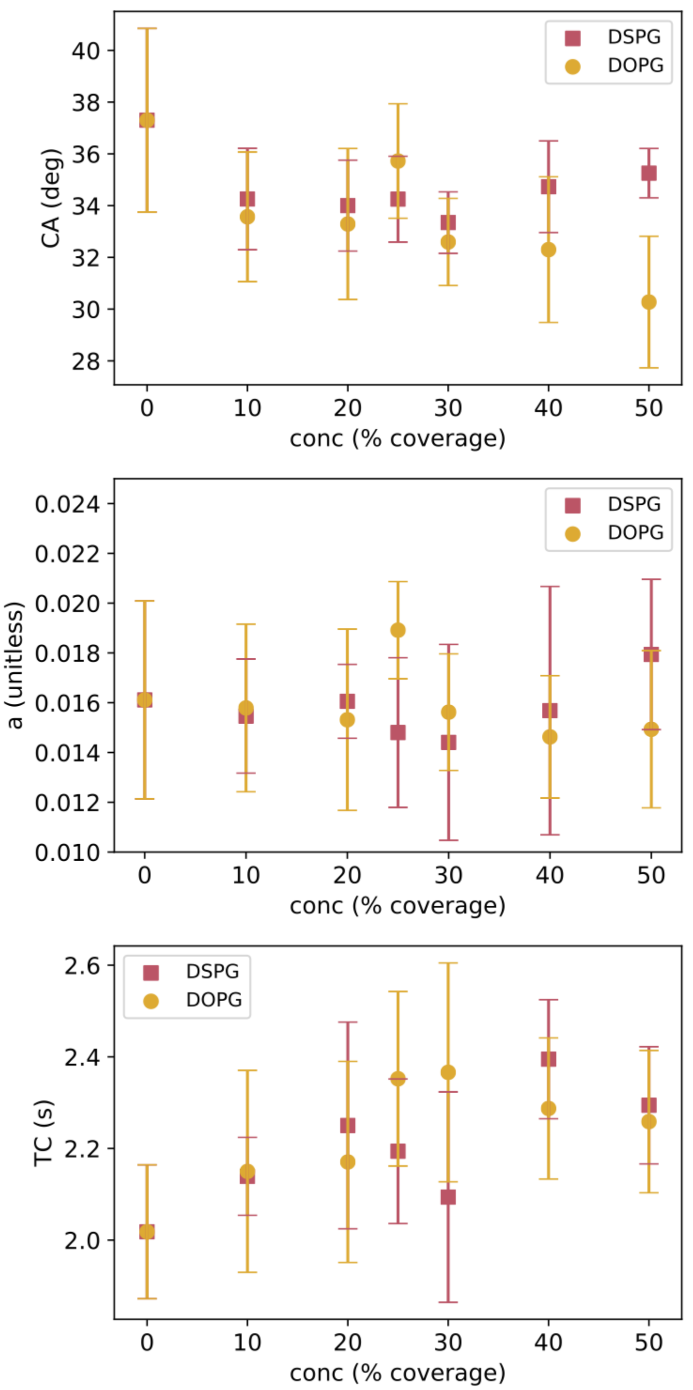

Figure 5-10: (S4) Wettability variables vs. concentration for PG lipids. (A) Contact angle against concentration. (B) Exponent *a* against concentration. (C) The time constant TC (or 1/K in eqn. 2) against concentration. Error bars denote standard deviations.

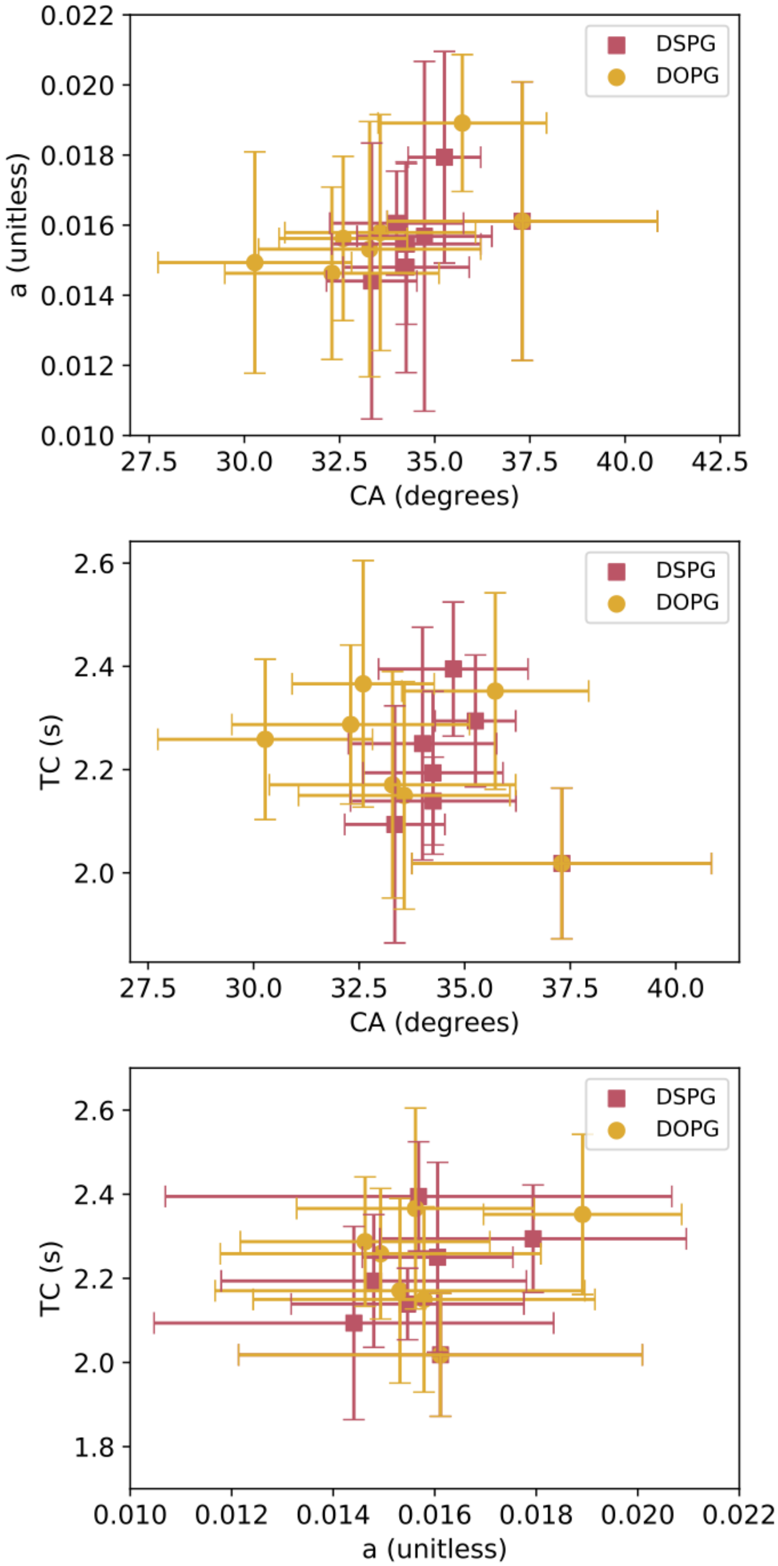

Figure 5-11: (S5) (A) a vs TC for PG lipids. (B) TC vs. CA for PG lipids. (C) CA vs a for PG lipids.

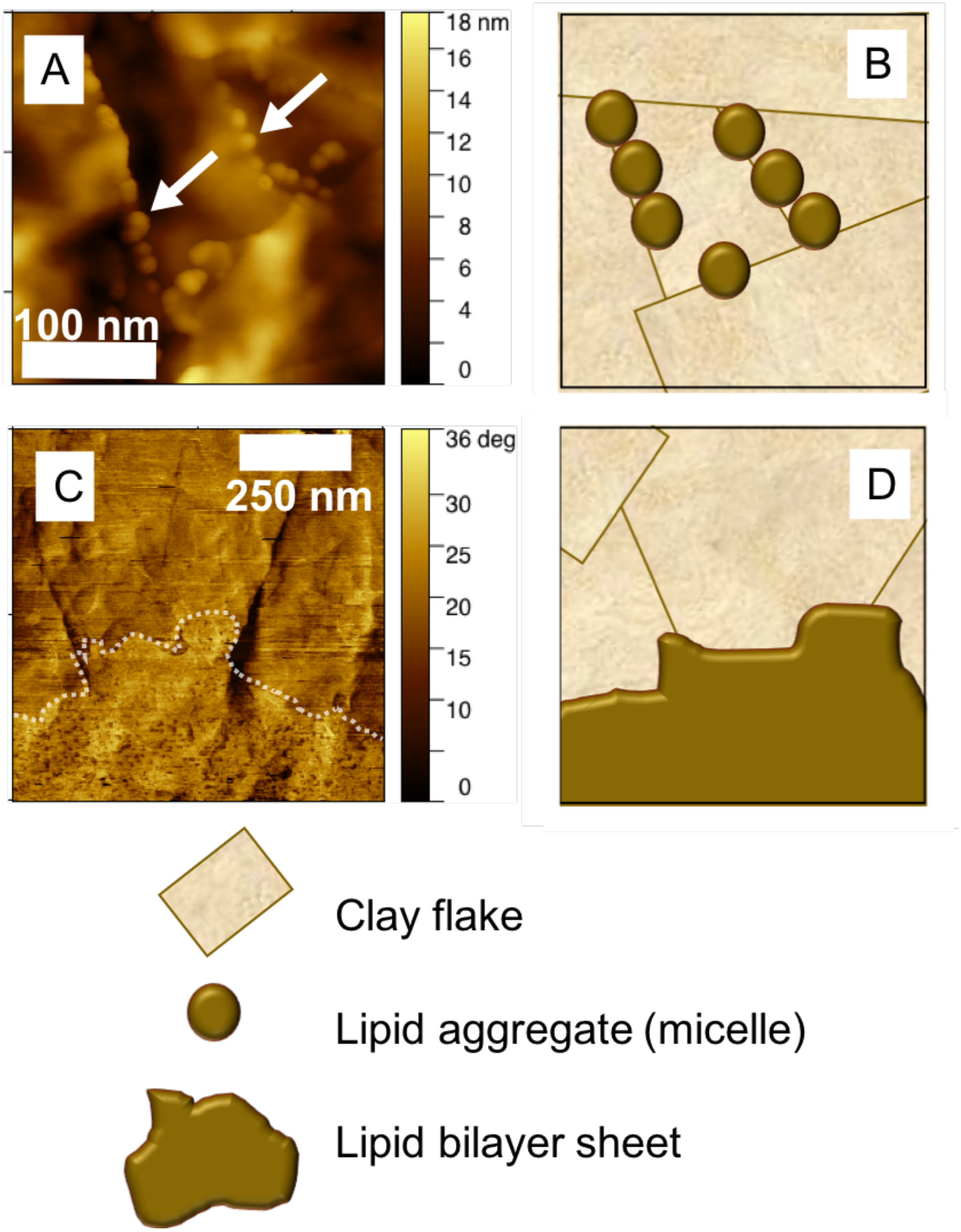

Figure 5-12: (S6) A) AFM topography showing aggregates on the edges of clay flakes. B) A cartoon of the image in (A). C) AFM phase image showing the presence of a lipid bilayer sheet on the clay surface. D) A cartoon of (C).

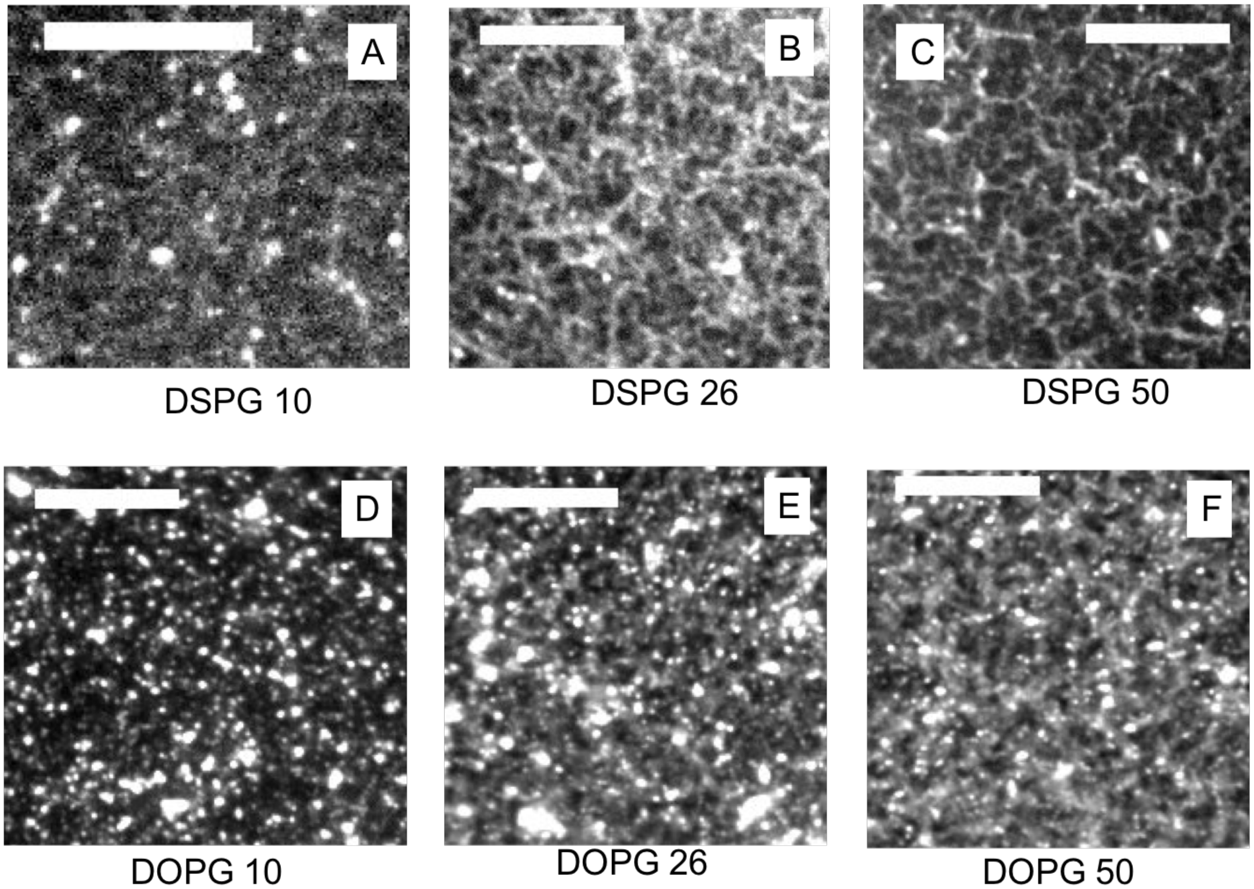

Figure 5-13: (S7) Representative fluorescence micrographs for several coverage values. Scale bars are 50 um. A) DSPG 10% coverage. B) DSPG 25% coverage. C) DSPG 50% coverage. D) DOPG 10% coverage. E) DOPG 26% coverage. F) DOPG 50% coverage.

Table 5-5: (S2) r^2 values for each linear comparison of wetting and physical variables. Larger values are indicated by a darker color. CA = Contact angle.

	DOPG			DSPG		
	CA	TC	*a*	CA	TC	*a*
Avg diameter	0.13	0.56	0.00	0.97	0.85	0.44
Aggregate/nm^2 estimate	0.35	0.30	0.04	0.99	0.79	0.51
edge/total aggregates	0.76	0.02	0.34	0.89	0.36	0.90
Fluorescence 25% Threshold, Junctions	0.20	0.46	0.00	0.07	0.35	0.00
Fluorescence 50% Threshold, Junctions	0.43	0.23	0.07	0.45	0.13	0.64
Fluorescence 75% Threshold, Junctions	0.38	0.27	0.05	0.72	0.96	0.53
Fluorescence 25% Threshold, Skeleton ratio	0.09	0.62	0.02	0.52	0.85	0.33
Fluorescence 50% Threshold, Skeleton ratio	0.18	0.48	0.00	0.48	0.81	0.29
Fluorescence 75% Threshold, Skeleton ratio	0.31	0.34	0.02	0.51	0.84	0.32
AFM 25% Threshold, Junctions	0.06	0.67	0.04	0.36	0.71	0.19
AFM 50% Threshold, Junctions	0.01	0.80	0.11	0.25	0.60	0.10
AFM 75% Threshold, Junctions	0.31	0.34	0.02	0.29	0.64	0.13
AFM 25% Threshold, Skeleton ratio	0.38	0.27	0.05	0.39	0.74	0.21
AFM 50% Threshold, Skeleton ratio	0.70	0.65	0.98	0.29	0.64	0.13
AFM 75% Threshold, Skeleton ratio	0.14	0.54	0.002	0.30	0.65	0.14

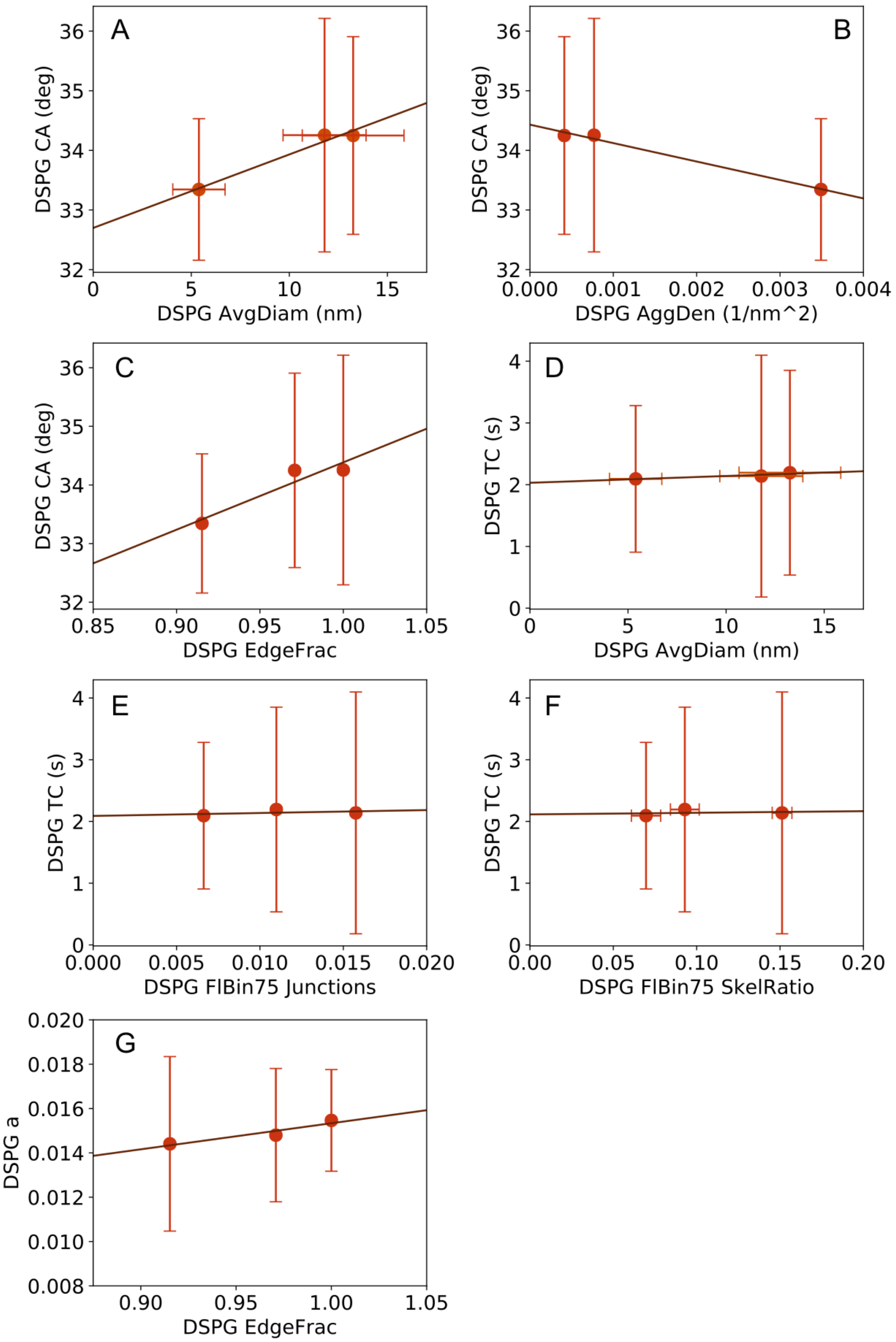

Figure 5-14: (S8) DSPG correlation plots for which $r^2 > 0.8$. Note large error bars and flat *a* values. (A) DSPG aggregate size vs. CA. (B) DSPG aggregate density vs CA. (C) DSPG DSPG aggregate edge fraction vs. CA. (D) DSPG aggregate size vs. TC. (E) DSPG junction density (fluorescence) vs. TC. Junction density is reported as the number of junction pixels per square micron. (F) DSPG skeleton ratio (fluorescence) vs. TC. (G) DSPG aggregate edge fraction vs. *a*.

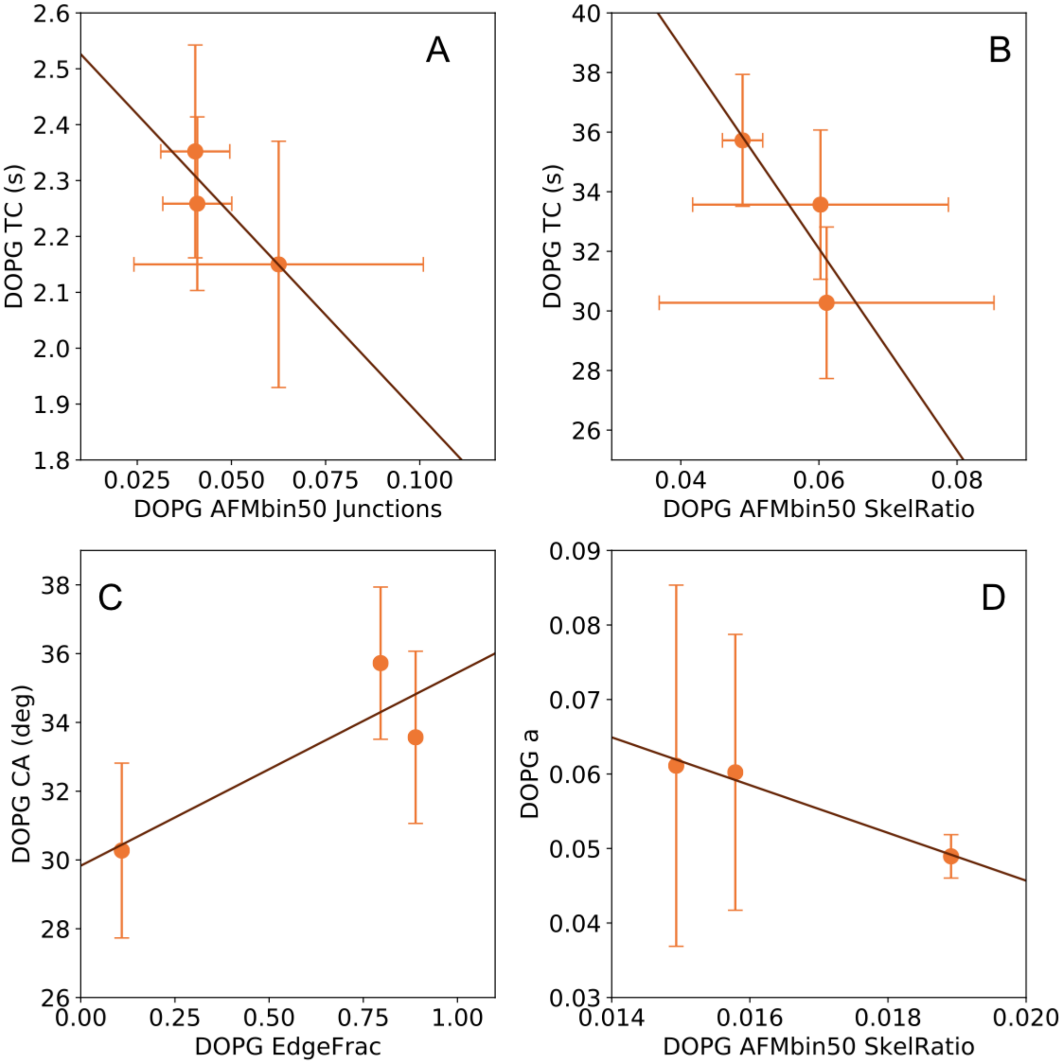

Figure 5-15: (S9) : All DOPG correlation plots for which $r^2 > 0.7$. (A) DOPG junction density, fluorescence, vs CA. (B) DOPG skeleton ratio, fluorescence, vs TC. (C) DOPG fraction of aggregates on edges vs CA. (D) DOPG skeleton ratio, AFM, vs. *a*.

Chapter 6. STRUCTURES OF DRIED FATTY ACIDS

6.1 INTRODUCTION

Life on Earth requires several features: cells are bound by membranes and rely on proteins and DNA/RNA to function and reproduce. A major area of inquiry is how these components (membranes and biopolymers) initially came together. Did membranes, proteins, and RNA form separately and then combine, or did membranes and polymers develop together? The latter scenario, wherein monomers initially attached to primitive membranes, thereby strengthening the membranes, while the membranes brought the monomers into close contact and thus allowed them to polymerize[57], offers a potential answer to the question of how life's components initially combined.

Dehydration can drive the condensation reactions that produce biopolymers[58]. In addition, confinement of amino acids or nucleotides in between dried bilayers during repeated wetting/drying cycles has been suggested as a mechanism that enhances biopolymer formation[59]. Drying nucleotides with phospholipids[60] or salt crystals[61] has been shown to increase RNA polymerization yield. Polymerization enhancement most likely results from trapping nucleotides between dehydrated phospholipid bilayers[62,63,64], as confinement generally increases the polymerization of monomers[65] and the lipid matrix may favorably align them[64].

Modern phospholipids readily form bilayers. However, phospholipids are made by cells; the prebiotic analogs to modern phospholipids are simple fatty acids[66,67]. Fatty acids form membranes which are much more fragile than those made by phospholipids[68]. In this study, I investigate if fatty acid vesicles form dried bilayer stacks as phospholipids do, and if this increases the yield of polymerization reactions.

Decanoic acid was chosen for this study because it forms vesicles in solution, much like modern phospholipids, and it is a prebiotically-plausible amphiphilic molecule. Heptanoic acid and benzoic acid were chosen as control amphiphiles. With a tail of only seven carbons, heptanoic acid is not expected to form membranes in solution[69].

6.2 METHODOLOGY

6.2.1 *Experimental details*

Decanoic acid, serine, alanine, and serine ethyl ester was obtained from Nu-Chek Prep, Elysian, MN. 0.18 M stock decanoic acid was prepared by dissolving decanoic acid in 0.19 M NaOH with gentle heating. Because the stock pH is basic, micelles were present in this solution. Vesicles were made freshly for each experiment by diluting the stock solution to 50 mM and titrating to a pH of 6.8 with HCl. For experiments with added amino acid, an aqueous solution of serine, alanine, or alanine ethyl ester was added to the decanoic acid solution. DOPC was acquired from Avanti Polar Lipids; DOPC vesicles were made by gentle hydration (see also section **3.1**).

Samples were prepared by placing a 3 μL droplet of vortexed solution on a freshly-cleaved mica substrate. Droplets were allowed to dry for 1-2 hours before imaging.

All AFM imagery was acquired in air on an Asylum Cypher ES with AC240TS cantilevers (tapping mode).

6.2.2 *Molecular packing theory calculations*

To provide rationalization for the structures seen in the AFM images, I calculated the molecular packing parameter for a range of fatty acids. Molecular packing theory provides a prediction for how amphiphiles self-assemble in water based on the relative size of the hydrophilic and hydrophobic parts of the molecule[70]. The packing parameter is defined as:

$$P = \frac{V}{l * a} \qquad \text{6.1: Packing parameter}$$

where P is the packing parameter, V is the volume of the molecule's hydrophobic moiety, l is the length of the hydrophobic moiety, and a is the polar head-group's cross-sectional area. Based on the value of P, different morphologies are expected. For $P<0.33$, spherical micelles are predicted; for $0.33<P<0.5$, fibers ("wormlike" or cylindrical micelles); for $0.5<P<0.7$, vesicles; for $0.7<P<1$, tubes with bilayer walls; and for $P=1$, bilayer membrane sheets.

Calculation of P is complex due to the lack of experimental data available on head group areas and the presence of different methods of determining V. It can provide insight into trends even if it does not yield quantitative predictions.

I estimated the length of the hydrophobic moiety in Angstroms based off of work done at Norgwyn Software[71].

$$l = 1.5 + 1.265 * c \qquad \text{6.2: Tail length}$$

where c is the number of carbons minus one in the hydrophobic backbone, and 1.5 Å is added to account for the hydrogens at the end of the carbon chain. Decanoic acid has 10 total carbons and $c = 9$.

In order to estimate the cross-sectional area of the head groups, I used the literature value for stearic acid (18-carbon fatty acid), which is 20 Å^2 per molecule[72]. Generally speaking, the area per molecule is *larger* for *smaller* molecules because they have weaker van der Waals interactions with each other. The area per molecule will also increase with pH, as head groups deprotonate and are electrostatically repulsed from each other. However, because shorter-chain fatty acids are too water soluble to obtain accurate data on area-per-molecule from Langmuir trough isotherms, the areas I use in this section must be regarded as estimations only.

I calculated the hydrophobic moiety volume from the van der Waals volume of alkanes. Zhao et al.[73] calculate a van der Waals volume of 164 Å^3 for nonane. Each carbon therefore has a volume of about 18 Å^3; this volume can be multiplied by the number of carbons in the hydrophobic tail in order to obtain V.

6.3 RESULTS

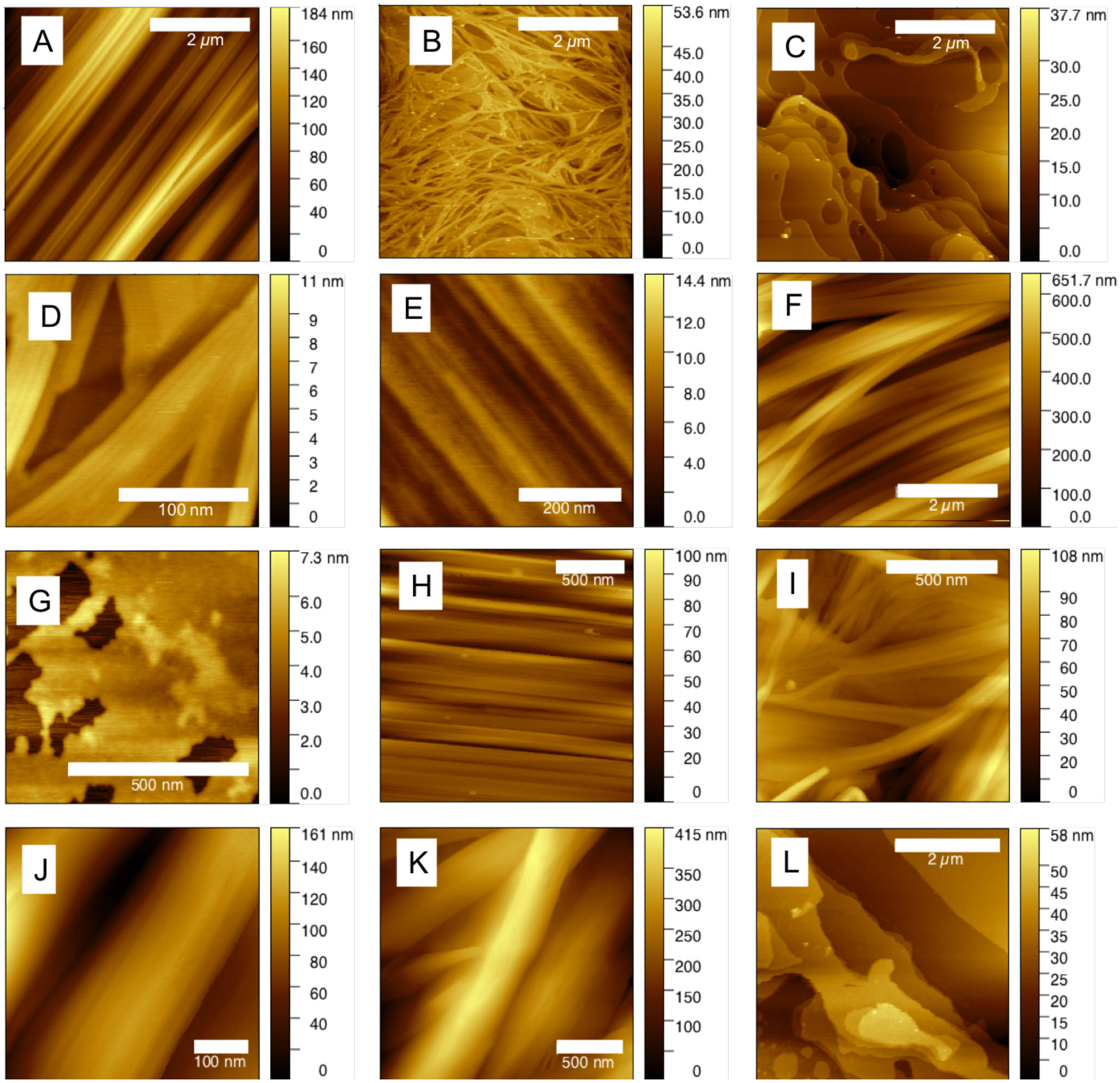

Figure 6-1: Dried structures of: A) Decanoic acid micelles. B-D) Decanoic acid vesicles. E,F) Heptanoic acid, pH 7.5. G) Heptanoic acid, pH 10. H,I) Heptanoic acid, pH 6. J,K) Benzoic acid. L) DOPC. Section 6.5 contains additional images.

6.3.1 *Structures of fatty acids and a phospholipid*

AFM images for all molecules and pH values tested are presented in **Figure 6-1.** In general, dried fatty acids form long ribbons which are composed of smaller ribbons between 3 and 8 nm in diameter **(Figure 6-2** and **Section 6.5)**, with 6 nm being typical. I hypothesize that these constituent ribbons are most likely cylindrical micelles. That they are wider than two decanoic acid molecules laid end-to-end is likely because they flatten upon drying. Conventional AFM did not produce sufficiently clear images, so it is not clear if these structures are present in solution, or if they form during the drying process. It is possible that high-speed AFM could be used to observe these molecules assemble in a liquid environment.

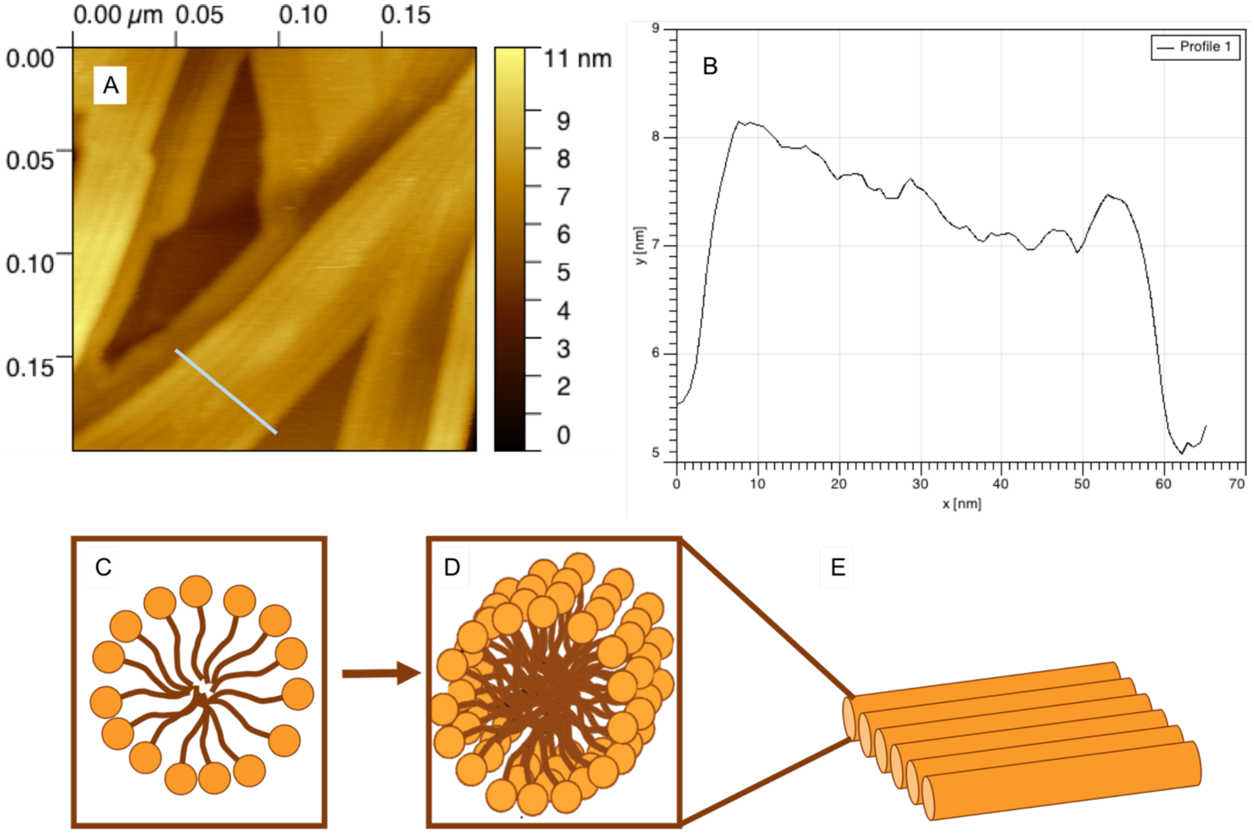

Figure 6-2: Vertical profile of a "ribbon" resulting when a solution of decanoic acid vesicles were dried. The proposed structure is diagrammed in C,D,E. C) Cross-section of a cylindrical micelle (D). E) Many cylindrical micelles lined up could make up the larger "ribbon" structure.

DOPC forms sheet-like structures which we interpret as stacks of bilayers (**Figure 1 L**).

Within the fatty acid samples, bilayers form definitively from dried decanoic acid and may form from dried heptanoic acid under very basic conditions. Specifically, roughly half of the sampled areas of dried decanoic acid vesicles contained flat terraces characteristic of bilayers **(Figure 6-1C)**. Heptanoic acid at pH 10 dries into areas of flat, soft material; the consistency of its height suggests a bilayer or monolayer may form under these circumstances. However, heptanoic acid rarely forms the multi-stack terraces found in the decanoic acid vesicles and DOPC samples.

6.3.2 *Decanoic acid mixed with other molecules*

Mixing decanoic acid with other molecules, whether amino acids or buffer, disrupts the structures seen in **Figure 6-1**. HEPES buffer is particularly disruptive, as it prevents formation of bilayers when decanoic acid vesicles dry out **(Figure 6-3G, H** and **Figure 6-10)**. **Figure 6-3G** may at first glance appear to be bilayer structures, but the "flat" areas are actually made of the cylindrical micelle structures **(Figure 6-4).**

For the ribbon morphology, amino acids tend to lead to shorter or interrupted ribbons **(Figure 6-3A,B).** For the bilayer morphology, amino acids cause the formation of nodules on the edges of the bilayer sheets **(Figure 6-3C,E).** The addition of alanine ethyl ester to decanoic acid leads to the formation of crystals **(Figure 6-3I, Figure 6-9).**

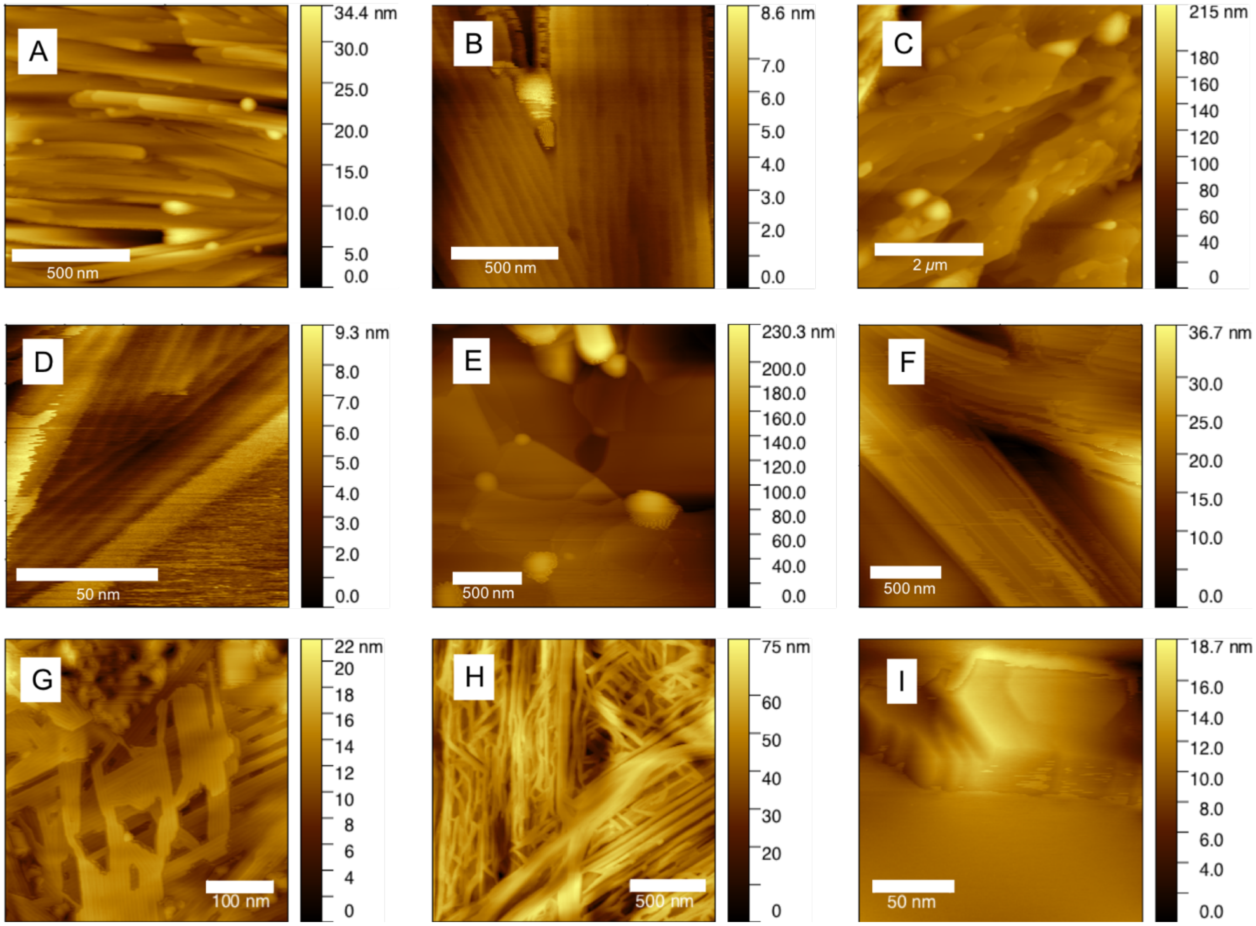

Figure 6-3: Dried structures of: A,B) DA micelles and serine. C,D) DA vesicles + serine. E,F) DA Vesicles and alanine. G,H) DA vesicles and HEPES. I) DA and alanine ethyl ester.

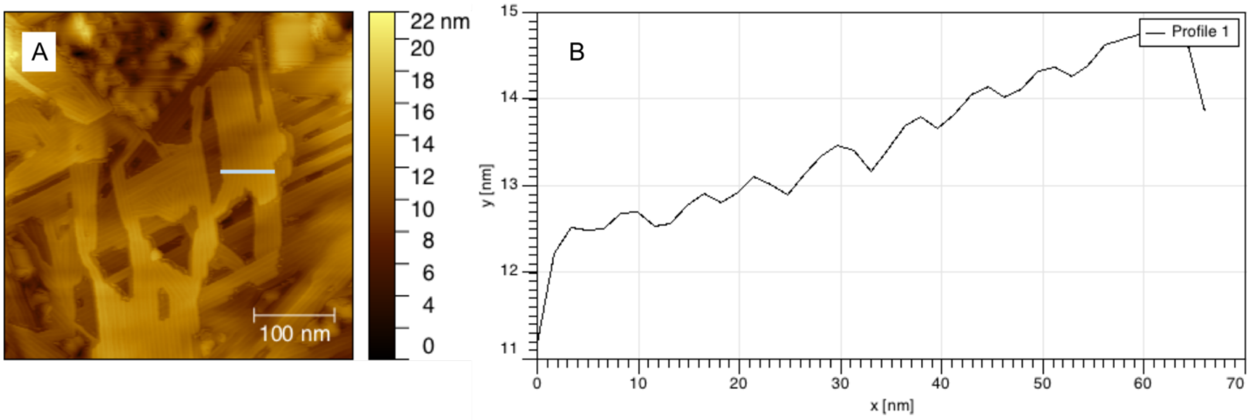

Figure 6-4: Vertical profile of a "flat" surface in the DA/HEPES dried system. The wormlike micelles (A) are roughly 6 nm in diameter (B).

6.3.3 *Non-lipid structures*

Serine and alanine ethyl ester both crystallize out of aqueous solutions **(Figure 6-5).** Some amorphous structures also occur **(Figure 6-5B),** but these molecules do not produce the same ribbon-like or bilayer structures that the lipids do.

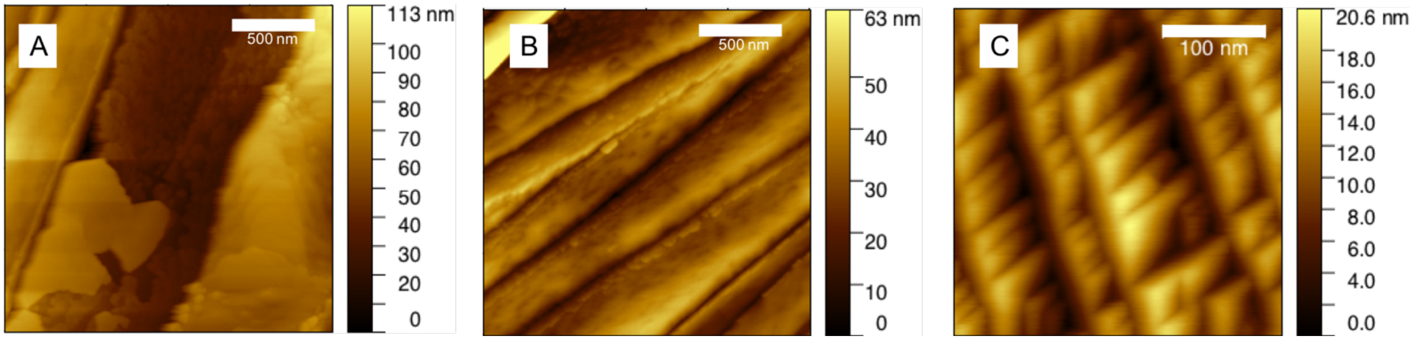

Figure 6-5: A,B) Serine alone. C) Alanine ethyl ester.

6.3.4 *Molecular packing theory results*

I assumed that in the pH range of decanoic acid vesicle formation, $a = 20$ Å^2, V = 9 carbons*18 Å^3/carbon = 162 Å^3, and $l = 12.9$ Å. This produced P = 0.62, which is in the vesicle range.

I have plotted the change in packing parameter over a range of areas per molecule **(Figure 6-6)**. For a headgroup area of approximately 18-28 Å^2, vesicles are expected, with the length of the carbon tail having a slight influence on this range. Assuming an increase in pH, the area per molecule would also increase as the headgroups pick up charge and repel each other, and for areas larger than 28 Å^2 1D fibers or micelles (if a > 28 Å^2) are expected. It is interesting that there is a range of areas that would produce 1D fibers, which are the same morphology I observe in the AFM images of dried fatty acids.

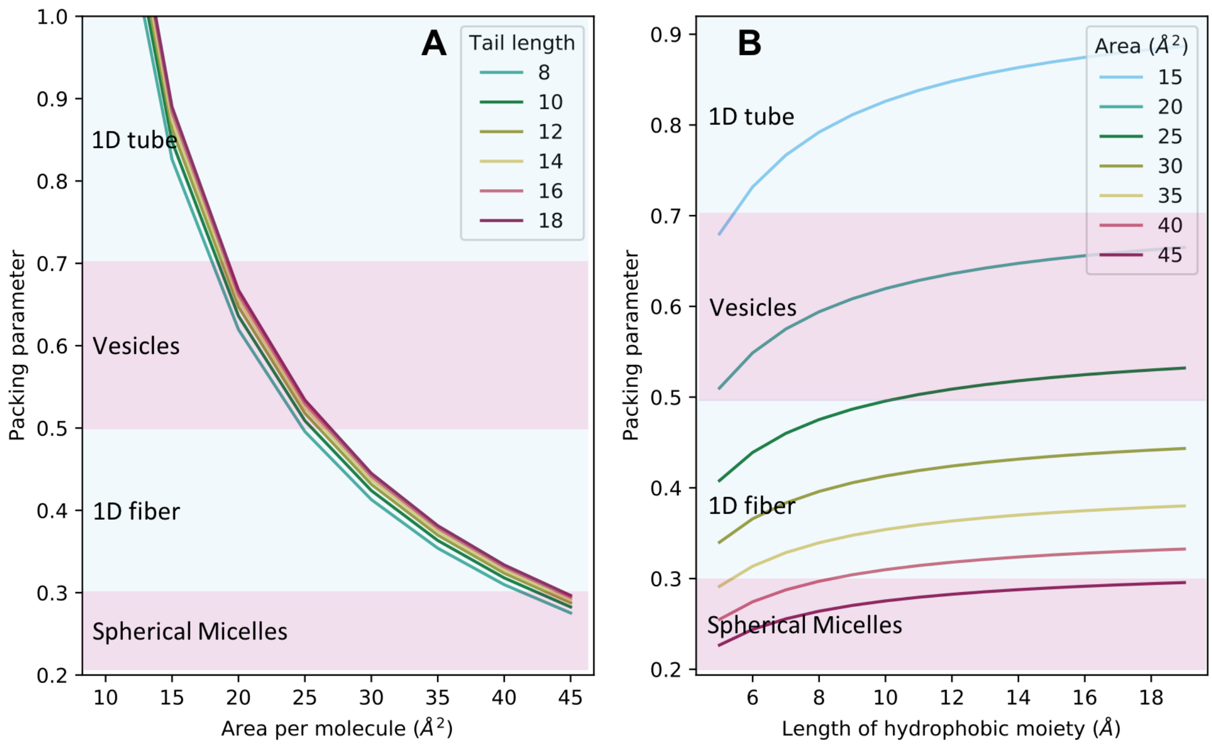

Figure 6-6: Molecular packing theory results. A) Varying the number of carbons in the tail group has a limited effect on the predicted packing of fatty acids. B) Varying the head group's cross-sectional area has a dramatic effect on the packing parameter. Note that some combinations of tail lengths and areas are unlikely to occur naturally. Vesicles are most likely when the fatty acid head group has an area near 20 Å^2.

Figure 6-6 provides a qualitative trend of how the head group area might alter packing. This model suggests that to make vesicles, certain areas and tail lengths are favored – especially areas in the range of 15-25 Å^2. Since the head group area is expected to vary with the length of the molecule, some of the presented combinations of areas and tail lengths most likely never occur in nature. Nonetheless, these plots provide some idea of what areas and lengths are most likely to assemble into vesicles.

Table 6-1: Summary of molecular packing theory results and comparison to experimentally known morphologies. I assumed that decanoic acid's *a* approximately doubles when deprotonated, and that heptanoic acid's *a* is larger than decanoic acid's due to its smaller size.

Molecule	***a* ($Å^2$, estimate)**	***P***	**Predicted Morphology**	**Observed Morphology**
Decanoic acid	20 (acidic)	0.6	Vesicles	Vesicles
Decanoic acid	40 (basic)	0.3	1D fibers/spherical micelles	Micelles
Heptanoic acid	30	0.4	1D fibers	Unknown, most likely micelles

6.4 DISCUSSION AND CONCLUSIONS

I find that dried phospholipid (in this case, DOPC) forms bilayers on the substrate when dried. Decanoic acid is capable of forming bilayers like those formed by phospholipids, but this only occurs when decanoic acid *vesicles* are dried, and the bilayers are not as widespread as they are in phospholipid samples. Decanoic acid *micelles*, heptanoic acid, and benzoic acid do not form bilayer structures, only a ribbon-like morphology which is composed of cylindrical micelles. I therefore conclude that dried bilayers only occur when the original solution contained vesicles.

With the caveat that the molecular packing theory calculations contain many assumptions, the calculated packing parameters support the idea that the ribbon-like morphology in the AFM images represent wormlike/cylindrical micelles, as they would have dried out from a solution of cylindrical micelles. This provides some theoretical backing to the hypothesis that vesicles must be present in solution in order for the fatty acid to form bilayers when dried.

These results will need to be compared to mass spectrometry data currently being acquired in order to determine if polymerization is affected by the dried fatty acid morphology.

6.5 ADDITIONAL IMAGES

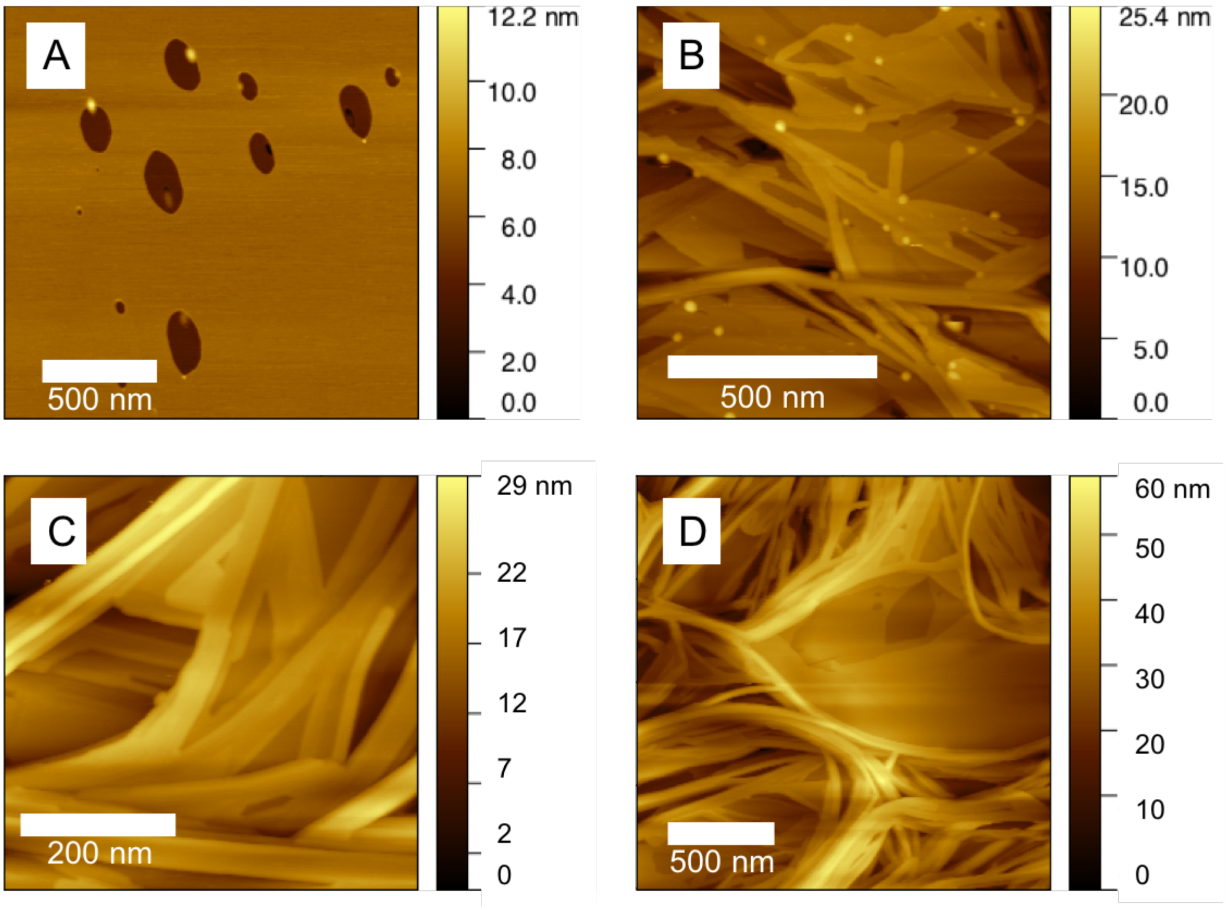

Figure 6-7: Additional dried decanoic acid vesicle images. A) Bilayer-height holes in a flat sheet of decanoic acid. B, C, D) Mixed morphology with some ribbon-like features and some bilayer sheets.

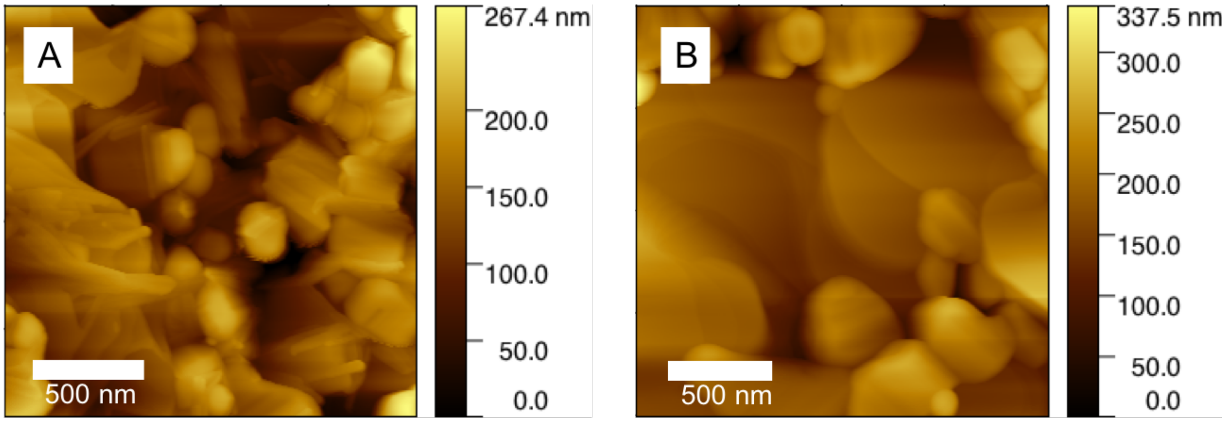

Figure 6-8: Decanoic acid vesicles and alanine. A) Mixed chunky morphology and bilayers. B) Larger chunks and bilayer sheets.

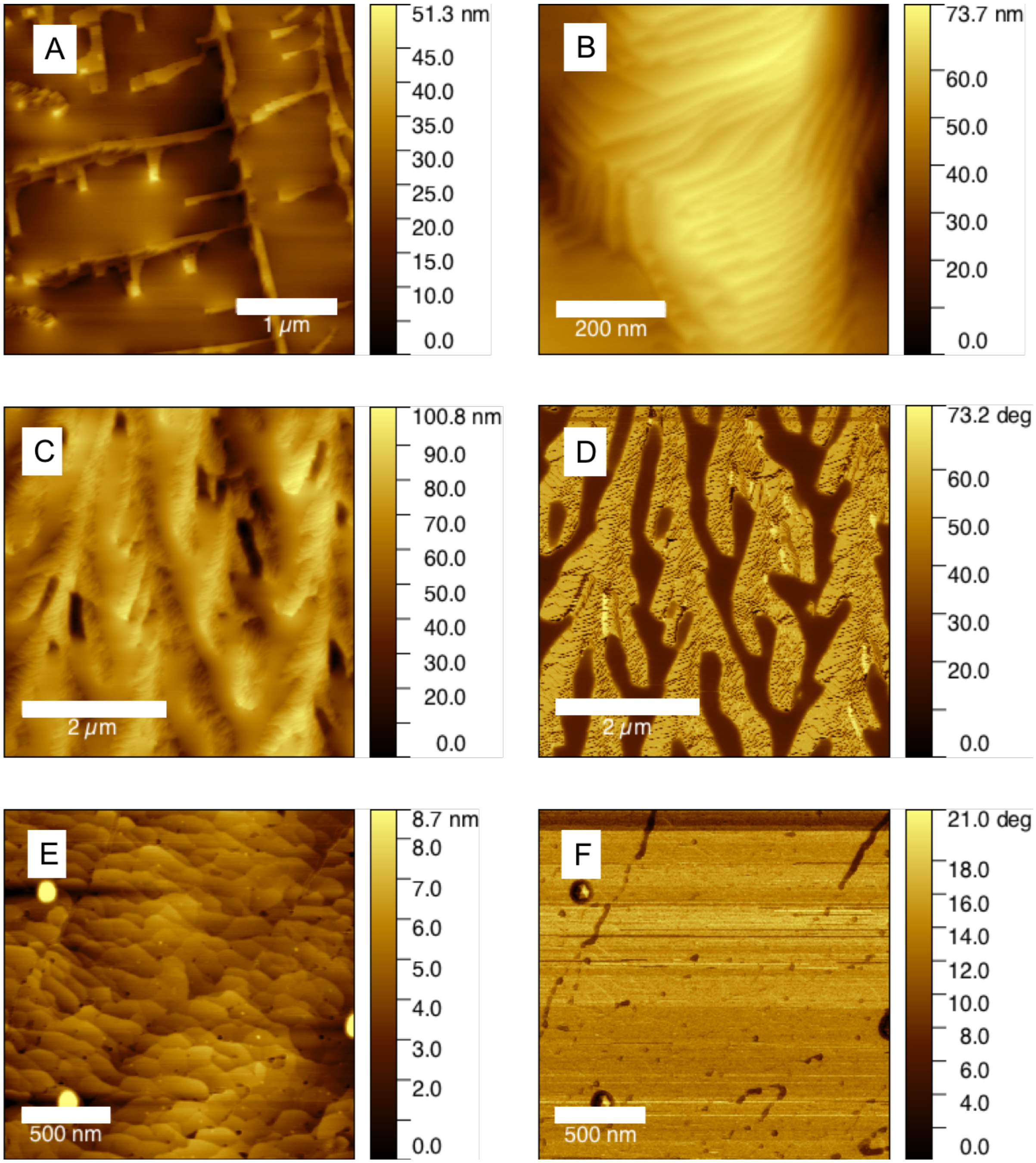

Figure 6-9: Decanoic acid and alanine ethyl ester. A) Crystal morphology. B) A close-up of the ribbed structures seen in (C), which shows a mix of smooth and lumpy textures. D) The corresponding phase image of (C). The two textures appear as different phases, which suggests that their material properties are different. The branching pattern is likely due to a growth instability during crystal growth. E) Fish-scale-like morphology, perhaps due to crystal growth with impurities. F) Phase image for (E).

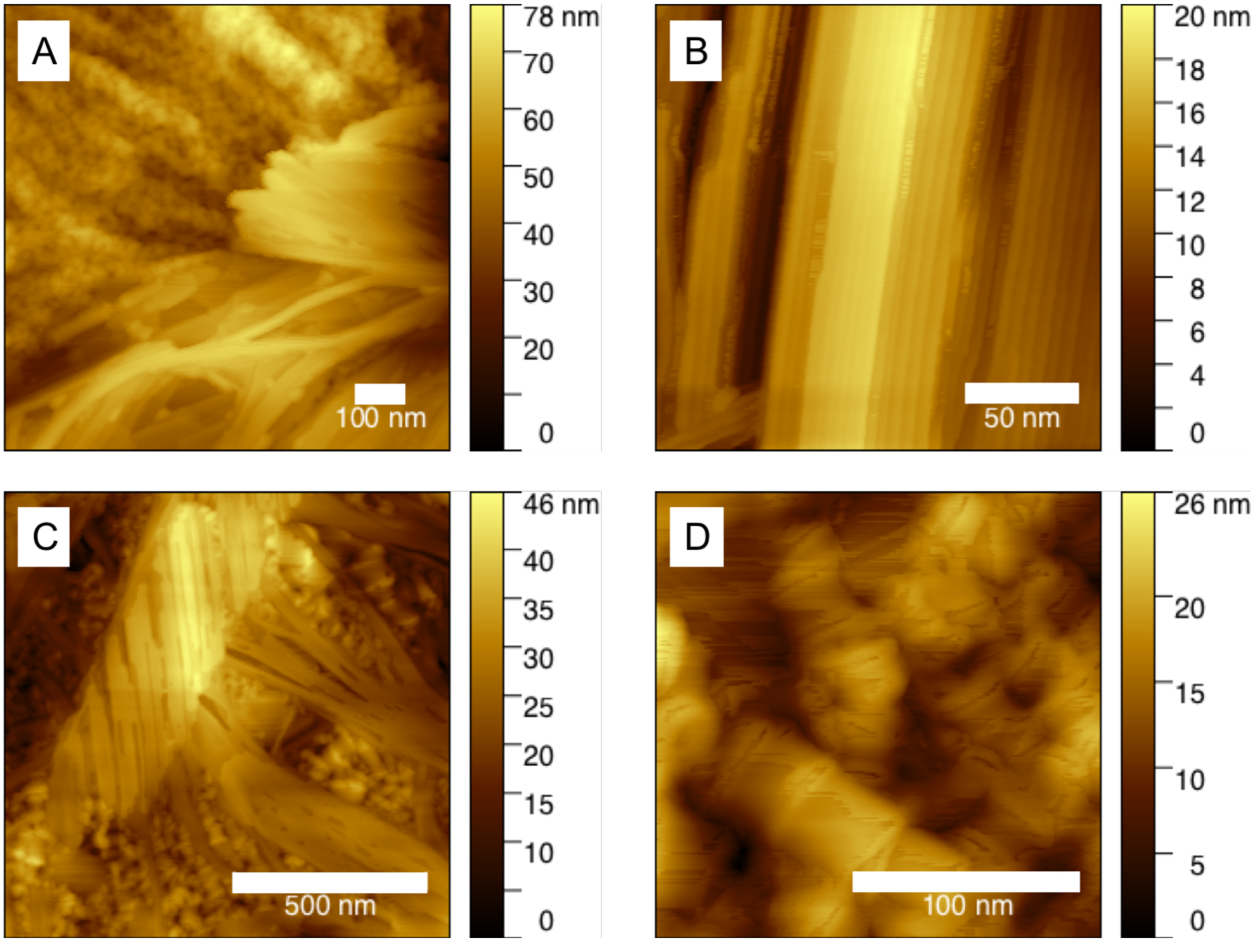

Figure 6-10: Decanoic acid and HEPES. A) Regions of lumpy morphology adjacent to ribbon morphology. B) Ribbon morphology with 6 nm diameters. C) Mixed lumpy and ribbon morphologies. D) Up-close image of the lumpy morphology.

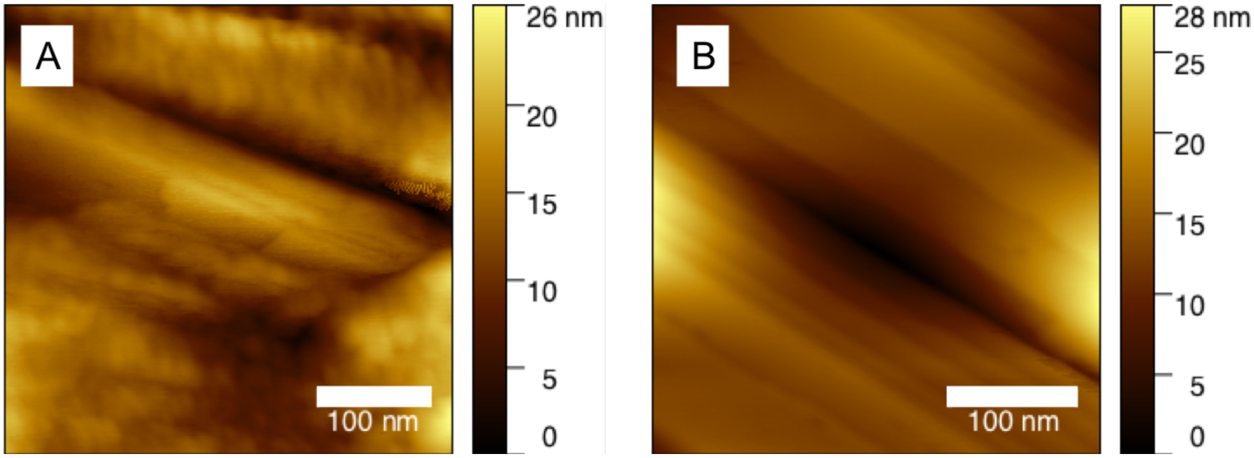

Figure 6-11: Benzoic acid. A) Lumpy morphology, perhaps similar to the “fish scale” morphology in Figure 6-8E. B) Possible ribbon morphology; imaging conditions were not sufficient to capture micelle-level detail.

Chapter 7. PC LIPIDS, SOLVENT EFFECTS, AND HIGH LIPID COVERAGE

7.1 PC LIPIDS

In addition to the PE and PG lipids discussed in Chapters 4-5 of this thesis, I collected data on phosphocholine (PC) lipids. PC lipids are zwitterionic, like PE, but have a bulkier headgroup. These data are included below for completeness and to assist others who may choose to pursue these systems.

7.1.1 *PC aggregates on the montmorillonite film surface*

PC forms nanoscale, circular aggregates on the montmorillonite film surface, like the other lipids studied **(Figure 7-1)**. The morphology of the DPPC aggregates was difficult to determine, as I found the sixteen-carbon lipids were difficult to image clearly **(Figure 7-1A-C).**

PC lipids also bind to the montmorillonite surface in solution **(Figure 7-2)**. This is expected based on the zwitterionic head-group charge at ambient pH, and matches the behavior of PE lipids.

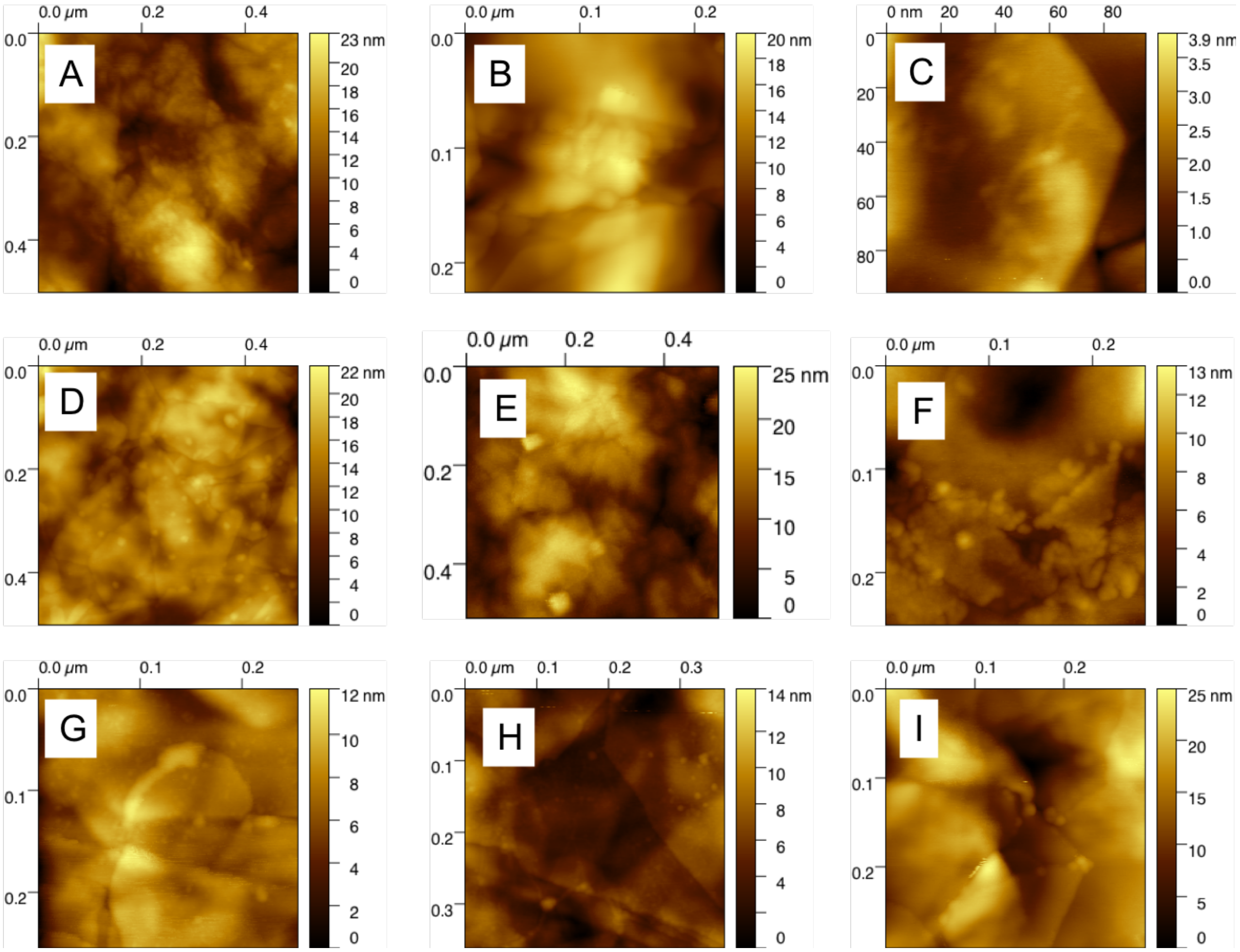

Figure 7-1: PC lipids on montmorillonite. A) DPPC, 10% coverage. B) DPPC, 25% coverage. C) DPPC, 50% coverage. D) DOPC, 10% coverage. E) DOPC, 25% coverage. F) DOPC, 50% coverage. G) DSPC, 10% coverage. H) DSPC, 25% coverage. I) DSPC, 50% coverage.

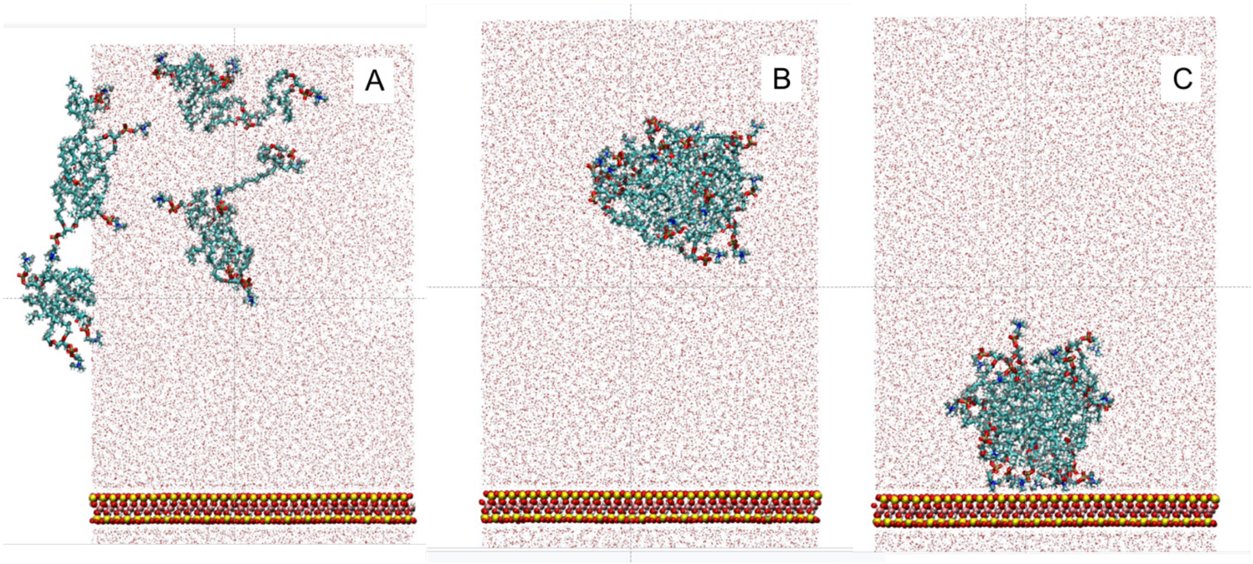

Figure 7-2: Unbiased molecular dynamics simulation of DOPC and a montmorillonite surface. (A)-(B) First, the lipid forms a micelle in solution. (C) The micelle then interacts with the montmorillonite surface and remains stable there for the remainder of the simulation. Simulations were run by Dr. Nihit Pokhrel.

7.1.2 *DOPC on a flat mica surface*

The substrate's surface roughness influences how DOPC arranges. On irregular clay films, DOPC readily forms the circular aggregates described above **(Figure 7-1D,E,F)**. However, on a flat mica surface, DOPC instead forms flat bilayers or multilayer sheets upon drying **(Figure 7-3)**.

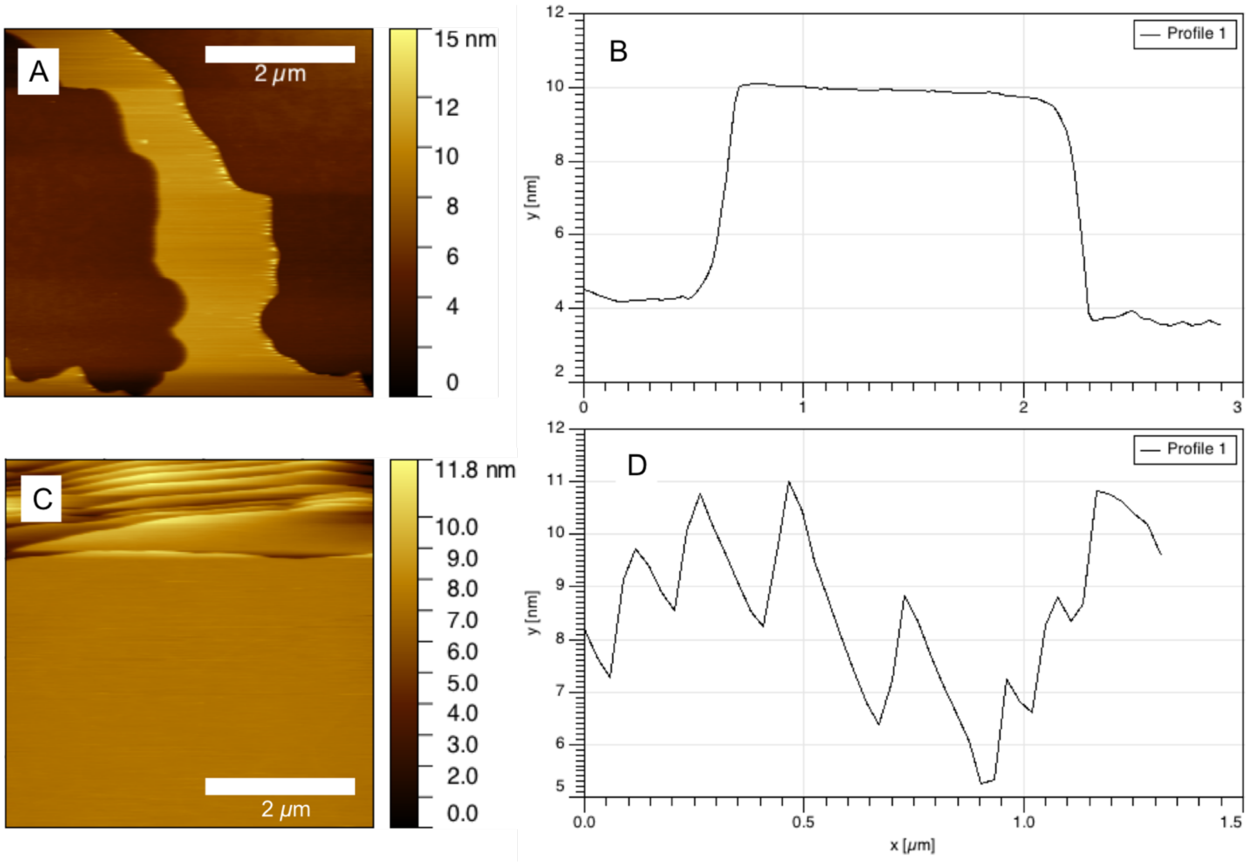

Figure 7-3: DOPC on mica. A) An isolated bilayer. B) The height profile of the isolated bilayer in A. C) A "pancake stack" of bilayers with the height profile of the stair-steps (D).

7.1.3 *PC fluorescence*

The PCs are distributed through the film at all concentrations tested **(Figure 7-4)**. Even DSPC, with a melting temperature of 55 °C, is distributed through the film. This matches with DSPG behavior (T_{melt} = 55 °C). Therefore, DSPE (T_{melt} = 74 °C) is the only lipid out of all the PE, PG, and PC lipids that is not distributed through the film. It is possible that if lipids with melting temperatures between 55 °C and 74 °C were imaged, one could identify a characteristic T_{melt} that corresponds with a switch from being distributed through the film to being present only in patches, or perhaps find a gradual transition with a mix of distributed lipid and lipid patches over some range of temperature between 55 °C and 74 °C.

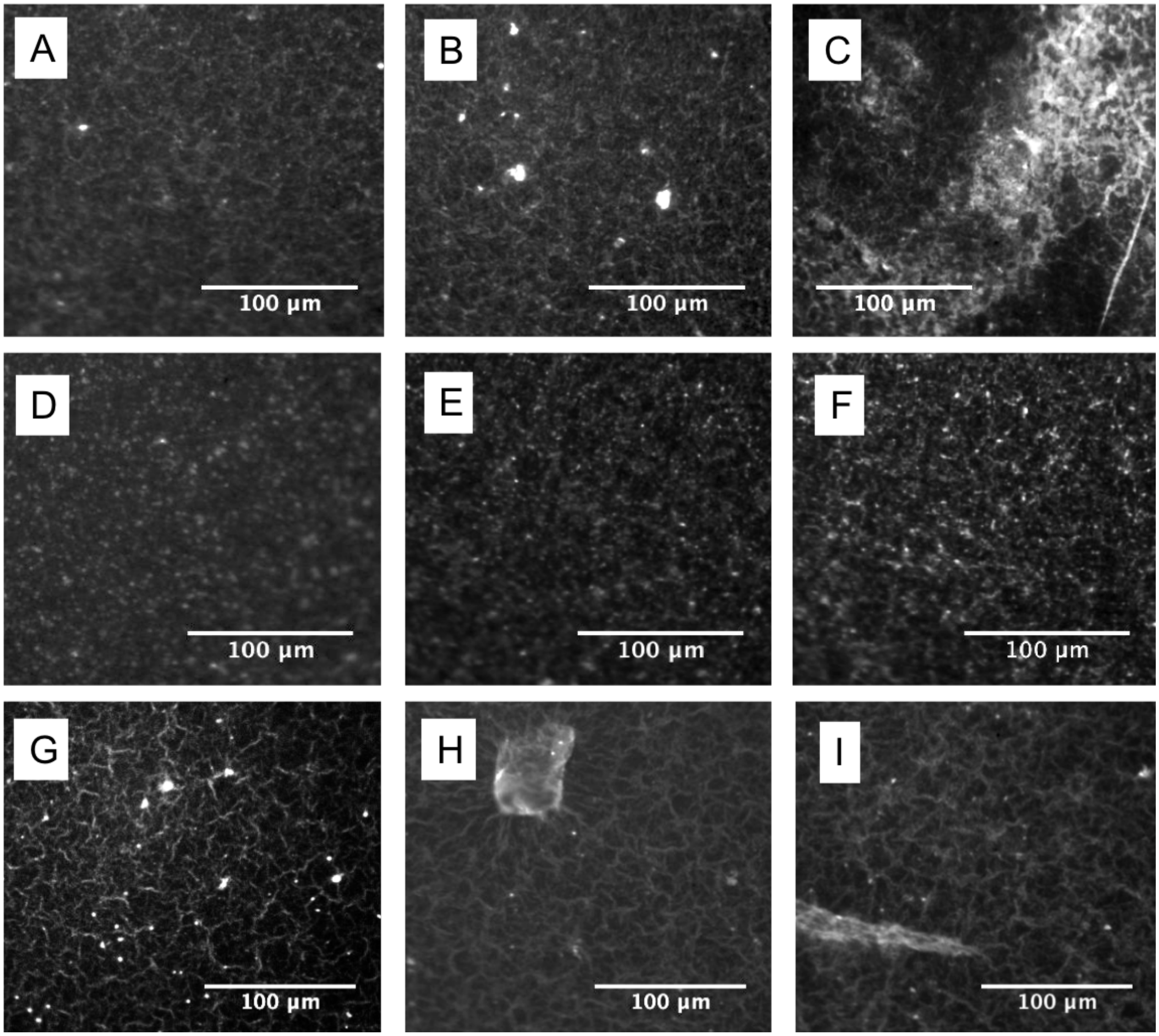

Figure 7-4: Fluorescence micrographs showing the distribution of PC lipids throughout montmorillonite films. A) DPPC, 10% coverage. B) DPPC, 25% coverage. C) DPPC, 50% coverage. D) DOPC, 10% coverage. E) DOPC, 25% coverage. F) DOPC, 50% coverage. G) DSPC, 10% coverage. H) DSPC, 25% coverage. I) DSPC, 50% coverage.

7.2 COMPARING LIPIDS DRIED FROM H_2O AND DRIED FROM $CHCL_3$

While establishing the experimental approach for the wettability project, I tested the behavior of chloroform solutions of lipid. I found that the lipids dried from chloroform did not necessarily have the same morphology as those dried from water. For example, DSPE forms islands of different step-heights **(Figure 7-5)**. When dried from chloroform, the islands have a maximum step height of approximately 1.5 nm, whereas when dried from water, the step-height is a minimum of 2 nm. This suggests that the molecules change their aggregation behavior depending on the solvent, perhaps by changing the interdigitation of a bilayer, or the tail conformation in a monolayer.

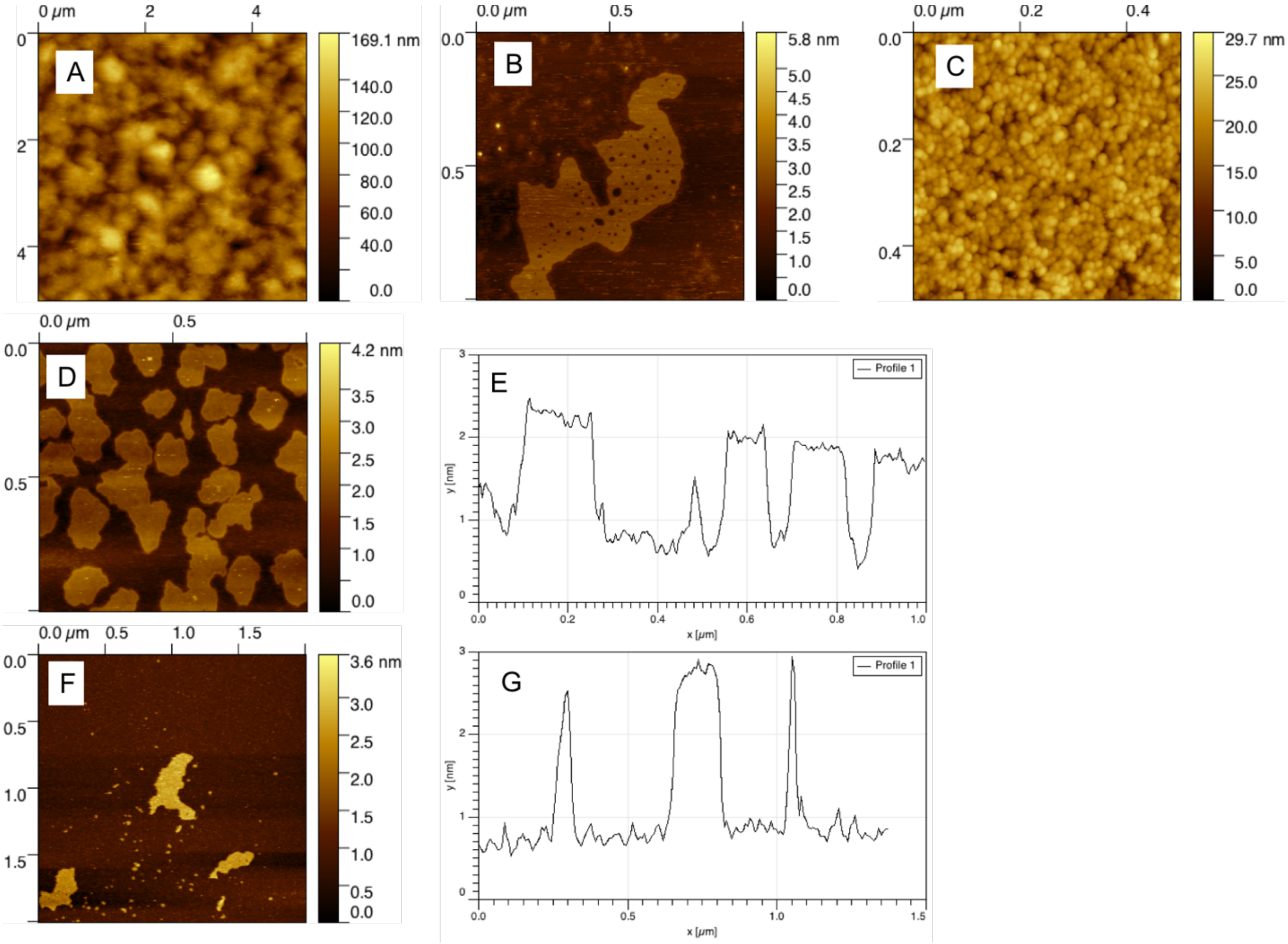

Figure 7-5: Lipids dried from chloroform vs. water. A) DSPG dried from chloroform. B) and C) represent DSPG dried from water. It is possible that A and C represent the same general structure. D) DSPE dried from chloroform and the associated height profile (E). (F) DSPE dried from water and the associated height profile (G).

7.3 HIGH-COVERAGE LIPID/CLAY FILMS

The decision to primarily conduct experiments using 10%, 25%, and 50% coverage was motivated by two reasons: 1) preliminary contact angle data suggested the largest changes in wettability occurred below 100% coverage, and 2) identifying the lipid aggregates at higher coverage (>100% coverage) was typically more difficult than in low coverage (<50% coverage) samples. In the case of 300% CAM, aggregates are only clearly identifiable for DSPG **(Figure 7-6)**.

At 100% and 200% CAM, I initially thought that DSPG could be identifiable in the phase images **(Figure 7-7)**. The dark areas in the phase image may indicate the location of DSPG layers (some line up with aggregates visible in the topography images). However, phase images of DOPC on mica also present such phase behavior, even though only DOPC is present in those samples. In order to use the phase images, an ideal image would contain two values: one phase value for the mineral surface, and one phase value for the lipid. If the lipid alone has multiple phase values, this complicates distinguishing the lipid from the mineral via phase images. Therefore, it is not possible to identify the lipid aggregates in the lipid/clay films with the phase images alone.

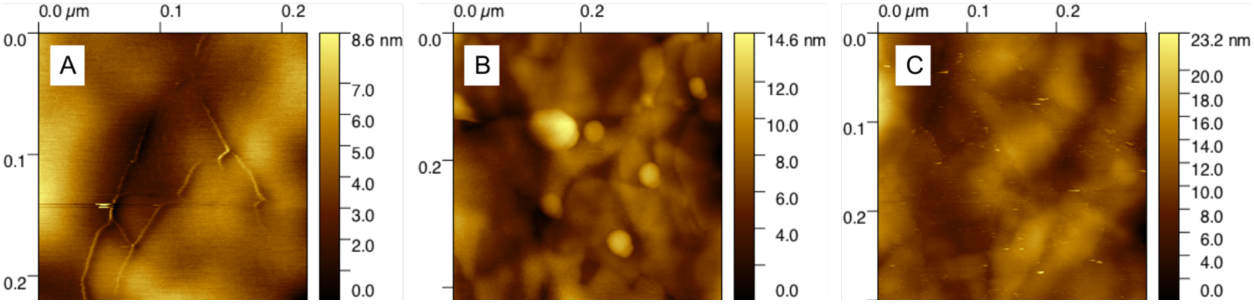

Figure 7-6: Lipids at 300% coverage on montmorillonite. A) DOPC, B) DSPG, C) DSPE.

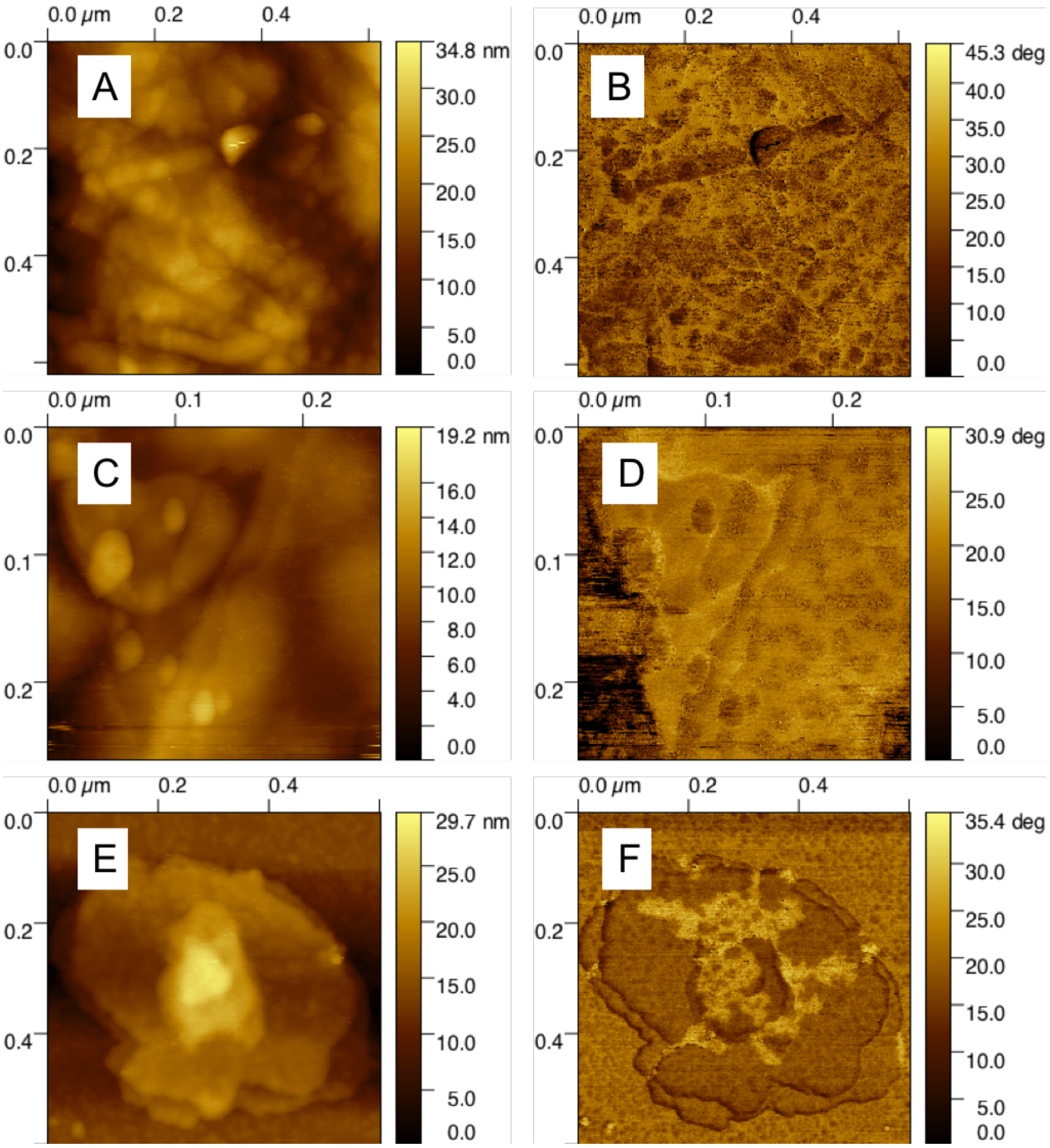

Figure 7-7: Topography (left column) vs. phase images (right column). A,B) DSPG at 100% coverage on montmorillonite. C,D) DSPG at 200% coverage on montmorillonite. E,F) DOPC on mica. Note that the phase image contains multiple color values.

APPENDIX A: CODE FOR DATA COLLECTION AND ANALYSIS

A.1 MATLAB CODE: CONTACT ANGLE EXTRACTION FROM DROPLET VIDEOS

MATLAB code by Dr. Elias Nakouzi (PNNL) to analyze droplet videos; included with permission.

```
%%%%%%%%%%% This code uses an .mp4 video file (pre-loaded into the workspace) of a
contact angle measurement to obtain the dynamics of the contact angle

% first load .mp4 movie, by dragging it from windows onto the command window below.
Name this new variable AA.
% AA is a 4D matrix where the first two dimensions are x and y,the third dimension is
RGB contrast values, and the fourth dimension is time

%%%%%%%%%%% In this first section in the program, the user will:
%%%%%%%%%%% 1) define the coordinates for xy cropping the image at four corners
(CROPx1, CROPx2, CROPy1, CROPy2)
%%%%%%%%%%% 2) define the ANGLE (in deg) that should be rotated to align the image
(for these data sets it is typically between -0.3 and -0.7
%%%%%%%%%%% 3) define the boundaries within which to search for the droplet, between
LEVELx1, LEVELx2, and above LEVEL
close all
A = AA(:,:,1,1300); % for defining the terms described above in 1) 2) 3), we need to
extract a single image from the movie. Let us pick randomly frame 1300, towards the
end of the movie (better to get an idea how wide the droplet has sank). NOTE: in the
third dimension of this matrix we put "1", we do not care about all RGB values. This
is good enough
% imagesc(A), % uncomment this line and the following ginput line, use the cursor
(shows up on figure because of ginput) to click on the frame at two opposite corners
around the droplet, to obtain the coordinates needed for cropping the droplet
% ginput()
CROPy1 = 1; CROPy2 = 744; CROPx1 = 230; CROPx2 = 530; % use the coordinates obtained
from the above ginput() line to define the cropping limits of the image. After doing
this re-comment the above imagesc and ginput lines, we do not need them anymore
ANGLE = -0.5; % now tweak this parameter, we need to rotate the image so that the
droplet is lying on a horizontal surface as much as possible
A = imrotate(A,ANGLE); % rotate the image
aa = A(CROPx1:CROPx2,CROPy1:CROPy2); % crop using the coordinates obtained above, this
magnified view is more useful
% imagesc(aa); % uncomment this and the following two lines to test and tweak for the
right ANGLE
% ginput(); % the cursor will help determine if the droplet is indeed "horizontal",
once happy with the cursor, use the ginput function to determine LEVELx1, LEVELx2, and
LEVEL
% stop
LEVEL = 270.5; LEVELx1 = 66; LEVELx2 = 647; inc = 1;
THRESH = 100; % threshold for binarizing, needed below, I never had to change it from
100 for these data sets, but here it is in case we needed to
FRAMErate = 25; % fps, found in movie file description, usually 25 for these data sets
```

```
% STOP % once happy with all the parameters comment this stop line and play program to
proceed to next sections
%%
[~,~,~,tSIZE] = size(AA); % tSIZE is how many frames in total are in the movie, not
that tSIZE/FRAMrate = TIME
MOV = []; % initiate a variable, we will need this in a few lines
for n = 1:1:tSIZE % now use the parameters obtained from the first section to process
all the images
    A = imrotate(AA(:,:,1,n),ANGLE); % rotate according to ANGLE
    A = A(CROPx1:CROPx2,CROPy1:CROPy2); % crop
    MOV(:,:,n) = A; % important line, we will basically reduce the movie to this
cropped and aligned movie, in the next section we will interact with this variable MOV
to detect the droplet
    %%%%%%%%%%% the next eight lines simply image the droplet, nice for checking
things, but usually I comment them out
%     imagesc(A)
%     daspect([1 1 1])
%     colormap(gray)
%     TXT = ['t = ',num2str(floor(n/FRAMErate)),' s']; % string for adding frame
number
%     text(5,15,TXT,'fontsize',14,'color','k','fontweight','bold'); % add text and
text position
%     axis off
%     drawnow
%     pause(0.3)
    %%%%%%%%%%% end of lines needed for showing the cropped images
end

%%%%%%%%%%%% In this section we will detect the droplet in each frame and find the
tangents
close all
NUM = 60; NUM1l = 16; NUM1r = 15; % NUM = how many data points from the binarized
droplet are needed to fit the tangent, NUM1l and NUM1r are how many data points to
skip on the left and right side of the droplet respectively to deal with the weird
droplet shape at the very edges
tDROP = 5; tt = 1; % tDROP is the frame when the droplet lands, initialize a variable
tt we need it later
cmp = get(gca,'ColorOrder'); % summons the matlab default color scheme, we need it for
pretty plots later
for t = 1:1:tSIZE % go through all frames iteratively
    aa = MOV(:,:,t); % let us consider frame t from the movie MOV
    [xx, yy] = size(aa); BIN = 100*ones(xx, yy); n = 1; % most importantly here, we
create an image of ones, which later will be populated with zeros where the droplet
exists, as such to binarize the droplet image
    for i = 1:LEVEL
        for j = LEVELx1:LEVELx2
            if aa(i,j) <= THRESH % THRESH is the threshold for binarizing, for these
data sets THRESH = 100 is good enough
                BIN(i,j) = 0; % if this pixel meets threshold constraint, make this
pixel a zero
                n = n+1;
            end
        end
    end

    if t > tDROP % do the following stuff if we are at a frame when the droplet has
already landed on the surface
    BOUND = bwboundaries(BIN); % these function segments the binarized image into
objects, BOUND will be a structure with multiple cells, I think usually the biggest
cell is the contour of the whole image, the second biggest cell is the contour of the
droplet, and there are sometimes cells with a few pixels of noise
```

```
    ssize = []; % the whole point of the next three lines is to find out which is the
second largest cell in the structure BOUND. Typically, that is our droplet
    for iii = 1:length(BOUND), ssize(iii) = length(BOUND{iii}); end
    [~,m2] = max(ssize); ssize(m2) = -1; [~,m2] = max(ssize);
    ind = find(BOUND{m2}(:,1) < LEVEL-1); % disregard the pixels below the horizontal
LEVEL defined in section 1
    PERI = BOUND{m2}(ind,:); % important line, this defines the perimeter of the
droplet based on all the above considerations

    DIAMdrop(tt) = (max(PERI(:,2)) - min(PERI(:,2))).*(0.5/70);
    HTdrop(tt) = (max(PERI(:,1)) - min(PERI(:,1))).*(0.5/70);


    PERI1 = PERI(NUM1l:NUM1l+NUM,:); PERI2 = PERI(end-NUM-NUM1r:end-NUM1r,:); % this
defines a bunch of pixels PERI1/PERI2 as the left/right edge using NUM, NUM1l, NUM1r
    s1 = polyfit(PERI1(:,2), PERI1(:,1),1); SLOPE1(tt) = -1*s1(1); % fit a line to the
left edge, save the negative of the slope
    s2 = polyfit(PERI2(:,2), PERI2(:,1),1); SLOPE2(tt) = s2(1); % fit a line to the
right edge, save theslope
    tt = tt+1;

%%%%%%%% the following five lines are usually commented out, I use them sometimes to
tweak and check if everything is fine, basically they plot different things as defined
%     hold on
%     plot(BOUND{1}(:,2),BOUND{1}(:,1),'go')
%     plot(BOUND{3}(:,2),BOUND{3}(:,1),'ro')
%         plot(PERI1(:,2),PERI1(:,1),'ro')
%         plot(PERI2(:,2),PERI2(:,1),'bo')

%%%%%%% the next if loop plots the frame once every 50 frames, including the fitted
tangents, plotting all >1700 frames is redundant, we are saving that data anyway, this
is just a check
    if rem(t,50) == 0
        imagesc(aa)
        hold on
        axis off, daspect([1 1 1]), colormap(gray) % cosmetics for image
        plot([PERI1(1,2) PERI1(end,2)+30],s1(1)*[PERI1(1,2)
PERI1(end,2)+30]+s1(2),'color',cmp(1,:),'linewidth',3) % plot left tangent
        plot([PERI2(1,2)-30 PERI2(end,2)],s2(1)*[PERI2(1,2)-30
PERI2(end,2)]+s2(2),'color',cmp(2,:),'linewidth',3) % plot right tangent
        TXT = ['t = ',num2str(floor(t/FRAMErate)),' s']; % string for adding frame
number
        text(5,15,TXT,'fontsize',14,'color','k','fontweight','bold'); % add text and
text position, basically a time stamp
        drawnow
    end
    end
end
TIME = (0:length(SLOPE1)-1)/FRAMErate; % save the TIME variable
ANGLE1 = atan(SLOPE1)*180/pi; % save the two sets of ANGLES in degrees
ANGLE2 = atan(SLOPE2)*180/pi;

%%%%%%%%%%%%%%% in this section we plot the slopes and angles we just calculated
figure(2)
scatter(TIME,SLOPE1,12,cmp(1,:),'filled','MarkerFaceAlpha',0.3)
hold on
scatter(TIME,SLOPE2,8,cmp(2,:),'MarkerFaceAlpha',0.5)
set(gca,'linewidth',2,'fontsize',16)
xlabel('t (s)','fontsize',19)
ylabel('slope','fontsize',19)
```

```
axis([0 inf -inf inf])
box on

figure(3)
plot(TIME,ANGLE2,'color',cmp(2,:),'linewidth',2)
hold on
plot(TIME,ANGLE1,'color',cmp(1,:),'linewidth',2)
set(gca,'linewidth',2,'fontsize',16)
xlabel('t (s)','fontsize',19)
ylabel('\theta_c (deg)','fontsize',19)
axis([0 inf -inf inf])
box on

STOP % STOP is important so that you do not save every time you run the program, when
happy with the result, comment out this line and run this section to save the data
%%%%%%% in this section, if everything is fine, we save all the parameters we used for
this calculation in .mat file, and the main three parameters in an excel sheet
save mmt6.mat TIME ANGLE ANGLE1 ANGLE2 SLOPE1 SLOPE2 CROPx1 CROPx2 CROPy1 CROPy2 LEVEL
LEVELx1 LEVELx2 THRESH NUM NUM1l NUM1r tDROP FRAMErate
AllVar = [TIME' ANGLE1' ANGLE2' DIAMdrop' HTdrop'];
csvwrite('mmt6.csv',AllVar)
```

A.2 PYTHON CODE: OBTAINING A AND K VALUES

```
#!/usr/bin/env python3
# -*- coding: utf-8 -*-
"""
Created on Sun Aug 25 06:25:22 2019

@author: Brenda

k_and_a_loop.py
Fit to obtain a and K values
"""
import numpy as np
import pandas as pd
import glob
import os
import matplotlib.pyplot as plt
from scipy import optimize

directory = os.chdir('/Users/Brenda/Dropbox/Research/Data/Analysis/Python/PG_radii/')
#tells the code where your files are
aList = []  #these lines set up lists that will be filled with information we want
kList = []
sampleList = []

for filename in glob.glob("*.csv"):        #initializes a loop so that every file in
the directory is analyzed

    #csv read
    data = pd.read_csv(filename)
    #radius= some index
    diameter = data.iloc[:,3] #python claims this index doesn't exist and i don't know
why, but the code still generates believable a and K vals
    time = data.iloc[:,0]
    #fit radius/radius0
    D0 = data.iloc[0,3]
    radRAT = (diameter/2)/(D0/2)

    def func(x, a, b):
        return a*(pow(x,b))+1

    params,params_covariance = optimize.curve_fit(func,time,radRAT,p0=[1,0.1])

    alpha = params[0]
    k = params[1]

    sampleList.append(filename)   #these lines write the values to the lists
initialized in lines 16 + 17
    aList.append(alpha)
    kList.append(k)


#these lines write the values to a csv file, along with the sample name
dataframe = pd.DataFrame({"sample":sampleList,"a":aList, "k":kList})
dataframe.to_csv('/Users/Brenda/Dropbox/Research/Data/Analysis/Python/pg_a_k.csv')
```

A.3 PYTHON CODE: LINEAR REGRESSIONS

```
#!/usr/bin/env python3
# -*- coding: utf-8 -*-
"""
Created on Tue Sep 24 16:48:44 2019

@author: Brenda

LinRegLoop.py
Linear regressions
"""

#Currently works for dictionaries with no NaN values (potential workaround:
find+remove indices corresponding to nan)

import numpy as np
import pandas as pd
from sklearn.linear_model import LinearRegression

data =
pd.read_excel(r'/Users/Brenda/Dropbox/Research/Data/Analysis/Python/PG_all_variables.x
lsx',index_col=0)

#Wetting Var
DOPG_CA_mmt = data.loc[["MMT0","DOPG10","DOPG25","DOPG50"],["CA0_avg"]].to_numpy()
DOPG_TC_mmt = data.loc[["MMT0","DOPG10","DOPG25","DOPG50"],["TC_avg"]].to_numpy()
DOPG_a_mmt = data.loc[["MMT0","DOPG10","DOPG25","DOPG50"],["a_avg"]].to_numpy()

DOPG_CA = data.loc[["DOPG10","DOPG25","DOPG50"],["CA0_avg"]].to_numpy()
DOPG_TC = data.loc[["DOPG10","DOPG25","DOPG50"],["TC_avg"]].to_numpy()
DOPG_a = data.loc[["DOPG10","DOPG25","DOPG50"],["a_avg"]].to_numpy()

DSPG_CA_mmt = data.loc[["MMT0","DSPG10","DSPG25","DSPG50"],["CA0_avg"]].to_numpy()
DSPG_TC_mmt = data.loc[["MMT0","DSPG10","DSPG25","DSPG50"],["TC_avg"]].to_numpy()
DSPG_a_mmt = data.loc[["MMT0","DSPG10","DSPG25","DSPG50"],["a_avg"]].to_numpy()
DSPG_CA = data.loc[["DSPG10","DSPG25","DSPG50"],["CA0_avg"]].to_numpy()
DSPG_TC = data.loc[["DSPG10","DSPG25","DSPG50"],["TC_avg"]].to_numpy()
DSPG_a = data.loc[["DSPG10","DSPG25","DSPG50"],["a_avg"]].to_numpy()

#PhysVar
DOPG_AvgDiam = data.loc[["DOPG10","DOPG25","DOPG50"],["Avg diameter (nm)"]].to_numpy()
DOPG_AggDen = data.loc[["DOPG10","DOPG25","DOPG50"],["Aggregate/nm2
Estimate"]].to_numpy()
DOPG_EdgeFrac = data.loc[["DOPG10","DOPG25","DOPG50"],["edge/total
aggregates"]].to_numpy()
DOPG_flbin25_junc = data.loc[["DOPG10","DOPG25","DOPG50"],["Bin25Fl Junc"]].to_numpy()
DOPG_flbin50_junc = data.loc[["DOPG10","DOPG25","DOPG50"],["Bin50Fl Junc"]].to_numpy()
DOPG_flbin75_junc = data.loc[["DOPG10","DOPG25","DOPG50"],["Bin75Fl Junc"]].to_numpy()
DOPG_flbin25_skelrat = data.loc[["DOPG10","DOPG25","DOPG50"],["Bin25Fl
SkelRat"]].to_numpy()
DOPG_flbin50_skelrat = data.loc[["DOPG10","DOPG25","DOPG50"],["Bin50Fl
SkelRat"]].to_numpy()
DOPG_flbin75_skelrat = data.loc[["DOPG10","DOPG25","DOPG50"],["Bin75Fl
Skelrat"]].to_numpy()
DOPG_afmbin25_junc = data.loc[["DOPG10","DOPG25","DOPG50"],["Bin25AFM
Junc"]].to_numpy()
DOPG_afmbin50_junc = data.loc[["DOPG10","DOPG25","DOPG50"],["Bin50AFM
Junc"]].to_numpy()
```

```
DOPG_afmbin75_junc = data.loc[["DOPG10","DOPG25","DOPG50"],["Bin75AFM
Junc"]].to_numpy()
DOPG_afmbin25_skelrat = data.loc[["DOPG10","DOPG25","DOPG50"],["Bin25AFM
SkelRat"]].to_numpy()
DOPG_afmbin50_skelrat = data.loc[["DOPG10","DOPG25","DOPG50"],["Bin50AFM
SkelRat"]].to_numpy()
DOPG_afmbin75_skelrat = data.loc[["DOPG10","DOPG25","DOPG50"],["Bin75AFM
Skelrat"]].to_numpy()

DSPG_flbin25_junc = data.loc[["DSPG10","DSPG25","DSPG50"],["Bin25Fl Junc"]].to_numpy()
DSPG_flbin50_junc = data.loc[["DSPG10","DSPG25","DSPG50"],["Bin50Fl Junc"]].to_numpy()
DSPG_flbin75_junc = data.loc[["DSPG10","DSPG25","DSPG50"],["Bin75Fl Junc"]].to_numpy()
DSPG_flbin25_skelrat = data.loc[["DSPG10","DSPG25","DSPG50"],["Bin25Fl
SkelRat"]].to_numpy()
DSPG_flbin50_skelrat = data.loc[["DSPG10","DSPG25","DSPG50"],["Bin50Fl
SkelRat"]].to_numpy()
DSPG_flbin75_skelrat = data.loc[["DSPG10","DSPG25","DSPG50"],["Bin75Fl
Skelrat"]].to_numpy()
DSPG_afmbin25_junc = data.loc[["DSPG10","DSPG25","DSPG50"],["Bin25AFM
Junc"]].to_numpy()
DSPG_afmbin50_junc = data.loc[["DSPG10","DSPG25","DSPG50"],["Bin50AFM
Junc"]].to_numpy()
DSPG_afmbin75_junc = data.loc[["DSPG10","DSPG25","DSPG50"],["Bin75AFM
Junc"]].to_numpy()
DSPG_afmbin25_skelrat = data.loc[["DSPG10","DSPG25","DSPG50"],["Bin25AFM
SkelRat"]].to_numpy()
DSPG_afmbin50_skelrat = data.loc[["DSPG10","DSPG25","DSPG50"],["Bin50AFM
SkelRat"]].to_numpy()
DSPG_afmbin75_skelrat = data.loc[["DSPG10","DSPG25","DSPG50"],["Bin75AFM
Skelrat"]].to_numpy()

#########Assemble dictionaries of data###########
DOPG_Wet = {'DOPG_CA': DOPG_CA.reshape(-1, 1), 'DOPG_TC':DOPG_TC.reshape(-1,
1),'DOPG_a':DOPG_a.reshape(-1,1)}
DOPG_Phys = {'DOPG_AvgDiam': DOPG_AvgDiam.reshape(-1, 1),
'DOPG_AggDen':DOPG_AggDen.reshape(-1, 1),'DOPG_EdgeFrac':DOPG_EdgeFrac.reshape(-
1,1),'DOPG_flbin25_junc':DOPG_flbin25_junc.reshape(-1,
1),'DOPG_flbin50_junc':DOPG_flbin50_junc.reshape(-1,
1),'DOPG_flbin75_junc':DOPG_flbin75_junc.reshape(-1,
1),'DOPG_flbin25_skelrat':DOPG_flbin25_skelrat.reshape(-1,
1),'DOPG_flbin50_skelrat':DOPG_flbin50_skelrat.reshape(-1,
1),'DOPG_flbin75_skelrat':DOPG_flbin75_skelrat.reshape(-1,
1),'DOPG_afmbin25_junc':DOPG_afmbin25_junc.reshape(-1,
1),'DOPG_afmbin50_junc':DOPG_afmbin50_junc.reshape(-1,
1),'DOPG_afmbin75_junc':DOPG_afmbin75_junc.reshape(-1,
1),'DOPG_afmbin25_skelrat':DOPG_afmbin25_skelrat.reshape(-1,
1),'DOPG_afmbin50_skelrat':DOPG_afmbin50_skelrat.reshape(-1,
1),'DOPG_afmbin75_skelrat':DOPG_afmbin75_skelrat.reshape(-1, 1)}

DSPG_Wet = {'DSPG_CA': DSPG_CA.reshape(-1, 1), 'DSPG_TC':DSPG_TC.reshape(-1,
1),'DSPG_a':DSPG_a.reshape(-1,1)}
DSPG_Phys = {'DSPG_flbin25_junc':DSPG_flbin25_junc.reshape(-1,
1),'DSPG_flbin50_junc':DSPG_flbin50_junc.reshape(-1,
1),'DSPG_flbin75_junc':DSPG_flbin75_junc.reshape(-1,
1),'DSPG_flbin25_skelrat':DSPG_flbin25_skelrat.reshape(-1,
1),'DSPG_flbin50_skelrat':DSPG_flbin50_skelrat.reshape(-1,
1),'DSPG_flbin75_skelrat':DSPG_flbin75_skelrat.reshape(-1,
1),'DSPG_afmbin25_junc':DSPG_afmbin25_junc.reshape(-1,
1),'DSPG_afmbin50_junc':DSPG_afmbin50_junc.reshape(-1,
1),'DSPG_afmbin75_junc':DSPG_afmbin75_junc.reshape(-1,
1),'DSPG_afmbin25_skelrat':DSPG_afmbin25_skelrat.reshape(-1,
```

```
1),'DSPG_afmbin50_skelrat':DSPG_afmbin50_skelrat.reshape(-1,
1),'DSPG_afmbin75_skelrat':DSPG_afmbin75_skelrat.reshape(-1, 1)}

#testLR = LinearRegression().fit(Lip1EdgeFrac,Lip1a)
#print(testLR.score(Lip1EdgeFrac,Lip1a),testLR.coef_)


for N,W in DOPG_Wet.items(): #Am using N,M here to refer to the Key and P,W to the
Value
    for M,P in DOPG_Phys.items():
        LR = LinearRegression().fit(P,W)
        print(N, M, 'r2', LR.score(P,W), 'slope', LR.coef_)

for NS,WS in DSPG_Wet.items():
    for MS,PS in DSPG_Phys.items():
        LR = LinearRegression().fit(PS,WS)
        print(NS, MS, 'r2', LR.score(PS,WS), 'slope', LR.coef_)

####Special DSPG ones that have 10%, 25%, and 30% only####
DSPG_AvgDiam = data.loc[["DSPG10","DSPG25","DSPG30"],["Avg diameter (nm)"]].to_numpy()
DSPG_AggDen = data.loc[["DSPG10","DSPG25","DSPG30"],["Aggregate/nm2
Estimate"]].to_numpy()
DSPG_EdgeFrac = data.loc[["DSPG10","DSPG25","DSPG30"],["edge/total
aggregates"]].to_numpy()

DSPG_CA_c = data.loc[["DSPG10","DSPG25","DSPG30"],["CA0_avg"]].to_numpy()  #C for
Cypher, since we're doing this for cypher data.
DSPG_TC_c = data.loc[["DSPG10","DSPG25","DSPG30"],["TC_avg"]].to_numpy()
DSPG_a_c = data.loc[["DSPG10","DSPG25","DSPG30"],["a_avg"]].to_numpy()

DSPGc_Wet = {'DSPG_CA':DSPG_CA_c.reshape(-1, 1),'DSPG_TC':DSPG_TC_c.reshape(-1,
1),'DSPG_a':DSPG_a_c.reshape(-1, 1)}
DSPGc_Phys = {'DSPG_AvgDiam':DSPG_AvgDiam.reshape(-1,
1),'DSPG_AggDen':DSPG_AggDen.reshape(-1, 1),'DSPG_EdgeFrac':DSPG_EdgeFrac.reshape(-1,
1)}

for O,X in DSPGc_Wet.items(): #Am using N,M here to refer to the Key and P,W to the
Value
    for Q,R in DSPGc_Phys.items():
        LR = LinearRegression().fit(R,X)
        print(O, Q, 'r2', LR.score(R,X), 'slope', LR.coef_)
```

A.4 PYTHON CODE: BINARY THRESHOLD AUTOMATION

```
#!/usr/bin/env python3
# -*- coding: utf-8 -*-
"""
Created on Thu Jun 27 17:50:21 2019

@author: Brenda

binary_threshold.py
Slices grayscale images into three binary images
"""

#import necessary python packages, which contain functions we'll use below
import matplotlib.pyplot as plt
import imageio
import numpy as np
import os
import glob

#establish input+output directories
path = os.chdir('/Users/Brenda/Dropbox/Research/Data/Analysis/Python/DOPG10')
output_path = ('/Users/Brenda/Dropbox/Research/Data/Analysis/Python/DOPG10/bin')

for filename in glob.glob("*.png"):
    #import image as a matrix (an ndarray)
    img = imageio.imread(filename)

    ##threshold according to percentile
    bin75 = np.percentile(img,75)     #gives 75th percentile value in the image
matrix; we'll use this as the threshold
    imgthresh75 = np.empty(img.shape) #creates a new matrix for the binarized image
    imgthresh75[img > bin75] = 0      #fills empty matrix with black for parts of the
image above the threshold
    imgthresh75[img < bin75] = 255    #fills matrix with white below the threshold
    plt.imshow(imgthresh75, interpolation='nearest') #shows new, binarized image
    plt.show()
    output_filepath =  os.path.join(output_path, filename + "_75" + '.png') #makes
filename for binarized image based off of original name
    imageio.imwrite(output_filepath,imgthresh75) #writes the new binary image to the
output directory


    bin50 = np.percentile(img,50)
    imgthresh50 = np.empty(img.shape)
    imgthresh50[img > bin50] = 0
    imgthresh50[img < bin50] = 255
    plt.imshow(imgthresh50, interpolation='nearest')
    plt.show()
    output_filepath =  os.path.join(output_path, filename + "_50" + '.png')
    imageio.imwrite(output_filepath,imgthresh50)

    bin25 = np.percentile(img,25)
    imgthresh25 = np.empty(img.shape)
    imgthresh25[img > bin25] = 0
    imgthresh25[img < bin25] = 255
    plt.imshow(imgthresh25, interpolation='nearest')
    plt.show()
    output_filepath =  os.path.join(output_path, filename + '_25' + '.png')
    imageio.imwrite(output_filepath,imgthresh25)
```

A.5 PYTHON CODE: SKELETON RATIO

```
#!/usr/bin/env python3
# -*- coding: utf-8 -*-
"""
Created on Mon Jun 24 16:26:35 2019

@author: Brenda

skeleton_loop.py
Calculates skeleton ratio from image
"""
#importing all the python packages we're going to use
import numpy as np
import pandas as pd
from skimage import io
import glob
import os

directory = os.chdir('/Users/Brenda/Dropbox/Research/Data/Analysis/2019Images for
analysis - PGs/PG AFM Skel') #tells the code where your files are
ratioList = []  #these lines set up lists that will be filled with information we want
sampleList = []

for filename in glob.glob("*.tif"): #initializes a loop so that every file in the
directory is analyzed

    skeleton = io.imread(filename)  #reads the file as a matrix where white pixels
have a value of 0 and black pixels have a value of 255
    blackpixels = np.count_nonzero(skeleton) #counts all the black pixels
    skel_ratio = blackpixels/skeleton.size   #divides the number of black pixels by
the total number of pixels in the image

    print(filename,skel_ratio)    #I put this here as a "sanity check"; it should list
every file in the directory

    sampleList.append(filename)   #these lines write the values to the lists
initialized in lines 16 + 17
    ratioList.append(skel_ratio)


#these lines write the values to a csv file, along with the sample name
dataframe = pd.DataFrame({"sample":sampleList,"skel ratio":ratioList})
dataframe.to_csv('/Users/Brenda/Dropbox/Research/Data/Analysis/2019Images for analysis
- PGs/PGafm_skelratio.csv')
```

BIBLIOGRAPHY

---

1 Tschapek, M. (1984). Criteria for Determining the hydrophilicity-hydrophobicity of Soils. Zeitschrift Für Pflanzenernährung Und Bodenkunde *147*, 137–149.

2 Bodí, M.B., Muñoz-Santa, I., Armero, C., Doerr, S.H., Mataix-Solera, J., and Cerdà, A. (2013). Spatial and temporal variations of water repellency and probability of its occurrence in calcareous Mediterranean rangeland soils affected by fires. CATENA *108*, 14–25.

3 Mataix-Solera, J., Arcenegui, V., Tessler, N., Zornoza, R., Wittenberg, L., Martínez, C., Caselles, P., Pérez-Bejarano, A., Malkinson, D., and Jordán, M.M. (2013). Soil properties as key factors controlling water repellency in fire-affected areas: Evidences from burned sites in Spain and Israel. CATENA *108*, 6–13.

4 Goebel, M.-O., Bachmann, J., Reichstein, M., Janssens, I.A., and Guggenberger, G. (2011). Soil water repellency and its implications for organic matter decomposition – is there a link to extreme climatic events? Global Change Biology *17*, 2640–2656.

5 Schmidt, M.W.I., Torn, M.S., Abiven, S., Dittmar, T., Guggenberger, G., Janssens, I.A., Kleber, M., Kögel-Knabner, I., Lehmann, J., Manning, D.A.C., et al. (2011). Persistence of soil organic matter as an ecosystem property. Nature *478*, 49–56.

6 Vogel, C., Mueller, C.W., Höschen, C., Buegger, F., Heister, K., Schulz, S., Schloter, M., and Kögel-Knabner, I. (2014). Submicron structures provide preferential spots for carbon and nitrogen sequestration in soils. Nat Communications *5*, 1–7.

7 Lehmann, J., and Kleber, M. (2015). The contentious nature of soil organic matter. Nature *528*, 60–68.

8 Richter, R.P., Bérat, R., and Brisson, A.R. (2006). Formation of Solid-Supported Lipid Bilayers: An Integrated View. Langmuir *22*, 3497–3505.

9 Achtenhagen, J., Goebel, M.-O., Miltner, A., Woche, S.K., and Kästner, M. (2015). Bacterial impact on the wetting properties of soil minerals. Biogeochemistry *122*, 269–280.

10 Leelamanie, D. a. L., Karube, J., and Yoshida, A. (2008). Characterizing water repellency indices: Contact angle and water drop penetration time of hydrophobized sand. Soil Science & Plant Nutrition *54*, 179–187.

11 Doerr, S.H., Shakesby, R.A., and Walsh, R.P.D. (2000). Soil water repellency: its causes, characteristics and hydro-geomorphological significance. Earth-Science Reviews *51*, 33–65.

12 Truong, V.K., Owuor, E.A., Murugaraj, P., Crawford, R.J., and Mainwaring, D.E. (2015). Impact of particle nanotopology on water transport through hydrophobic soils. Journal of Colloid and Interface Science *460*, 61–70.

13 Ma'shum, M., Tate, M.E., Jones, G.P., and Oades, J.M. (1988). Extraction and characterization of water–repellent materials from Australian soils. Journal of Soil Science *39*, 99–110.

14 de Blas, E., Rodríguez-Alleres, M., and Almendros, G. (2010). Speciation of lipid and humic fractions in soils under pine and eucalyptus forest in northwest Spain and its effect on water repellency. Geoderma *155*, 242–248.

15 Mainwaring K., Hallin I. L., Douglas P., Doerr S. H., and Morley C. P. (2013). The role of naturally occurring organic compounds in causing soil water repellency. European Journal of Soil Science *64*, 667–680.

16 Kaltenbach, R., Diehl, D., and Schaumann, G.E. (2018). Links between nanoscale and macroscale surface properties of natural root mucilage studied by atomic force microscopy and contact angle. Journal of Colloid and Interface Science *516*, 446–455.

17 Cheng, S., Bryant, R., Doerr, S.H., Wright, C.J., and Williams, P.R. (2009). Investigation of Surface Properties of Soil Particles and Model Materials with Contrasting Hydrophobicity Using Atomic Force Microscopy. Environ. Sci. Technol. *43*, 6500–6506.

18 Cheng, S., Doerr, S.H., Bryant, R., and Wright, C.J. (2010). Effects of Isopropanol/Ammonia Extraction on Soil Water Repellency as Determined by Atomic Force Microscopy. Soil Science Society of America Journal *74*, 1541–1552.

19 Jung, Y.C., and Bhushan, B. (2006). Contact angle, adhesion and friction properties of micro-and nanopatterned polymers for superhydrophobicity. Nanotechnology *17*, 4970.

20 Zisman, W.A. (1964). Relation of the Equilibrium Contact Angle to Liquid and Solid Constitution. Contact Angle, Wettability, and Adhesion (American Chemical Society), pp. 1–51.

21 Letey, J.; Carrillo, M. L. K.; Pang, X. P. (2000) Approaches to Characterize the Degree of Water Repellency. *J. Hydrol.*, *231*, 61–65.

22 King, P.M. (1981). Comparison of methods for measuring severity of water repellence of sandy soils and assessment of some factors that affect its measurement. Australian Journal of Soil Research *19*, 275.

23 Dekker, L.W., and Ritsema, C.J. (1994). How water moves in a water repellent sandy soil: 1. Potential and actual water repellency. Water Resources Research *30*, 2507–2517.

24 Roy, J.L., and McGill, W.B. (2000). Flexible conformation in organic matter coatings: An hypothesis about soil water repellency. Can. J. Soil. Sci. *80*, 143–152.

25 McHale G., Newton M. I., and Shirtcliffe N. J. (2004). Water-repellent soil and its relationship to granularity, surface roughness and hydrophobicity: a materials science view. European Journal of Soil Science *56*, 445–452.

26 Petridis, L., Ambaye, H., Jagadamma, S., Kilbey, S.M., Lokitz, B.S., Lauter, V., and Mayes, M.A. (2014). Spatial Arrangement of Organic Compounds on a Model Mineral Surface: Implications for Soil Organic Matter Stabilization. Environ. Sci. Technol. *48*, 79–84.

27 Chao, T.C., Arjmandi-Tash, O., Das, D.B., and Starov, V.M. (2015). Spreading of blood drops over dry porous substrate: Complete wetting case. Journal of Colloid and Interface Science *446*, 218–225.

28 Chao, T.C., Arjmandi-Tash, O., Das, D.B., and Starov, V.M. (2016). Simultaneous spreading and imbibition of blood droplets over porous substrates in the case of partial wetting. Colloids and Surfaces A: Physicochemical and Engineering Aspects *505*, 9–17.

29 Schramm, L.L. (2006). Colloid Rheology. In Emulsions, Foams, and Suspensions, (John Wiley & Sons, Ltd), pp. 155–199.

30 Liu, H.-H., Li, L., and Birkholzer, J. (2012). Unsaturated properties for non-Darcian water flow in clay. Journal of Hydrology *430–431*, 173–178.

31 Cui, Y.J., Tang, A.M., Loiseau, C., and Delage, P. (2008). Determining the unsaturated hydraulic conductivity of a compacted sand–bentonite mixture under constant-volume and free-swell conditions. Physics and Chemistry of the Earth, Parts A/B/C *33*, S462–S471.

32 Zou, Y. (1996). A non-linear permeability relation depending on the activation energy of pore liquid. Géotechnique *46*, 769–774.

33 Low, P.F. (1961). Physical Chemistry of Clay-Water Interaction. In Advances in Agronomy, A.G. Norman, ed. (Academic Press), pp. 269–327.

---

34 Kim, W.-J., and Yang, S.-M. (2000). Effects of Sodium Salicylate on the Microstructure of an Aqueous Micellar Solution and Its Rheological Responses. Journal of Colloid and Interface Science *232*, 225–234.

35 Binnig, G., C. F. Quate, and Ch. Gerber. 1986. "Atomic Force Microscope." Physical Review Letters 56 (9): 930 33. doi:10.1103/PhysRevLett.56.930.

36 Chow, Ernest H. H., Dejan-Krešimir Bučar, and William Jones. 2012. "New Opportunities in Crystal Engineering – the Role of Atomic Force Microscopy in Studies of Molecular Crystals." *Chemical Communications* 48 (74): 9210. doi:10.1039/c2cc32678g.

37 Zhong, Q., Inniss, D., Kjoller, K., and Elings, V.B. (1993). Fractured polymer/silica fiber surface studied by tapping mode atomic force microscopy. Surface Science Letters *290*, L688–L692.

38 Zhao, Y., Cheng, Q., Qian, M., and Cantrell, J.H. (2010). Phase image contrast mechanism in intermittent contact atomic force microscopy. Journal of Applied Physics *108*, 094311.

39 Ye, Z., and Zhao, X. (2010). Phase imaging atomic force microscopy in the characterization of biomaterials. Journal of Microscopy *238*, 27–35.

40 Veatch, S.L., and Keller, S.L. (2002). Organization in Lipid Membranes Containing Cholesterol. Phys. Rev. Lett. *89*, 268101.

41 McKissock, I., Walker, E.L., Gilkes, R.J., and Carter, D.J. (2000). The influence of clay type on reduction of water repellency by applied clays: a review of some West Australian work. Journal of Hydrology *231*, 323–332.

42 Gmeinfr, J., and Martin, H.H. Phospholipid and Lipopolysaccharide in Proteus mirabilis and Its Stable Protoplast l-Form. European Journal of Biochemistry *67*, 487–494.

43 Siervo, A.J.D., and Homola, A.D. (1980). Analysis of caulobacter crescentus lipids. J. Bacteriol. *143*, 1215–1222.

44 Kessenich, B.L., Pokhrel, N., Nakouzi, E., Newcomb, C.J., Flury, M., Maibaum, L., and De Yoreo, J.J. (2019). Connecting wettability, topography, and chemistry in a simple lipid-montmorillonite system. Journal of Colloid and Interface Science *555*, 498–508.

45 Kessenich, B.L., Pokhrel, N., Kibue, J.K., Flury, M., Maibaum, L., and De Yoreo, J.J. (2020). Negatively-charged phospholipids exhibit negligible effects on the water repellency of montmorillonite films. *Under review.*

46 Berendsen, H.J.C., van der Spoel, D., and van Drunen, R. (1995). GROMACS: A message-passing parallel molecular dynamics implementation. Computer Physics Communications *91*, 43–56.

47 Tribello, G.A., Bonomi, M., Branduardi, D., Camilloni, C., and Bussi, G. (2014). PLUMED 2: New feathers for an old bird. Computer Physics Communications *185*, 604–613.

48 Darden, T., York, D., and Pedersen, L. (1993). Particle mesh Ewald: An N·log(N) method for Ewald sums in large systems. J. Chem. Phys. *98*, 10089–10092.

49 Hess, B., Bekker, H., Berendsen, H.J.C., and Fraaije, J.G.E.M. (1997). LINCS: A linear constraint solver for molecular simulations. Journal of Computational Chemistry *18*, 1463–1472.

50 Ritsema, C. J.; Dekker, L. W. How Water Moves in a Water Repellent Sandy Soil: 2. Dynamics of Fingered Flow. *Water Resour. Res.* **1994**, *30* (9), 2519–2531.

51 Osborn, J. F.; Pelishek, R. E.; Krammes, J. S.; Letey, J. Soil Wettability as a Factor in Erodibility. *Soil Sci. Soc. Am. J.* **1964**, *28* (2), 294–295.

---

52 Ma'shum, M.; Farmer, V. C. Origin and Assessment of Water Repellency of a Sandy South Australian Soil. *Soil Res.* **1985**, *23* (4), 623–626.

53 Blosser, M. C.; Starr, J. B.; Turtle, C. W.; Ashcraft, J.; Keller, S. L. Minimal Effect of Lipid Charge on Membrane Miscibility Phase Behavior in Three Ternary Systems. *Biophys. J.* **2013**, *104* (12), 2629–2638.

54 Feller, S. E.; Venable, R. M.; Pastor, R. W. Computer Simulation of a DPPC Phospholipid Bilayer: Structural Changes as a Function of Molecular Surface Area. *Langmuir* **1997**, *13* (24), 6555–6561.

55 Lewis, B. A.; Engelman, D. M. Lipid Bilayer Thickness Varies Linearly with Acyl Chain Length in Fluid Phosphatidylcholine Vesicles. *J. Mol. Biol.* **1983**, *166* (2), 211–217.

56 Dogan, M.; Dogan, A. U.; Yesilyurt, F. I.; Alaygut, D.; Buckner, I.; Wurster, D. E. Baseline Studies of the Clay Minerals Society Special Clays: Specific Surface Area by the Brunauer Emmett Teller (Bet) Method. *Clays Clay Miner.* **2007**, *55* (5), 534–541.

57 Black, R.A., and Blosser, M.C. (2016). A Self-Assembled Aggregate Composed of a Fatty Acid Membrane and the Building Blocks of Biological Polymers Provides a First Step in the Emergence of Protocells. Life *6*, 33.

58 Forsythe, J.G., Yu, S.-S., Mamajanov, I., Grover, M.A., Krishnamurthy, R., Fernández, F.M., and Hud, N.V. (2015). Ester-Mediated Amide Bond Formation Driven by Wet–Dry Cycles: A Possible Path to Polypeptides on the Prebiotic Earth. Angewandte Chemie International Edition *54*, 9871–9875.

59 Ross, D.S., and Deamer, D. (2016). Dry/Wet Cycling and the Thermodynamics and Kinetics of Prebiotic Polymer Synthesis. Life *6*, 28.

60 DeGuzman, V., Vercoutere, W., Shenasa, H., and Deamer, D. (2014). Generation of Oligonucleotides Under Hydrothermal Conditions by Non-enzymatic Polymerization. J Mol Evol *78*, 251–262.

61 Da Silva, L., Maurel, M.-C., and Deamer, D. (2015). Salt-promoted synthesis of RNA-like molecules in simulated hydrothermal conditions. J. Mol. Evol. *80*, 86–97.

62 Rajamani, S., Vlassov, A., Benner, S., Coombs, A., Olasagasti, F., and Deamer, D. (2008). Lipid-assisted Synthesis of RNA-like Polymers from Mononucleotides. Orig Life Evol Biosph *38*, 57–74.

63 Deamer, D. (2012). Liquid crystalline nanostructures : organizing matrices for non-enzymatic nucleic acid polymerization. Chemical Society Reviews *41*, 5375–5379.

64 Toppozini, L., Dies, H., Deamer, D.W., and Rheinstädter, M.C. (2013). Adenosine Monophosphate Forms Ordered Arrays in Multilamellar Lipid Matrices: Insights into Assembly of Nucleic Acid for Primitive Life. PLOS ONE *8*, e62810.

65 Blumstein, A., Kitagawa, N., and Blumstein, R. (1971). Polymerization of p-Methacryloyloxy Benzoic Acid within Liquid Crystalline Media. Molecular Crystals and Liquid Crystals *12*, 215–227.

66 Deamer, D., Dworkin, J.P., Sandford, S.A., Bernstein, M.P., and Allamandola, L.J. (2002). The First Cell Membranes. Astrobiology *2*, 371–381.

67 Deamer, D.W., and Pashley, R.M. (1989). Amphiphilic components of the murchison carbonaceous chondrite: Surface properties and membrane formation. Origins Life Evol Biosphere *19*, 21–38.

68 Cornell, C.E., Black, R.A., Xue, M., Litz, H.E., Ramsay, A., Gordon, M., Mileant, A., Cohen, Z.R., Williams, J.A., Lee, K.K., et al. (2019). Prebiotic amino acids bind to and stabilize prebiotic fatty acid membranes. PNAS *116*, 17239–17244.

---

69 Apel, C.L., Deamer, D.W., and Mautner, M.N. (2002). Self-assembled vesicles of monocarboxylic acids and alcohols: conditions for stability and for the encapsulation of biopolymers. Biochim. Biophys. Acta *1559*, 1–9.

70 Israelachvili, J.N., Mitchell, D.J., and Ninham, B.W. (1976). Theory of self-assembly of hydrocarbon amphiphiles into micelles and bilayers. J. Chem. Soc., Faraday Trans. 2 *72*, 1525–1568.

71 Quinn, James A. (2018). Notes on the Development of a Critical Packing Parameter routine for Molecular Modeling ProPlus. Norgwyn Montgomery Software, Inc. https://www.norgwyn.com/pdf/CPP.pdf, accessed 5/1/2020.

72 Lane, C.A., Burton, D.E., and Crabb, C.C. (1984). Accurate molecular dimensions from stearic acid monolayers. Journal of Chemical Education *61*, 815.

73 Zhao, Y.H., Abraham, M.H., and Zissimos, A.M. (2003). Fast Calculation of van der Waals Volume as a Sum of Atomic and Bond Contributions and Its Application to Drug Compounds. J. Org. Chem. *68*, 7368–7373.